Institut National des Sciences Appliquées

Dept. of Engineering Mathematics,
Numerical Modeling.

Université Paul Sabatier

Master of Science,
Applied Analysis, Modeling and Scientific Computing.

TECHNICAL REPORT

Preliminary Investigation of Data Assimilation Methodologies for Forest Fire Propagation

Mélanie Rochoux

February - October 2010

Supervisors:

Prof. Arnaud Trouvé
Dept. of Fire Protection Engineering,
University of Maryland,
College Park, MD 20742.

Dr. Sophie Ricci
GLOBC Research Team,
Centre Européen de Recherche et de
Formation Avancée en Calcul Scientifique,
Toulouse, France.

November 1, 2010

Abstract

The present study aims at demonstrating that some of the limitations of wildfire modeling can be overcome by coupling information coming from both observations and models using data assimilation techniques. The concept is that a data-driven fire model can lead to more accurate predictions of fire spread. This work is limited to a stand-alone numerical feasibility with the objective of calibrating some of the parameters of a numerical model using the Best Linear Unbiased Estimator (BLUE) algorithm. The observations are synthetic, i.e. generated with the numerical model; the treatment of real observations from fire sensors is not addressed.

A simplified model of premixed combustion is used to simulate the evolution of a wildfire. The model is based on a reaction-diffusion equation for a progress variable in which the local flame speed (i.e., the local rate of spread) is the main physical quantity. In a preliminary step, the local flame speed depends on a single variable that represents the effects of a non-uniform vegetation (i.e., fuel) distribution.

Two different data assimilation strategies are explored: an Eulerian approach in which observations of the progress variable are made at fixed spatial locations over the computational domain; and a Lagrangian approach in which observations are made at time-evolving locations along the flame front. Numerical tests indicate that the Eulerian prototype performs well even though the fire physics are non-linear and the error statistics on the parameters do not follow a Gaussian distribution. The measure of the DFS has proved that observations lead to a significant gain of information along the fire front where the fire dynamics is confined. As to the Lagrangian methodology, it has been tested for a one-dimensional configuration, where the single particle represents the front position, and shown potential for further investigations in 2D. Both proposed data-driven modeling strategies appear to provide a valuable solution to the problem of integrating fire sensor observations into fire models. These strategies also correspond to an innovative application of data assimilation to the area of combustion and fire science.

keywords: wildfire, fire modeling, CFD, data assimilation, fire forecast, flame spread.

Introduction

There are three principal means of acquiring knowledge...
observation of nature, reflection, and experimentation. Observation collects facts;
reflection combines them; experimentation verifies the result of that combination.
Denis Diderot

Scientific context

Predicting the speed and the direction in which a forest fire will propage is directly in link with public safety and environmental protection issues. The modeling of this natural disturbance is indeed a management tool for ecosystems worldwide so as to control their growth and preservation. This could avoid the development of extensive fires and measure the a posteriori impacts of a fire, in particular on the atmosphere. However, it remains a scientific challenge as its rate of spread depends on the multi-scale interactions between multi-physics processes: the combustion, the flow dynamics at the flame scale and the atmospheric dynamics. These processes are highly connected to the local vegetation characteristics, topography and weather conditions. Wind increases indeed the fire spread in the wind direction, or attenuates it when opposed to its propagation. Higher temperature makes the fire burn faster, while higher relative humidity and precipitation may slow it down and even extinguish it. As to topographical conditions, their variations imply changes in the solar orientation and in the vegetation structure, both affecting the fire spread.
In such a multi-physics multi-scale problem, a fire model does not account accurately for all the relevant physical processes. Many parameters of the model may be unknown: what is burning, at what speed, in which direction, what is the fuel distribution, what is the local humidity, how much heat is generated, etc? And yet their interactions are of first importance to characterize the fire propagation in terms of direction, speed and intensity.

Due to the complexity of the fire process and to the lack of a fully physical model, the scientific community has initiated different projects so as to monitor the fire front spread and its associated emissions with satellite observations. Beyond observations led by the projects MACC[1] in Europe and FLAMBE[2] in the US, many efforts have been made on the development of wildfire modeling [1][2][3]. In France, the coupling of combustion, fire physics and atmosphere dynamics has been carried out within the project ANR-COSINUS-IDEA, developed as a collaboration between the University of Corte, CERFACS, Météo-France, the CNRS laboratory EM2C at *Ecole Centrale Paris* and the *Laboratoire d'Aérologie* at *Observatoire Midi-Pyrénées*. The objective is to build a simulation tool of extensive open fires, coupling the fire dynamics and the atmospheric emissions (carbon, trace gases, aerosols) within an operational time frame.
Still, the uncertainties in the models are significant. Like all models in computational sciences, fire models need to strike a balance between accuracy, availability of data, and fast execution. All physical processes are not taken into account as a full three-dimensional treatment of wildfires by DNS[3] at scales relevant for atmospheric modeling would be beyond current supercomputer capacities. Instead of a complete physical model, many semi-empirical fire spread equations have been therefore developed for a quick estimation of fundamental parameters such as the fire spread rate. Fire modeling implies therefore some parametrizations which introduce necessarily errors in the physics and uncertainties in the model parameters. In particular, the quality of a fire model mainly relies on the parametrization of the rate of spread. This study focuses on the calibration of these parameters of the model. In other words, it aims at identifying the value of these

[1] Monitoring Atmospheric Chemistry and Climate = current service of the European Global Fire Assimilation System program which provides in real-time data on the atmospheric composition and in particular on the biomass burning emissions.
[2] Fire Locating And Modeling of Burning Emissions = global monitoring and forecasting system of biomass-burning smoke.
[3] Direct Numerical Simulation.

parameters to be more consistent with reality.

Parameter calibration can be formulated as an inverse problem [4] and can be solved using data assimilation approach. Data assimilation combines both numerical and observational information of a system, in order to provide an optimized description [5][6][7]. This approach is based on the estimation of the error statistics for the numerical and observational information. Its benefit has already been greatly demonstrated in meteorology [8][9] and oceanography [10] over the past decades, especially for providing initial conditions for numerical forecasts. Data assimilation is now being applied with increasing frequency outside these original domains of application, for instance to hydrology. It offers therefore an efficient framework to reduce the uncertainty on the parametrization of a fire propagation model and as a consequence on the forecast of a fire propagation.

To this purpose, the collaboration between CERFACS (Dr. Sophie RICCI) and the Department of Fire Protection Engineering at UMD (Prof. Arnaud TROUVE) has been initiated. This project forms indeed a very innovative application of advanced methods for coupling information from observations and models to the area of combustion and fire science. CERFACS has indeed a strong expertise in both data assimilation and combustion, while UMD focuses on the physics of fire and builds advanced fire models.

This study presents the data assimilation approach in the context of wildfire propagation. Examples of recent similar efforts in the context of compartment fires may be found in references [11][12]. A prototype was built on top of a simple model to prove the feasibility of this approach for wildland fire applications. This work focuses therefore on the method of data assimilation itself, and is aimed at determining which is the suitable strategy for wildfire applications. As highlighted by Mandel's preliminary work [13], this feasibility study does not require the development of a complex propagation model. Here a two-dimensional combustion solver is used to simulate the evolution of a wildfire in a layer just above the surface. This model based upon the reaction-diffusion equation integrates the main features of a fire: a kinetic term is indeed coupled to diffusion so as to create a propagating front in a domain where the vegetation may be randomly spread. It introduces the rate of spread as primary parameter of the model. In this approach, the rate of spread is assumed to be linearly dependent upon the vegetation distribution. It is then assumed here, that the uncertainty on the wildfire modeling is due mostly to the uncertainty on the constant of proportionality between the rate of spread and the vegetation distribution. So this formulation describing the evolution of a progress variable reduces the uncertainty to one single control parameter.

The data assimilation prototype was built in the context of Observing System Experiment (OSE), meaning that the observations are generated using the numerical model itself. Observations result from the integration of the fire model with a given parameter (referred to as the true control parameter): they are either measurements of the progress variable at spatial fixed locations over the computational domain, or positions of the fire front over time. The physics of fire is indeed described by the propagation of an interface separating the burned region from the unburned region. So a Lagrangian assimilation might appear as a better tool to track the trajectory of the flame over time. In the course of the internship, both approaches, Eulerian and Lagrangian, will therefore be investigated. Starting from an a priori value of the control parameter (different from the true value), called the background value, the objective of this investigation is to show how efficient are these approaches to correct the background parameter and to converge towards the true value. Given the relatively small dimension of the problem, a simple filtering technique, further referenced as the Best Linear Unbiased Estimator (BLUE), is applied. This will be the basis of numerical studies, leading to a simple and fast integration of data assimilation tools for fire propagation.

A Franco-American collaboration

However, applying data assimilation to fire propagation raises special challenges as this is a phenomenon of interface, where most of the dynamics of the system is confined within a very thin zone along the flame front, which might be difficult to track over time. Solving them requires a multi-institutional approach so as to combine the expertise already existing in the different fields involved in this multi-physics multi-scale problem. This is the primary motivation in the collaboration between CERFACS and UMD.

CERFACS, a partnership GLOBC-CFD-AE

Since the end of the 1980s, CERFACS is a well-known international institute for high performance computing, which aims at developing advanced methods for the algorithmic resolution and numerical simulation of very large scale scientific and technological problems. These problems are of interest to both research and industry, and require the most powerful supercomputers currently available.

With the benefit of worldwide collaborations, this organization gathers about 120 employees, among whom physicists, applied mathematicians, numerical analysts and software engineers, coming from more than 10 different countries. They are involved in 7 different research fields: parallel algorithms, code coupling (with OASIS and PALM softwares), data assimilation, aerodynamics, combustion, climate and environment, and finally electromagnetism and acoustics.

With such a wide range of activities, this research environment stimulates the development of multiphysics projects involving more than one research team, as for this project on fire propagation. As it includes components from computational physics and environmental sciences, it is a collaborative work between three research entities:

- GLOBC[4], with Dr. Sophie RICCI and Dr. Andrea PIACENTINI.
  Strongly involved in the research on climate change and variability, this entity works partly on data assimilation. Four main areas of applications are presently explored (atmospheric chemistry, oceanography, hydrology and neutronics), but one objective is to widen the scope of applications, for instance to fire propagation.

- CFD[5], with Dr. Bénédicte CUENOT and Dr. Thierry POINSOT.
  This entity is involved in all problems related to aerodynamics and combustion with high performance computing, so as to apply LES[6] techniques to model turbulent flows and turbulent combustion. The AVBP solver has been jointly developed by CERFACS and IFP, the French Institute of Petroleum, to perform parallel compressible LES computations, and is specifically designed to simulate industrial gas turbines, aero gas turbines, rocket engines, and laboratory burners.

- AE[7], with Dr. Roberto PAOLI and Dr. Sébastien MASSART.
  The goal is to study the effect of aircraft emissions on atmospheric chemistry and on the radiative balance of the atmosphere by developing a variational approach of data assimilation. Soot particles trigger indeed the formation of cirrus clouds, and emission of nitrogen oxides perturbs the natural chemical cycles, leading to an additional contribution to the green house forcing like the particles emitted by a fire.

Beyond research, CERFACS expands its missions to provide advanced training on high performance computing. This private research company funded in 1987 takes the form of a *société civile* under the French law. Seven shareholders are part of the company board: CNES, the French Space Agency; EADS France; EDF, Electricité de France; Météo-France, the French meteorological service; ONERA, the French Aerospace Laboratory; SAFRAN, an international high-technology group; and TOTAL, a multinational energy company. Furthermore, CERFACS has established strong partnerships with CNRS, the National Center for Scientific Center, for its activities related to climate and environment, and with CEA, the Commission for Atomic Energy, in the field of advanced computing.

Department of Fire Protection Engineering at UMD

Located at the border with Washington D.C. in College Park, in the state of Maryland, the University of Maryland was founded in 1856 and was dedicated originally to agricultural studies. With 112 graduate degrees spread over 13 different colleges and schools, among whom the A.J. Clark School of Engineering, it

[4]Global Change and Climate Modeling.
[5]Computational Fluid Dynamics.
[6]Large Eddy Simulation.
[7]Aviation and Environment.

enrols about 35,000 students (including 10,000 postgraduates) and is nowadays recognized as one of the top public North-American universities.

Since 1956, the Fire Protection Engineering Department belongs to the School of Engineering and offers the only full ABET[8]-accredited undergraduate program and one of the two graduate degree programs in the US. The associated Master of Science or Master of Engineering, graduating about 30 students per year, includes basically scientific studies on fire modeling and combustion behaviour as well as courses related to risk analysis techniques.
The department composed of 8 faculty members, among whom my supervisor Dr. Arnaud Trouvé, focuses on recent advances in material testing practices, fire detection, performance-based design and modeling techniques to predict fire growth, smoke movement or the response of building systems in design and fire investigation applications. These investigations are notably performed via FDS[9], a simulator solving computational fluid dynamics model of fire-driven fluid flow, notably in building systems, and developed by NIST[10]. Currently, more than 800 graduates from the department are employed in industry, insurance companies, Federal, state or local government, military, and fire service.

Unlike combustion, scientific investigations on fire behavior and spread are restricted to some research centers in the world. For instance, the equivalent of the Department of Fire Protection Engineering in Europe is part of the University of Edinburgh, Scotland, which has been among the first universities (with UMD) to offer a degree in Fire Engineering and had its first research group on fire in the 1970s. Through the BRE[11] Centre for Fire Safety Engineering, its current mission is to develop a real-time emergency response system for enclosure fires. This is a challenging task as the most advanced technologies shall be used so as to limit the computational cost to real-time.

Motivations

With the Franco-American collaboration between CERFACS and the University of Maryland, this internship has been an outstanding experience and has provided a relevant framework to work on a multi-scale multi-physics problem. This has required the interaction between different research communities (environmental, combustion and fire science). CERFACS is indeed a unique structure combining very different skills in a wide range of science and engineering problems, from combustion and aerodynamics to climate change and oceanography. As a reference in the fire research community, UMD brings the expertise in fire science at very different scales, from the laboratory experiments to the simulation of enclosure fires.
Thanks to my strong international experience, I have been motivated to help to promote this international collaboration and to learn as much as possible on the different components of a fire, from basic combustion sciences, environmental sciences (description of biomass fuel, small-scale topographical and meteorological conditions), atmospheric sciences (large-scale topographical and meteorological conditions) to computational physics, applied mathematics and computer science. With such a framework, I have been able to study each subdomain in details, and at the same time to draw the big picture of the project and of the fire phenomenon.

Furthermore, from a technical perspective, this project consists in what is considered as a very innovative application of advanced methods for coupling observations and models that are developed in related scientific and engineering fields (e.g. weather forecasting) to the area of combustion and fire science. As a future engineer in numerical modeling, it has been a perfect opportunity to complete my background and to assimilate stronger knowledge in statistics and inverse modeling. The combination of numerics and statistics allows indeed the reduction of the degree of details in the physical model, a loss which may be balanced by the direct observations. Hence, it appears as a key approach for operational frameworks when the computational time shall fit with the decision time frame.

This internship is also a first phase in a wider and longer program, leading to a PhD dissertation. In the context of fire management, this innovative approach is motivated by the urgent need for an operational tool

[8] Accreditation Board for Engineering and Technology.
[9] Fire Dynamics Simulator.
[10] National Institute of Standards and Technology.
[11] Build Reseach Establishment.

forecasting the development of a fire given weather, topography and vegetation conditions, with a limited computational cost. An operational model will be helpful at three different levels: emergency response, anticipation, and risk control. Firstly, it would give an insight of which zones will be affected by the disaster and bring significant information to the rescue team. Secondly, it would help to study which regions are sensitive to an ignition of a wildfire by integrating the local topography and mapping the fuel load, and to build scenarii for a wide range of conditions. Furthermore, a fire has positive effects on the ecological systems by stimulating growth without accumulation, so such a model would also be useful to generate controlled fires and thus to prevent any fire disaster. To this purpose, a new approach is required. It has therefore been captivating to work on defining the strategy which could help the fire community in the future, and thus motivating to introduce a new paradigm of great potential for having important safety and environmental impact.

So this internship appears as the initiation of a project of great scope which could lead on the long-range to a better understanding of the fire process and of its interactions with the environment, and to a useful tool for emergency responses. These perspectives match my strong interest in research and advanced modeling in geosciences.

Glossary

Data assimilation variables

In this thesis, the variables used specifically for data assimilation are adapted from the notation defined in the article from Ide et al. [5]. Note that random variables are usually denoted in capital letters (X, Y,...), whereas one of their realizations is denoted in minuscule letters (x, y,...). Vector or matrix variables are denoted in bold (for instance, $\mathbf{X}$ or $\mathbf{A}$).

Dimension

- n: dimension of the control vector $\mathbf{X}$.
- p: number of assimilated observations, e.g. the length of the observation vector $\mathbf{Y}^o$.

Variables

- $\mathbf{X}$: the control random variable, called the *control vector*, with $\mathbf{x}$ a realization.
- $\mathbf{x}^t$: a non-random variable which represents the true value of the control parameters, called the *true control vector* (denoted by "t" for "true").
- $\mathbf{X}^b$: the background random variable which defines an a priori knowledge of the model state, called the *background vector*, with $\mathbf{x}^b$ a realization (denoted by "b" for "background").
- $\mathbf{X}^a$: the analysis random variable which defines the optimal parameters resulting from data assimilation, called the *analysis*, with $\mathbf{x}^a$ a realisation (denoted by "a" for "analysis").
- $\mathbf{X}^g$: the reference random variable, in the vicinity of which the operator H and/or M is linearized.
- $\mathbf{Y}^o$: the observation random variable, which contains the experimental measures of the system and which is called the *observation vector*, with $\mathbf{y}^o$ a realization (denoted by "o" for "observation").

Operators

- H: the observation operator, with $\mathbf{H}$ its linear tangent operator.
- M: the model operator which defines the integration of the equations over time, with $\mathbf{M}$ its linear approximation.
- S: the selection operator which defines how observations are extracted from the simulated fields with a prescribed spatial and time frequency, containing only 0 and 1 values.

Errors/Covariance matrices

- $\epsilon^b = \mathbf{X}^b - \mathbf{x}^t$: the random variable of background errors.
- $\epsilon^o = \mathbf{Y}^o - \mathbf{H}\mathbf{x}^t$: the random variable of observation errors.
- $\mathbf{B}$: the covariance matrix for background errors.
- $\mathbf{R}$: the covariance matrix for observation errors.

- $\mathbf{A}$: the covariance matrix for analysed errors.
- $\mathbf{I}$: the identity matrix.
- $\mathbf{K}$: the Kalman filter.
- $\mathbf{d}^{ob} = \mathbf{Y}^o - H(\mathbf{X}^b)$: the innovation vector, measuring the discrepancies between the observation vector and the background in the observation space.
- $\mathbf{d}^{oa} = \mathbf{Y}^o - H(\mathbf{x}^a)$: the analysis residual in the observation space.
- $\mathbf{d}^{ab} = H(\mathbf{X}^a) - H(\mathbf{X}^b)$: the residual between the analysis and the background in the observation space.

Functions/Distributions

- J: the cost function minimized within the framework of data assimilation.
- $\mathcal{N}(m, \sigma)$: the Gaussian distribution, also called the normal distribution, of mean m and standard deviation σ (if this distribution is a vector, σ defines a covariance matrix).

Combustion variables

- T : temperature.
- T_{ig}: ignition temperature.
- T_1: fresh gas temperature.
- T_2: burnt gas temperature.
- Y_F: mass fraction.
- θ: reduced temperature.
- θ_c: reference reduced temperature identifying the position of the front.
- x_c, (x_c, y_c): position of the fire front (1D, 2D).
- Y: reduced mass fraction.
- D: diffusion coefficient.
- a: reaction coefficient.
- ρ: density.
- Le: Lewis number.
- s_L: flame speed.
- δ_L: flame thickness.
- τ_L: response time of the system.
- $s_{L,KPP}$: flame speed provided by the KPP analysis.
- $\delta_{L,KPP}$: flame thickness provided by the KPP analysis.
- β: numerical parameter defining the flame thickness.
- $s_{L,d}$, s_{L,d_1}, s_{L,d_2}: diagnostics of the flame speed.
- $\delta_{L,d}$: diagnostic of the flame thickness.

- $\tau_{L,d}$: diagnostic of the response time of the system.
- δ, Δx, Δy: mesh size (minimum, along the x-axis, along the y-axis).
- Δt: time step.
- F: Fourier number.

Acronyms

- AMB or BMA: Analysis Minus Background.
- BLUE: Best Linear Unbiased Estimator.
- BMO or OMB: Observation Minus Background.
- CFD: Computational Fluid Dynamics.
- DFS: Degrees of Freedom for Signal.
- EBU: Eddy Break Up.
- EnKF: Ensemble Kalman Filter.
- KPP: Kolmogorov-Petrovsky-Piskounov.
- PDF: Probability Density Function.
- RK4: Runge-Kutta 4.
- RMS: Root Mean Square.
- TMA or AMT: True Minus Analysis.
- TMB or BMT: True Minus Background.
- VOC: Volatile Organic Compounds.

Outline

This research work is divided into three parts.

The *first part* presents the main principles associated with data assimilation and parameter calibration. While chapter 1 introduces the mathematical quantities required to apply this methodology and the modeling of the uncertainties with error covariance matrices, a particular attention is then given to the BLUE algorithm and to the OSE framework in chapter 2. The behavior of the data assimilation algorithm is illustrated, in chapter 3, using a 1D sample model based on the diffusion equation and assimilating a single parameter, the diffusion coefficient.

In the *second part*, the objective is to present the Partial Differential Equation (PDE) model to represent the propagation of a fire front given an a priori vegetation distribution. Chapter 4 presents the main processes involved in the propagation of a wildfire. As in Jan Mandel's work, the fire propagation is based on conservation equations and more precisely on the reaction-diffusion equation with the fire modeled as a premixed flame in chapter 5. The derivation of the model from the standard reaction-diffusion form to an equation with the local rate of spread as primary physical quantity is highlighted in chapter 6. Both models were checked against an analytical solution, so as to validate the diagnostics of the flame properties in terms of flame rate of spread and thickness.

The *third part* shows the different strategies experimented in the context of parameter calibration, either with an Eulerian approach in chapters 7 and 8 or with a Lagrangian approach in chapter 9. It presents results from a series of tests that evaluate the ability of data assimilation analysis to calibrate the control parameter(s). More precisely, the impact of the observations on the assimilation algorithm, quantitatively as well as qualitatively, was investigated in chapter 7 for a single control parameter, the diffusion coefficient. A useful diagnostic is given by the DFS, which measures directly the contribution of observations to the analysis. This primary study leads to the assimilation of the propagating speed of the fire front in chapter 8, which is the outcome of this thesis. Chapter 9 explores the potential of Lagrangian assimilation for fire applications.

A *conclusion* summarizes the main achievements of this thesis, which open the way to further developements.

Contents

Part I

Data Assimilation, Concepts, Methods and Applications

Introduction

Data assimilation appeared at the end of the eighteenth century, with scientific scholars such as Johann Tobias Mayer (1723-1762), Adrien-Marie Legendre (1752-1834), Pierre-Simon Laplace (1749-1827) and Karl Friedrich (1777-1855), as a statistical method able to estimate the state of a dynamical system by combining all available sources of information. Considering the observations as a quantitative tool, this method developed in the course of the next century, within the framework of astronomy, as a fundamental tool in the theory of celestial movement. Mayer computed the motions of the Moon with an outstanding accuracy by introducing the instrumental errors in its calculcations and repeating measures so as to reduce their uncertainty. Limited to a linear adjustment, this method was generalized later by Legendre and is currently known as the least-squares method. Nevertheless, it is rather difficult to define the paternity of this optimization method as twelve years before Legendre, Gauss used implicitly this method to predict the future location of the newly discovered asteroid Ceres in 1801, without solving the complicated Kepler's nonlinear equations of planetary motion but using a least-squares analysis. However, Legendre was the first to publish the method in 1805. These developments led to the *Gauss-Markov theorem*, stating that in a linear model where errors are of zero average, uncorrelated and have equal variance, the optimal solution is given by the least-squares estimator.

During the twentieth century, further works in statistics enhanced the development of the method, with the concept of probability density function with Sir Ronald Aylmer Fisher (1890-1962), and of optimal filters with Norbert Wiener (1894-1964), Andrei Kolmogorov (1903-1987) and Rudolf Emil Kalman (1930-). This led in the 1960s to the recursive optimal filter, commonly known as the *Kalman filter* and widely used in control theory like navigation systems, for the Apollo program and more recently for the International Space Station. It is equivalent to a variational approach of data assimilation (under some assumptions), a method explored by Yoshi Sasaki during his work on the trajectory of hurricanes.

Application to geosciences was initiated in 1963 by Gandin in reply to the operational need of weather forecast and extented at the end of the 1990s to oceanography. For such a system, the challenge is to take into account as best as possible all the physical processes to determine the air temperature, among whom the strong interplay between ocean and atmopshere. They cannot be defined with the only use of mathematical equations due to the complex dynamics and to the large number of state variables involved. Thus, observations have to be combined with the model through an optimal interpolation: each source of information has a weight in the estimation of the state of the system, the most weight given to the source with the least uncertainty. This idea is at the core of data assimilation.

This part of the thesis introduces the main principles associated to data assimilation and more precisely to parameter calibration, widely developed at CERFACS for applications in oceanography and hydrology. The BLUE algorithm will be presented for a 1D sample model, the diffusion equation, so as to point out its key points and to introduce a powerful tool to validate the implementation of the method, the so-called Observation System Experiment (OSE).

1. Basic Concepts

Data assimilation combines optimally all sources of information on a system (observations, physical properties) to produce a more realistic image of its control parameters than if either source of information were taken separately. Each of these sources is subject to an uncertainty due to the model approximations as well as to the measurement and representativeness errors. The statistics on the background and on the observation errors as well as their correlations are formulated in terms of covariance matrices and are taken into account as such in the data assimilation algorithm. The BLUE algorithm used in the present study can indeed be considered as a generalization of a least-squares problem where each source is weighted by its precision, modeled as the inverse of its error covariance matrix.

1.1 Data assimilation variables

1.1.1 Control vector

The state vector is formed by the finite number of data which represents the discrete state of the model, in other words the simulated field(s) defined at the grid points of the computational domain. The analysis problem is in general not solved for all components of the model state as the dimension of the system can be beyond computer capacities (about 10^6 variables in meteorology). Additionally, it does not only take into account the state variables but also model parameters if they are subject to critical uncertainties. So the idea is to reduce the number of variables to calibrate and to focus the assimilation on those which have the highest uncertainty and to which the system is highly sensitive. These variables are gathered to form the control vector $\mathbf{X}$. This vector is therefore not systematically in the same space as the state vector.

In the context of parameter calibration, the control vector is reduced to a set of n parameters, defining the control space. It is an approximation of a reference, known as the *true control vector* $\mathbf{x}^t$, which represents the true values of these n parameters which are, in reality, completely unknown. Data assimilation aims at determining an optimal value of the control vector, called the analysis and denoted by $\mathbf{X}^a$, which is closer to $\mathbf{x}^t$ than to the background $\mathbf{X}^b$, the a priori value of the control vector.

The integration of the model using the analysis parameters leads to simulated fields that are closer to the observations than the simulated fields resulting from the integration using the background parameters. Nevertheless, the simulated fields does not exactly fit the observations like in a least-squares problem since observation errors are introduced.

1.1.2 Observation vector

Even though they may be sparse in time and space, observations of the system give additional information on the dynamics of the system, provided that they are independent of each other. If some are not independent, they do not bring more information on the system and as a consequence they can be removed from the assimilation process.

Gathered in one vector $\mathbf{Y}^o$ of length p, they represent, in the framework of OSE, measurements of the simulated fields (the state variables) at some fixed spatial locations over the computational domain. They may help to integrate more physical elements in the simulation, which are not considered in the model.

1.1.3 Observation operator

As the background and observational information need to be combined in the course of data assimilation, an operator H mapping a parameter from the control space onto the observation space is required. This observation operator is generally non-linear as a composition of a model integration M (from model parameters to state variables) and of an interpolation process (from grid points to observational points). In this study, the interpolation process is reduced to a selection process S as the observations are located at some grid points. So H is defined by equation (1.1).

$$H(\mathbf{X}) = S\,o\,M(\mathbf{X}) \tag{1.1}$$

In practice, measurements are not perfect and the determination of H implies some assumptions and therefore uncertainties, denoted by ϵ^o. The problem comes down to solve an *inverse problem*: given the available observations $\mathbf{Y}^o$, the objective is to approximate as best as possible the associated physical control vector $\mathbf{x}^t$ satisfying $\mathbf{Y}^o = H(\mathbf{x}^t) + \epsilon^o$.

The formulation of the BLUE algorithm requires the linearization of H, denoted by $\mathbf{H}$, which is identified as the Jacobian matrix in the Taylor expansion of H in the vicinity of the background value of the control vector $\mathbf{X}^b$:

$$\mathbf{H} = \nabla H(\mathbf{X}^b) \tag{1.2}$$

$\mathbf{H}$ is called the linear tangent of H.

1.2 Modeling of the errors

As the true control vector $\mathbf{x}^t$ is unknown, the error on the background $\mathbf{X}^b$, denoted by ϵ^b, and on the observations $\mathbf{Y}^o$, denoted by ϵ^o, are also unknown. As a consequence, the background and observation error covariance matrices, denoted by $\mathbf{B}$ and $\mathbf{R}$ respectively, can only be estimated using an error covariance model.

The modeling of the errors is performed from a statistical point of view. If a large number of experiments were undergone under exactly the same conditions, the associated errors would be different each time, but statistics such as expectation value and variance could be established. These two first statistical moments would then converge to values which depend only on the physical processes responsible for the errors, and no longer on any particular realization of these errors. So a statistical model may appear as the reasonable process to approach the errors present in the system.

The best information about the distribution of these errors is given by the PDF (Probability Density Function) function. It describes the relative likelihood for these errors to occur at a given point in the control or observation space, and gives information on their expectation value and variance. This PDF is modeled by a Gaussian function. This is a reasonable assumption as only the first two moments of the distribution are considered, meaning that any distribution is reduced to a Gaussian approximation.

1.2.1 Background errors

The background error ϵ^b is defined as the difference between the background $\mathbf{X}^b$ and the true control vector $\mathbf{x}^t$ with $\epsilon^b = \mathbf{X}^b - \mathbf{x}^t$. The statistics of ϵ^b are described in a square symmetric, positive definite matrix $\mathbf{B}$ of size $n \times n$, such that:

$$\mathbf{B} = \mathbb{E}[\epsilon^b \cdot {\epsilon^b}^T] \tag{1.3}$$

where the diagonal elements of $\mathbf{B}$ represent the error variance for each control parameter, while the off-diagonal terms stand for the covariances between the errors. This means that if $n = 1$, $\mathbf{B}$ is a scalar and is fully described by the variance associated to the single control parameter considered.

Considering two control variables v_k and v_q among n, associated to errors e_k and e_q, their covariance is defined such that:

$$cov(e_k, e_q) = \rho(e_k, e_q) \cdot \sqrt{var(e_k)\,var(e_q)} \tag{1.4}$$

with $\rho(e_k, e_q)$ the correlation coefficient between e_k and e_q, satisfying $0 < \rho(e_k, e_q) < 1$.

$\mathbf{x}^b$ is the realization of the random variable $\mathbf{X}^b$ that is assumed to follow a Gaussian distribution $\mathcal{N}(\mathbf{x}^t, \mathbf{B})$. As the background errors are assumed to be of zero average,

$$\epsilon^b \sim \mathcal{N}(0, \mathbf{B}) \tag{1.5}$$

1.2.2 Observation errors

As to the background, the observations are represented by a random variable $\mathbf{Y}^o$ that is assumed to follow a Gaussian distribution $\mathcal{N}(H(\mathbf{x}^t), \mathbf{R})$ (provided that $H(\mathbf{x}^t)$ is a non-random variable) with the error covariance matrix

$$\mathbf{R} = \mathbb{E}[\epsilon^o \cdot \epsilon^{oT}] \tag{1.6}$$

As the observation error is defined as the difference between the observations and the true control vector projected onto the observation space such that $\mathbf{Y}^o = H(\mathbf{x}^t) + \epsilon^o$, assuming it is unbiased and uncorrelated, ϵ^o follows a Gaussian distribution

$$\epsilon^o \sim \mathcal{N}(0, \mathbf{R}) \tag{1.7}$$

In practice, ϵ^o may be random. So a new observation error, $\tilde{\epsilon^o} = \epsilon^o + \delta\mathbf{H}\mathbf{x}^t$ with the extra additive term $\delta\mathbf{H}$ of zero average, is defined. Hence,

$$\mathbf{Y}^o = H(\mathbf{x}^t) + \left(\epsilon^o + \delta\mathbf{H}\mathbf{x}^t\right) = H(\mathbf{x}^t) + \tilde{\epsilon^o} \tag{1.8}$$

Furthermore, observed quantities are not necessarily the same as the control variables. The transformations required to map one variable from the control space onto the observation space do not change the analysis problem, only its representation. However, they insert some unvavoidable errors due to the conversion between the observed values and their equivalents in the model state (independently from the observation and background errors), called the representativeness errors. They do not appear in this stand-alone numerical feasibility study as in the context of OSE, the observations represent the same physical quantities as in the model.

1.3 Analysis, the result of data assimilation

By accumulating the information from observations into the model state, data assimilation produces an analysis $\mathbf{x}^a$, that is to say a more accurate image of the true control vector $\mathbf{x}^t$ than the background at a given time. It means that the optimal solution $\mathbf{x}^a$ gives a better diagnostic of the system than the observations and the numerical model considered separately. Consequently, it can be used as an initial condition for a numerical forecast of the system or as a reference against which to check the quality of some observations.

1.3.1 The analysis formulation

The resolution of most data assimilation algorithms relies on the minimization of a cost function J_{3DVAR} (variational approach referred to as 3DVAR) defined in equation (1.9):

$$J_{3DVAR}(\mathbf{X}) = \frac{1}{2}\left(\mathbf{X} - \mathbf{X}^b\right)^T \mathbf{B}^{-1}\left(\mathbf{X} - \mathbf{X}^b\right) + \frac{1}{2}\left(\mathbf{Y}^o - H(\mathbf{X})\right)^T \mathbf{R}^{-1}\left(\mathbf{Y}^o - H(\mathbf{X})\right) \tag{1.9}$$

This cost function formulates the difference between the background and the control vector on the one hand, and the difference between the observations and the control vector (expressed in the observation space) on the other hand, where each term is weighted by the inverse of its error covariance matrix.

The objective is to determine the control vector $\mathbf{X}$ which leads to a zero gradient of J_{3DVAR} and thus a more realistic value of the control parameters. Either performed at an instantaneous time or over a period of time (called an assimilation window), the solution, called the analysis $\mathbf{X}^a$, is optimal in the sense that it

minimizes the variance of the distance to the true control vector $\mathbf{x}^t$. If H is linear (e.g., $H = \mathbf{H}$), $\mathbf{X}^a$ can be viewed as a correction $\delta\mathbf{X}^b$ applied to the background:

$$\mathbf{X}^a = \mathbf{X}^b + \delta\mathbf{X}^b \tag{1.10}$$

Note that this correction term $\delta\mathbf{X}^b$ is, in the case of an assimilation window, smooth in time and as a consequence physically more realistic.

A first estimation of $\mathbf{X}^a$ is provided by the *Cressman analysis*. At each grid point denoted with index j, the analysis is given by:

$$\mathbf{X}^a(j) = \mathbf{X}^b(j) + \frac{\sum_{i=1}^{p} \omega(i,j)\Big(\mathbf{Y}^o(i) - \mathbf{X}^b(i)\Big)}{\sum_{i=1}^{p} \omega(i,j)} \tag{1.11}$$

with $\mathbf{X}^b(i)$ the background variable interpolated at observation point i, and $\omega(i,j)$ the weight function which defines the reliability of each information. In this simple approach, it appears that the correction is proportional to the distance between the observations and the control vector, the so-called innovation vector. However, this is not sufficient to guarantee a correct analysis in the sense that it may not cope with the physical features of the true system, such as the smoothness of the fields and the relationships between the variables.

A more appropriate analysis can be defined using a linear combination of the observations and the background. $\mathbf{X}^a$ is then defined by equation (1.12):

$$\mathbf{X}^a = \mathbf{X}^b + \mathbf{B}\mathbf{H}^T(\mathbf{H}\mathbf{B}\mathbf{H}^T + \mathbf{R})^{-1}\mathbf{d}^{ob} \tag{1.12}$$

with $\mathbf{d}^{ob}$ the innovation vector such that $\mathbf{d}^{ob} = \mathbf{Y}^o - H(\mathbf{X}^b)$, where $H(\mathbf{X}^b)$ is the equivalent of the background in the observation space. Integrating the model with the analysed set of parameters results then in a better estimate of the state of the system.
This approach is based on the *Gauss-Markov theorem*, stating that the best linear estimation of the weight coefficients is given by the least-squares estimator (when errors are of zero average, equal variance and zero covariance) and more generally by the *Aitken estimator* (when errors are of zero average and of any covariance), known as the Best Linear Unbiased Estimator (BLUE).

1.3.2 A basic example

To show how data assimilation can reduce the uncertainty in the system, the estimation of a variable $\mathbf{X}$ using two observations $\mathbf{y}_1^o$ and $\mathbf{y}_2^o$ is derived here. In this analysis, observations are subject to errors which are some realizations of two random variables ϵ_1^o and ϵ_2^o. These errors have a zero expectation and are therefore completely described by their standard deviations σ_1 and σ_2, so $\mathbb{E}[\epsilon_i^o] = 0$ and $\mathbb{E}[(\epsilon_i^o)^2] = \sigma_i^2 \ \forall i$. Additionally, the measurement errors between the two observations are supposed to be non-correlated. This means that $\mathbb{E}[\epsilon_i^o \cdot \epsilon_j^o] = 0$ for $i \neq j$.

The estimation $\mathbf{x}^a$ of the true control vector $\mathbf{x}^t$ is defined as a linear combination of the two observations $\mathbf{y}_1^o$ and $\mathbf{y}_2^o$ such that:

$$\mathbf{x}^a = k_1\,\mathbf{y}_1^o + k_2\,\mathbf{y}_2^o \tag{1.13}$$

The coefficients k_1 and k_2 need to be determined so as to obtain an optimal analysis, which shall be an unbiased estimation of $\mathbf{x}^t$ and which shall minimize the variance σ^2 with respect to k_1 and k_2. This leads to relations (1.14) and (1.15):

$$\begin{aligned} \mathbb{E}[\mathbf{x}^a - \mathbf{x}^t] &= 0 \\ &= \mathbb{E}[k_1\mathbf{y}_1^o + k_2\mathbf{y}_2^o - \mathbf{x}^t] \\ &= (k_1 + k_2 - 1)\,\mathbf{x}^t \\ \Rightarrow k_1 + k_2 &= 1 \end{aligned} \tag{1.14}$$

$$
\begin{aligned}
\sigma^2 &= \mathbb{E}[(\mathbf{x}^a - \mathbf{x}^t)^2] \\
&= \mathbb{E}[(k_1 \mathbf{y}_1^o + k_2 \mathbf{y}_2^o - \mathbf{x}^t)^2] \\
&= k_1^2\, \mathbb{E}[\epsilon_1^{o2}] + k_2^2\, \mathbb{E}[\epsilon_2^{o2}] + 2k_1k_2\, \mathbb{E}[\epsilon_1^o \cdot \epsilon_2^o]] \\
\Rightarrow \sigma^2(k_1) &= k_1^2\, \sigma_1^2 + (1-k_1)^2\, \sigma_2^2
\end{aligned} \tag{1.15}
$$

By minimizing the variance, i.e. $\partial\sigma^2/\partial k_1 = \partial\sigma^2/\partial k_2 = 0$, it follows that:

$$
\left\{
\begin{array}{l}
k_1^a = \frac{\sigma_2^2}{\sigma_1^2+\sigma_2^2} \\
k_2^a = \frac{\sigma_1^2}{\sigma_1^2+\sigma_2^2}
\end{array}
\right. \tag{1.16}
$$

So the optimal analysis is given by (1.17):

$$
\mathbf{x}^a = \Big(\frac{\sigma_2^2}{\sigma_1^2+\sigma_2^2}\Big)\mathbf{y}_1^o + \Big(\frac{\sigma_1^2}{\sigma_1^2+\sigma_2^2}\Big)\mathbf{y}_2^o \quad \Rightarrow \quad \frac{\mathbf{x}^a}{\sigma_a^2} = \frac{\mathbf{y}_1^o}{\sigma_1^2} + \frac{\mathbf{y}_2^o}{\sigma_2^2} \tag{1.17}
$$

with its associated variance σ_a^2, satisfying $\sigma_a^2 < \sigma_1^2$ and $\sigma_a^2 < \sigma_2^2$, such that:

$$
\sigma_a^2 = \frac{\sigma_1^2\sigma_2^2}{\sigma_1^2+\sigma_2^2} \tag{1.18}
$$

In a general case, these observations can be provided by different sources of information on the system, either from the model or by direct measurements. In this example, the analysis evolves in the same space as in the observations. It can therefore be viewed as the barycenter of the measures balanced by their precision (e.g., the inverse of their variance). For a more general framework with n parameters and p observations, different approaches are possible to solve this optimization problem, among whom the BLUE, that provides the analysis in the control space and not in the observation space.

1.3.3 Principles

Data assimilation provides more realistic physical fields by integrating observations and the physical expertise through a numerical model. Despite of the number of observations available, the system is in general underdetermined, in particular when assimilation focuses on state variables. To define a well-posed mathematical problem, it is therefore necessary to add an extra source of information with an a priori estimation of the control variables, called the background, directly inserted into the control vector.

In this context, errors are limited to observations and background. Both follow a Gaussian distribution with a zero average and any covariance matrix. The resolution of the data assimilation problem requires therefore four components:

1. observations of the physical system $\mathbf{Y}^o$ and their associated errors (ϵ^o, $\mathbf{R}$),
2. a background estimation of the control vector $\mathbf{X}^b$ and its associated errors (ϵ^b, $\mathbf{B}$),
3. a model M describing the system dynamics,
4. an observation operator H with its associated linear tangent operator $\mathbf{H}$.

This approach provides a background correction proportional to the innovation vector, significant when the level of confidence in the background is low or equivalently when the level of confidence in the observations is high. This correction is projected onto the model grid and propagated in the vicinity of the observations via the background error correlations. The correction, called the analysis increment, is therefore in intensity proportional to the background and observation variance errors, and spatially determined by the associated error correlations. This leads to a better estimation of the state of the system at a given time, and therefore to a more accurate forecast of its future evolution.

2. The Best Linear Unbiased Estimator Formulation

By estimating uncertainties on the background and the observations, data assimilation gives an unbiased estimation of the analysis $\mathbf{X}^a$ *and minimizes the distance with the true control vector* $\mathbf{x}^t$*. The BLUE algorithm formulates the analysis as a linear combination of the background* $\mathbf{X}^b$ *and of the observations* $\mathbf{Y}^o$ *[14][15] such that*

$$\mathbf{X}^a = \mathbf{L}\mathbf{X}^b + \mathbf{K}\mathbf{Y}^o \tag{2.1}$$

In statistics, the Gauss-Markov theorem states that the best linear unbiased estimation of the weight coefficients is given by the least-squares estimator (when errors are of zero average, equal variance and zero covariance) and more generally by the Aitken estimator (when errors are of zero average and of any covariance), known as the BLUE [16][17].

2.1 The Aitken estimator

The Aitken estimator can be considered as a correction of the background. Using equation (2.1) and defining the error analysis $\epsilon^a = \mathbf{X}^a - \mathbf{x}^t$ of zero mean leads indeed to $\mathbf{L} = \mathbf{I} - \mathbf{K}\mathbf{H}$ [18]. Hence,

$$\mathbf{X}^a = \mathbf{X}^b + \mathbf{K}\Big(\mathbf{Y}^o - \mathbf{H}\mathbf{X}^b\Big) \tag{2.2}$$

Also, in this context, the analysis error covariance matrix reads

$$\mathbf{A} = (\mathbf{I} - \mathbf{K}\mathbf{H})\mathbf{B}(\mathbf{I} - \mathbf{K}\mathbf{H})^T + \mathbf{K}\mathbf{R}\mathbf{K}^T \tag{2.3}$$

2.1.1 The BLUE as a background correction

The optimal analysis $\mathbf{X}^a$ is obtained by minimizing the analysis error variance, namely the trace of $\mathbf{A}$. This leads to the formulation of the gain matrix $\mathbf{K}$, also called the Kalman matrix:

$$\mathbf{K} = \mathbf{B}\mathbf{H}^T(\mathbf{H}\mathbf{B}\mathbf{H}^T + \mathbf{R})^{-1} \tag{2.4}$$

$$= (\mathbf{H}^T\mathbf{R}^{-1}\mathbf{H} + \mathbf{B}^{-1})^{-1}\mathbf{H}^T\mathbf{R}^{-1} \tag{2.5}$$

$\mathbf{K}$ is defined in terms of the error covariance matrices $\mathbf{B}$ and $\mathbf{R}$ (if both are invertible) and of the tangent linear operator $\mathbf{H}$. Therefore the analysis is similar to the solution of the minimization approach presented in equation (1.12), and reads:

$$\mathbf{X}^a = \mathbf{X}^b + \mathbf{K}\mathbf{d}^{ob} \tag{2.6}$$

with $\mathbf{d}^{ob} = \mathbf{Y}^o - \mathbf{H}\mathbf{X}^b$ the innovation vector.
It can be deduced that a perfect confidence in the background $\mathbf{X}^b$ leads to a zero matrix $\mathbf{B}$ and therefore a zero matrix $\mathbf{K}$ by equation (2.4). In this context, the assimilation correction is zero, and $\mathbf{X}^a = \mathbf{X}^b$. In the opposite, if the confidence is total in the observations $\mathbf{Y}^o$, $\mathbf{R}$ is a zero matrix. The analysis is then the state which gives the observation vector $\mathbf{Y}^o$ by direct application of the observation operator $\mathbf{H}$. Thus, $\mathbf{X}^a$ is directly the solution of the inverse problem $\mathbf{H}\mathbf{X} = \mathbf{Y}^o$.

2.1.2 The analysis residual

The Kalman filter $\mathbf{K}$ provides a posteriori the analysis error covariance matrix $\mathbf{A}$, assuming that both background and observations errors are non-correlated. $\mathbf{A}$ reads

$$\mathbf{A} = \mathbb{E}[\epsilon^a \cdot \epsilon^{a\,T}] = (\mathbf{I} - \mathbf{KH})\mathbf{B} \tag{2.7}$$

As equation (2.7) shows, if $\mathbf{H}$ is of full rank (e.g., $\text{rank}(\mathbf{H}) = \min(n, p)$), then $\mathbf{A} \leq \mathbf{B}$, meaning that the BLUE algorithm reduces the error variance of the control variables. This order relation, defined for any matrix $\mathbf{A}$ and $\mathbf{B}$ of the positive cone of symmetric semi-definite matrices, has the following meaning:

$$\mathbf{A} \leq \mathbf{B} \quad \Leftrightarrow \quad \forall \mathbf{x} \in \mathbb{R}^n, 0 \leq \mathbf{x}^T\mathbf{A}\mathbf{x} \leq \mathbf{x}^T\mathbf{B}\mathbf{x} \tag{2.8}$$

Equivalently, as $\mathbf{A} = \mathbf{KR}$, the inverse of the analysis error covariance matrix satisfies $\mathbf{A}^{-1} \geq \mathbf{B}^{-1}$, with:

$$\mathbf{A}^{-1} = \mathbf{B}^{-1} + \mathbf{H}^T\mathbf{R}^{-1}\mathbf{H} \tag{2.9}$$

In this context, the analysis is integrated using the model M and provides a more accurate image of the system at a given time, leating to a better forecast of the system evolution than the model which does not take into account the observations.

2.2 Equivalence between the BLUE and 3DVAR

2.2.1 Least-squares method and BLUE

When considering the generalized inverse of the linear observation operator $\mathbf{H}$, which maps the state space into the observation space, observations $\mathbf{Y}^o$ are assumed to be linearly independent and the background $\mathbf{X}^b$ to exist. $\mathbf{H}$ is therefore of full rank.

For a classical least-squares problem, when there is no random error, the objective is to determine the value of the control vector $\mathbf{X}_{opt}$, which minimizes the L^2-norm of the innovation vector $\mathbf{d}^{ob} = \mathbf{Y}^o - \mathbf{H}\cdot\mathbf{X}$. In other words, $\mathbf{X}_{opt}$ minimizes the quadratic function J:

$$\min J(X) = \min\left(\frac{1}{2}\cdot\|\mathbf{Y}^o - \mathbf{H}\cdot\mathbf{X}\|^2\right) \tag{2.10}$$

$$\Rightarrow \mathbf{H}^T\cdot\mathbf{H}\cdot\mathbf{X}_{opt} = \mathbf{H}^T\cdot\mathbf{Y}^o \tag{2.11}$$

The solution $\mathbf{X}_{opt}$ satisfies the normal equation, for which different scenarii may be identified:

- $n = p$

  With $rank(\mathbf{H}) = n$, solving the normal equation is equivalent to inverting the observation operator $\mathbf{H}$ so that the minimum of the cost function J is precisely zero, and $\mathbf{X}_{opt} = \mathbf{H}^{-1}\cdot\mathbf{Y}^o$.

- $n < p$

  $rank(\mathbf{H}) = n$ leads to a regression on the observation data $\mathbf{Y}^o$. As $\mathbf{H}^T\cdot\mathbf{H}$ is a positive definite matrix, the solution $\mathbf{X}_{opt}$ is unique and satisfies $\mathbf{X}_{opt} = (\mathbf{H}^T\cdot\mathbf{H})^{-1}\cdot\mathbf{H}^T\cdot\mathbf{Y}^o$. In this context, the optimal solution is a special application of the BLUE, with $\mathbf{B}^{-1} = 0$ and $\mathbf{R} = \mathbf{I}$ by comparison with equations (2.2) and (2.4). It represents therefore the solution of the least-squares problem when there is no knowledge on the background control variable, and when the measurement errors are independent and of equal variance.

- $n > p$

  With more control variables than observations, the problem has in general an infinite set of solutions. However, it is known that there exists at least one solution as $\mathbf{H}$ is surjective (e.g., $rank(\mathbf{H}) = p$). So as to ensure unicity, the least-squares approach is generalized by introducing an a priori value of $\mathbf{X}_{opt}$, the background vector $\mathbf{X}^b$.

To ensure a well-posed problem for all possible configurations, the least-squares method is generalized by introducing the background parameter(s) $\mathbf{X}^b$ into the problem. The optimal estimator $\mathbf{X}_{opt}$ is therefore the result of the minimization of a quadratic function $J(\mathbf{X})$, composed of two terms as stated in equation (2.12): one associated with the background error, the other with the discrepancies between the observations and the image of the control vector in the observation space.

$$J(\mathbf{X}) = \frac{1}{2}\cdot \|\mathbf{X}-\mathbf{X}^b\|^2 + \frac{1}{2}\cdot \|\mathbf{Y}^o - \mathbf{H}\cdot\mathbf{X}\|^2 \tag{2.12}$$

This approach consists in penalizing the gap between the model and the observations by a back-pulling term proportional to the L^2-norm of the gap between the model and the background. This cost function $J(\mathbf{X})$ is equivalent to the variational approach if the error covariance matrices satisfy $\mathbf{B}=\mathbf{R}=\mathbf{I}$. Such a condition means that both background and observation errors are independent and follow standard normal distributions.

$\mathbf{X}_{opt}$ is the minimum of the function (2.12), so it satisfies $\nabla J(\mathbf{X}_{opt})\cdot h = 0, \forall h$, with $\nabla J(\mathbf{X})$ denoting the differential of the function $J(\mathbf{X})$. Hence,

$$\begin{aligned} \nabla J(\mathbf{X}_{opt}) &= (\mathbf{X}-\mathbf{X}^b) - \mathbf{H}^T\cdot(\mathbf{Y}^o - \mathbf{H}\cdot\mathbf{X}_{opt}) = 0 \\ \Rightarrow 0 &= (\mathbf{I}+\mathbf{H}^T\cdot\mathbf{H})\cdot\mathbf{X}_{opt} - (\mathbf{X}^b + \mathbf{H}^T\cdot\mathbf{Y}^o) \end{aligned} \tag{2.13}$$

As $(\mathbf{I}+\mathbf{H}^T\cdot\mathbf{H})$ is symmetric positive definite and therefore invertible, the solution of the cost function $J(\mathbf{X})$ is given by:

$$\begin{aligned} \mathbf{X}_{opt} &= (\mathbf{I}+\mathbf{H}^T\cdot\mathbf{H})^{-1}\cdot(\mathbf{X}^b + \mathbf{H}^T\cdot\mathbf{Y}^o) \\ &= (\mathbf{I}+\mathbf{H}^T\cdot\mathbf{H})^{-1}\cdot[(\mathbf{I}+\mathbf{H}^T\cdot\mathbf{H})\cdot\mathbf{X}^b + \mathbf{H}^T\cdot(\mathbf{Y}^o - \mathbf{H}\cdot\mathbf{X}^b)] \\ &= \mathbf{X}^b + (\mathbf{I}+\mathbf{H}^T\cdot\mathbf{H})^{-1}\cdot\mathbf{H}^T\cdot(\mathbf{Y}^o - \mathbf{H}\cdot\mathbf{X}^b) \\ \Rightarrow \mathbf{X}_{opt} &= \mathbf{X}^b + \mathbf{H}^T\cdot(\mathbf{I}+\mathbf{H}\cdot\mathbf{H}^T)^{-1}\cdot(\mathbf{Y}^o - \mathbf{H}\cdot\mathbf{X}^b) \end{aligned} \tag{2.14}$$

as $(\mathbf{I}+\mathbf{H^T}\cdot\mathbf{H})^{-1}\cdot\mathbf{H^T} = \mathbf{H^T}\cdot(\mathbf{I}+\mathbf{H}\cdot\mathbf{H^T})^{-1}$. As a consequence, the solution $\mathbf{X}_{opt}$ can be expressed as a correction of the background $\mathbf{X}^b$, similarly to the BLUE optimal estimation in equation 2.2 when supposing $\mathbf{B}=\mathbf{R}=\mathbf{I}$.

2.2.2 BLUE as a generalization of the least-squares method

The objective of data assimilation is to weigh each term of the cost function (2.12) by its precision, or equivalently by the inverse of its uncertainty (modeled as an error covariance matrix). The resulting cost function, introduced in equation (1.9), defines the 3DVAR variational approach. This measures the statistically weighted square difference between the observations and the equivalent of the control vector in the observation space on the one hand, the background and the control vector on the other hand:

$$J_{3DVAR}(\mathbf{X}) = \frac{1}{2}\Big(\mathbf{X}-\mathbf{X}^b\Big)^T\mathbf{B}^{-1}\Big(\mathbf{X}-\mathbf{X}^b\Big) + \frac{1}{2}\Big(\mathbf{Y}^o - H(\mathbf{X})\Big)^T\mathbf{R}^{-1}\Big(\mathbf{Y}^o - H(\mathbf{X})\Big) \tag{2.15}$$

with H the non-linear observation operator, whose linearization in the vicinity of $\mathbf{X}^b$ is denoted $\mathbf{H}$, so that $\mathbf{H}=\nabla H(\mathbf{X}^b)$.

As $\mathbf{X}^a = \mathrm{argmin}(J_{3DVAR})$,

$$\nabla J_{3DVAR}(\mathbf{X}^a) = \mathbf{B}^{-1}(\mathbf{X}^a-\mathbf{X}^b) + \mathbf{H}^T\mathbf{R}^{-1}(\mathbf{Y}^o - H(\mathbf{X}^a)) = 0 \tag{2.16}$$

$$\begin{aligned} \Rightarrow \mathbf{X}^a &= (\mathbf{B}^{-1}+\mathbf{H}^T\mathbf{R}^{-1}\mathbf{H})^{-1}(\mathbf{B}^{-1}\mathbf{X}^b + \mathbf{H}^T\mathbf{R}^{-1}\mathbf{Y}^o) \\ &= (\mathbf{B}^{-1}+\mathbf{H}^T\mathbf{R}^{-1}\mathbf{H})^{-1}((\mathbf{B}^{-1}+\mathbf{H}^T\mathbf{R}^{-1}\mathbf{H})\mathbf{X}^b + \mathbf{H}^T\mathbf{R}^{-1}(\mathbf{Y}^o - \mathbf{H}\mathbf{X}^b)) \\ &= \mathbf{X}^b + (\mathbf{B}^{-1}+\mathbf{H}^T\mathbf{R}^{-1}\mathbf{H})^{-1}\mathbf{H}^T\mathbf{R}^{-1}(\mathbf{Y}^o - \mathbf{H}\mathbf{X}^b) \\ &= \mathbf{X}^b + \mathbf{K}(\mathbf{Y}^o - \mathbf{H}\mathbf{X}^b) \end{aligned}$$

where the matrix $\mathbf{K}$ is the Kalman gain defined in (2.5).

The expression (2.9) shows that the inverse of the analysis error covariance matrix $\mathbf{A}$ is precisely the Hessian matrix of the generalized cost function J_{3DVAR}, evaluated at the optimal point $\mathbf{X}^a$:

$$\nabla^2 J_{3DVAR}(\mathbf{X}^a) = \mathbf{B}^{-1} + \mathbf{H}^T\mathbf{R}^{-1}\mathbf{H} = \mathbf{A}^{-1} \tag{2.17}$$

If the cost function is consistent with the probability density functions prescribed in the assimilation, then the Hessian matrix measures the sharpness of the PDF associated to $\mathbf{X}^a$: a sharper PDF means that the analysis is more reliable and that the probability of the estimated control vector to approach the true control vector is higher.

To conclude, the BLUE algorithm is equivalent to the minimization of the cost function J_{3DVAR}, both approaches leading potentially to $\mathbf{X}^a$ and its residual matrix $\mathbf{A}$. Compared to the classical least-squares method, the system is constrained by the prescribed error variances-covariances on each source of information.

2.3 Observation System Experiments, a validation framework

In the BLUE algorithm, an analysis is produced as a correction on the background, but it is necessary to ensure the good behavior of this algorithm and even its efficiency, once implemented. Observation System Experiments (OSE), schematized in figure 2.1, are a classical framework to do so as the errors in the background and in the observations as well as the true control vector are perfectly known (which is not the case in a real study). These information can therefore be used to quantify precisely the quality of the BLUE correction.

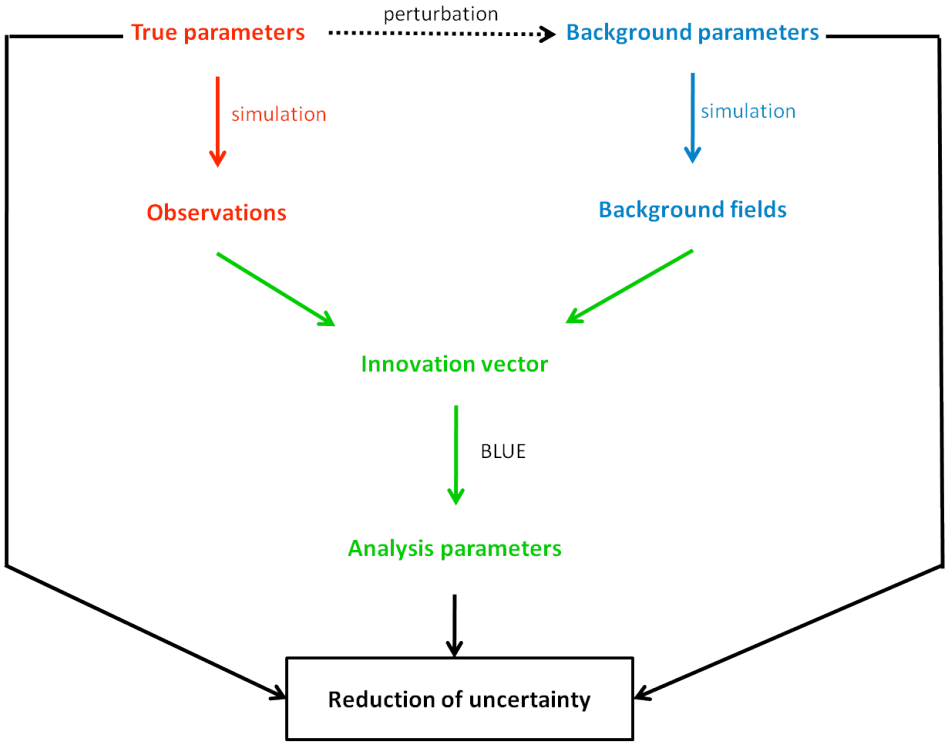

Figure 2.1: Schematic representation of OSE.

In these experiments, the true value of the control variables is assumed to be perfectly known and is used as a reference against which the quality of the correction can be evaluated. The background $\mathbf{X}^b$ is introduced as a perturbation of the true control parameters: the distance between $\mathbf{x}^t$ and $\mathbf{X}^b$ is known, and is used to define the error covariance matrix $\mathbf{B}$. As to the observations, they are produced by the model integration M using the true control parameters as parameters of the model. The selection operator is then applied to the simulated fields to extract the observations, in which noise is added. This noise is used to define the

observation error covariance matrix $\mathbf{R}$.
The perturbation, introduced either in background or in the observations, shall be consistent with the errors prescribed in the algorithm so as to define rigorous OSE. This means that any perturbation shall have a zero expectation value and a standard deviation corresponding to the prescribed error covariance matrix. So the background and the observation errors, along with their statistics, are completely known for these experiments, also called twin experiments, as two sets of control parameters are introduced, the true and background parameters.

The data assimilation algorithm provides an analysis. In this context and for the control of a single parameter, the analysis value shall be between the true and the background values of the control vector (provided H is linear, which is often not the case), at a distance of the background value depending on the errors prescribed in the observations and in the background.

Measuring the difference between the true state $\mathbf{x}^t$ and the analysis $\mathbf{X}^a$ provides information on the quality of the correction. The OSE are therefore a valuable tool to validate data assimilation and to prove the feasibility of the methodology for wildfire applications.

3. Parameter Calibration for a 1D Sample Model

In this part, a sample model is used to show the principles of data assimilation and to underline the critical points of the Best Linear Unbiased Estimator (BLUE) process in the context of Observation System Experiments (OSE), such as the effect of the non-linearities on the correction of the background. This model represents the 1D diffusion of a Dirac delta function, and the objective is to assimilate a single model parameter, the diffusion coefficient.

3.1 Model configuration

3.1.1 Diffusion equation

The 1D diffusion equation of a scalar quantity $u(x,t)$ is defined by the following PDE:

$$\frac{\partial u}{\partial t} = D\,\frac{\partial^2 u}{\partial x^2} \tag{3.1}$$

with D the diffusion coefficient. Considering a Dirac delta function as initial condition so that $u(x,t) = n_0\,\delta(x)$, the PDE has an analytical solution given by:

$$u(x,t) = \frac{n_0}{\sqrt{4\pi D t}}\exp\left(\frac{-x^2}{4Dt}\right) \tag{3.2}$$

3.1.2 Assimilation quantities

The goal of this sample model is to implement the calibration of the diffusion parameter D present in equation (3.1). So the control vector $\mathbf{X}$ is reduced to a scalar ($n = 1$), with D as the single component.

In the context of OSE, the true value of D is supposed to be known and is denoted by D_t. The vector gathering all the values of the analytical solution in space and time defines the true trajectory, which depends upon the reference diffusion coefficient D_t. Figure 3.1 presents the trajectory associated to $D_t = 0.1$.

The background parameter D_b is specified as a perturbation of D_t. In this prototype, observations are measurements of the true values of $u^t(x,t)$ at fixed spatial locations over the computational domain and at given times. So they can be directly extracted from the true representation so as to correct D_b via the analysis increment $\delta\mathbf{X}^a = \mathbf{K}(\mathbf{Y}^o - \mathbf{H}\mathbf{X}^b)$. The resulting analysis coefficient D_a represents a diffusion phenomenon closer to the physics described by D_t than D_b.

It is important to notice that the analysis coefficient D_a shall be in the interval $[D_b; D_t]$: if the confidence in the background is high, the correction will be low and D_a will be close to D_b, whereas D_a will be close to D_t if the observations are granted a high confidence. This result can only be guaranteed if the linear tangent of the observation operator $\mathbf{H}$ is valid along the interval $[D_b; D_t]$. It might not be the case if the distance between D_b and D_t is too large as H is non-linear. A sensitivity study has to be performed to define how large this interval can be without introducing too significant non-linearities in the data assimilation algorithm.

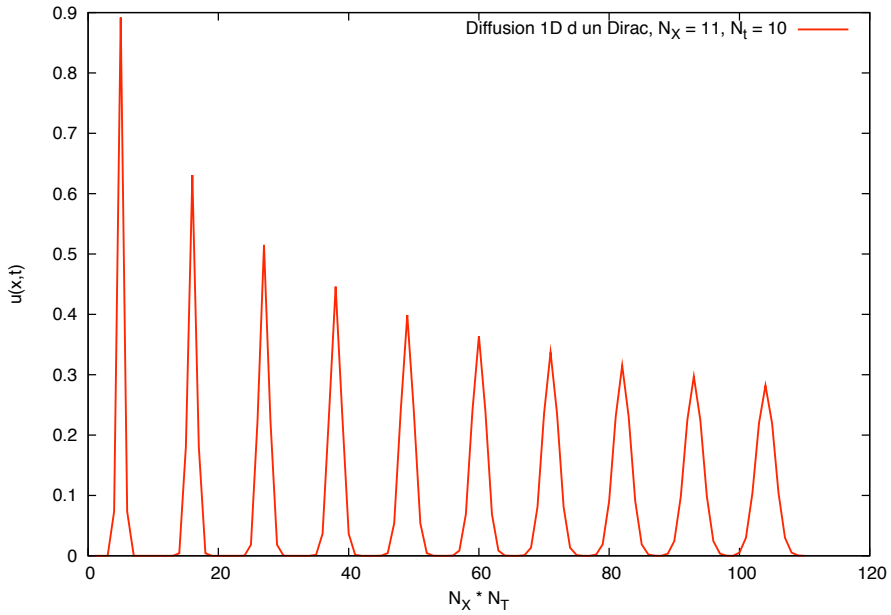

Figure 3.1: Representation of the 1D diffusion of the quantity $u^t(x,t)$ over time, initialized as a Dirac impulsion. The x-axis is meshed into $N_x = 11$ space elements (the Dirac impulsion is located in the middle of the space interval) and the solution is computed over $N_t = 10$ time steps. Consequently, the true trajectory is defined by $N_x \times N_t = 110$ components.

3.2 Steps of the data assimilation process

3.2.1 Choice of the numerical configuration

For this simple prototype, the computational configuration is chosen so as to keep a low computational cost and an immediate visualization. For this purpose, the size of the matrices and vectors involved in the assimilation process shall keep a relatively small size. So all the data assimilation tests are carried out for a mesh of $N_x = 11$ elements and an assimilation window defined by $N_t = 10$ time steps of 1 second.

3.2.2 Integration of the true and background trajectories

The true trajectory results from the integration of the model using D_t as the model parameter. From this true trajectory are directly extracted the artificial observations with a fixed frequency in space and time, for instance each two time steps and each two grid points. No noise is introduced. All the resulting observations are gathered into the vector $\mathbf{Y}^o$ of dimension p. For the present numerical configuration, there are 6 observations per time step and 5 time steps observed, so $p = 30$.

The background vector $\mathbf{X}^b$ has for single component the scalar D_b, which is different from D_t and which is associated to the background trajectory $u^b(x,t)$. In figure 3.2, $u^b(x,t)$ is represented for $D_b = 0.02$. The diffusion is therefore less intense for the background than for the true parameter ($D_t = 0.1$), that is why the magnitude of the background trajectory is higher than the magnitude of the true trajectory at each time step.

$\mathbf{X}^b$ and $\mathbf{Y}^o$ do not evolve in the same space, so an observation operator H is required to map the control parameters onto the observation space. In this context, H gives the value of the background trajectory at

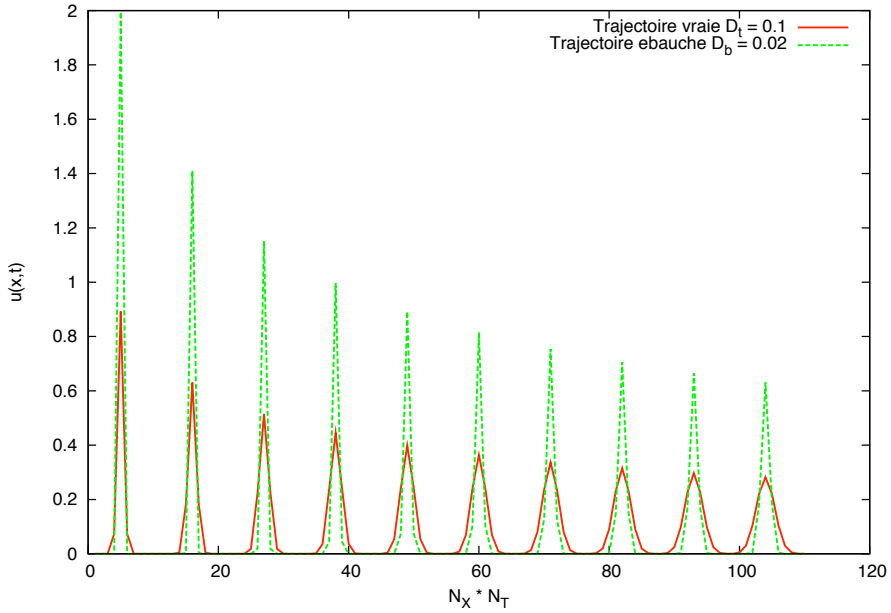

Figure 3.2: Representation of the true and background trajectories $u^t(x,t)$ and $u^b(x,t)$, initialized as a Dirac impulsion. The x-axis is meshed into $N_x = 11$ space elements (the Dirac impulsion is located in the middle of the space interval) and the solution is computed over $N_t = 10$ time steps.

each observation point. Thus, H is a composition of a model integration M and of a selection matrix S. Only the second step is linear as the solution describing the diffusion process depends non-linearly on the diffusion coefficient D in equation 3.2. H is therefore non-linear.

3.2.3 Determination of the tangent linear of H

In chapter 2, the BLUE analysis was formulated assuming a linear observation operator H. However, in the present application, it is not the case. So the assimilation algorithm requires a linearization $\mathbf{H}$ of the observation operator so as to define the optimal Kalman gain $\mathbf{K}$. $\mathbf{H}$ results from the Taylor expansion of H in the vicinity of a reference diffusion parameter, denoted $\mathbf{X}^g$:

$$H(\mathbf{X}^g + \delta\mathbf{X}^g) = H(\mathbf{X}^g) + \frac{\partial H}{\partial \mathbf{X}^g}\delta\mathbf{X}^g + O((\partial\mathbf{X}^g)^2) \tag{3.3}$$

with $\lim_{\delta\mathbf{X}^g \to 0} O((\partial\mathbf{X}^g)^2)\,(\delta\mathbf{X}^g)^{-2} = 0$.

By definition, the tangent linear of H at reference parameter $\mathbf{X}^g$, also called the linearized observation operator $\mathbf{H}$, is the Jacobian matrix in the Taylor expansion (3.3) and is approximated using a non-centered finite-difference scheme. Hence,

$$\mathbf{H} = \frac{\partial H}{\partial \mathbf{X}^g} \approx \frac{H(\mathbf{X}^g + \delta\mathbf{X}^g) - H(\mathbf{X}^g)}{\delta\mathbf{X}^g} \tag{3.4}$$

In practice, $\mathbf{H}$ results from the Taylor expansion in the vicinity of the background $\mathbf{X}^b$. The computation of $\mathbf{H}$ requires the integration of an additional trajectory corresponding to a perturbation of $\mathbf{X}^b$, denoted by $\mathbf{X}^b + \delta\mathbf{X}^b$. Then, both trajectories are projected onto the observation space through the selection operator S. The tangent linear $\mathbf{H}$ can be therefore computed for a prescribed perturbation $\delta\mathbf{X}^b$ using equation (3.4).

As H is non-linear, the quality of the linear approximation is highly sensitive to the perturbation $\delta\mathbf{X}^b$ introduced to compute $\mathbf{H}$. By construction, equation (3.4) is valid when the analysis is in the interval $[\mathbf{X}^b; \mathbf{X}^b + \delta\mathbf{X}^b]$, but its validity is not ensured outside of this interval. Consequently, the sensitivity of $\mathbf{H}$ shall be carefully studied as a function of the control parameter so as to guarantee the optimality of the solution when $|\mathbf{X}^a - \mathbf{X}^b| > \delta\mathbf{X}^b$.

3.2.4 Modeling of the error covariance matrices

For one parameter calibration, $\mathbf{B}$ is a scalar, namely the error variance associated to the diffusion coefficient. This variance can be derived from the knowledge of the physics of the system. In practice, the standard deviation σ_b of the background error is specified as a percentage α_b of the true parameter:

$$\sigma_b = \alpha_b \times D_t \tag{3.5}$$

As to the observation error covariance matrix $\mathbf{R}$, its size is $p \times p$ with p the dimension of the observation vector $\mathbf{Y}^o$. In this study, it is assumed that observation errors are not correlated so that $\mathbf{R}$ is reduced to a diagonal matrix (which is a common assumption in data assimilation). Their standard deviation is calculated as a percentage α_o of the mean value of the observed field $\overline{\mathbf{Y}^o}$:

$$\sigma_o = \alpha_o \times \overline{\mathbf{Y}^o} \tag{3.6}$$

implying that all observations have been prescribed the same error.

With these two definitions (3.5) and (3.6), the magnitude of α_b and α_o characterizes the level of confidence given to each source of information.

3.2.5 Analysis, application of the BLUE algorithm

To apply the BLUE algorithm, it is necessary to formulate the following mathematical elements: the background control vector $\mathbf{X}^b$, the observation vector $\mathbf{Y}^o$, the equivalent of the background in the observation space $H(\mathbf{X}^b)$, the linear tangent $\mathbf{H}$ of the observation operator, the error covariance matrices $\mathbf{B}$ and $\mathbf{R}$. As a result, the assimilation algorithm produces an analysis D_a of the control parameter, which is the optimal unbiaised linear estimator of the true coefficient D_t. The analysis trajectory can then be simulated using D_a as the parameter of the model.

A classical diagnosis in data assimilation consists in verifying that the Root Mean Square (RMS) of the distance between the background trajectory and the observations is reduced by the analysis. The following condition shall therefore be satisfied:

$$\mathbf{d}^{oa} = \mathrm{RMS}(\mathbf{Y}^o - H(\mathbf{X}^a)) < \mathbf{d}^{ob} = \mathrm{RMS}(\mathbf{Y}^o - H(\mathbf{X}^b)) \tag{3.7}$$

3.3 Validation of the data assimilation prototype

In the following, results from a series of data assimilation tests are presented, providing a first insight of how sensitive such an algorithm is to the perturbation introduced in the observations and in the model. Its performance will be analysed in terms of AMO/BMO and validated.

3.3.1 Simple assimilation

The assimilation prototype is not a strict application of the OSE. The distance between the true coefficient D_t and the background coefficient D_b is arbitrary, and not consistent with the prescribed background error variance σ_b^2. Observations are assumed to be perfect even though a non-zero error variance σ_o^2 is prescribed to the observations. This assimilation context is deliberate as the goal of this preliminary study is to focus

on the correction algorithm. Additionally, it is not so far from a real context as in reality observations and background have intrinsic errors which are hard to evaluate.

Results

A first series of tests is carried out for $D_t = 0.1$ and $D_b = 0.02$. The uncertainty in the observations is fixed ($\alpha_o = 0.05$, leading to $\sigma_o^2 = 2.42 \times 10^{-5}$) and the analysis is studied as a function of the background variance σ_b^2. Results are presented in table 3.1 for different values of α_b and thus, for different background uncertainties σ_b^2.

α_b	σ_b^2	D_a	RMS(BMO)	RMS(AMO)
0.05	1.00×10^{-6}	0.0428	0.271	0.118
0.005	1.00×10^{-8}	0.0344	0.271	0.156
0.0005	1.00×10^{-10}	0.0204	0.271	0.267

Table 3.1: Evolution of the analysis as a function of the background variance σ_b^2.

- When α_b is fixed to 0.05 (leading to a background variance of $\sigma_b^2 = 1 \times 10^{-6}$), the analysis is $D_a = 0.0428$, a value which is in the interval $[D_b; D_t]$ as expected from the linear estimation theory. Furthermore, the distance between the model and the observations is reduced by 66% as RMS(BMO) = 0.271 < RMS(AMO) = 0.118. The data assimilation algorithm provides therefore a trajectory which is closer to the observations than the background trajectory as confirmed by figure 3.3.

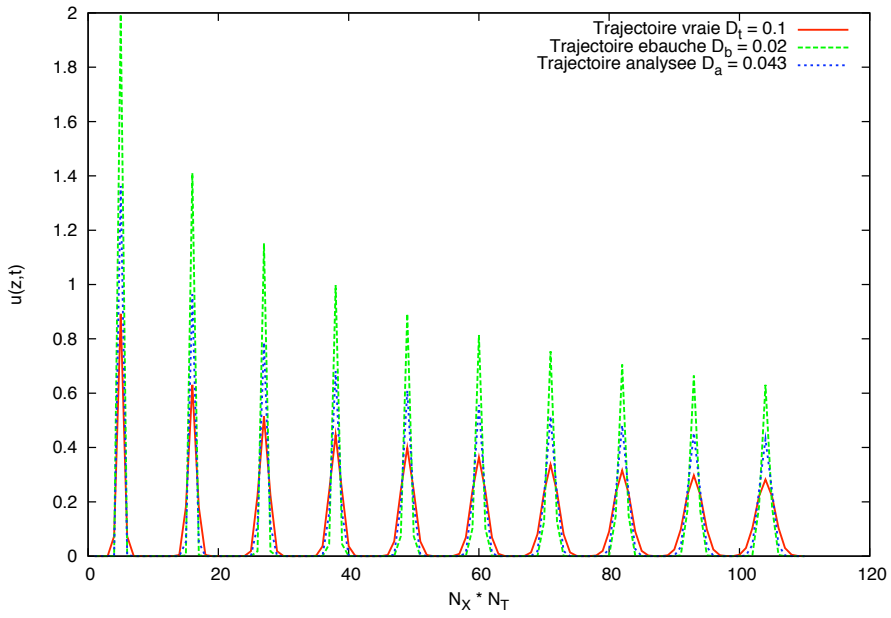

Figure 3.3: True, background and analysis trajectories associated to $D_t = 0.1$, $D_b = 0.02$ and $D_a = 0.0428$, resulting from the following uncertainty configuration: $\sigma_b^2 = 1 \times 10^{-6}$ and $\sigma_o^2 = 2.42 \times 10^{-5}$. The x-axis is meshed into $N_x = 11$ space elements (the Dirac impulsion is located in the middle of the space interval) and the solution is computed over $N_t = 10$ time steps.

- A validation of the assimilation prototype consists in prescribing a higher confidence in the background and in ensuring that the analysis converges towards the background parameter when non-linearities of H cannot interfere. When $\alpha_b = 0.005$, the level of confidence in the background is increased and so

the analysis is even closer to $D_b = 0.02$, with $D_a = 0.0344$. The RMS of the distance between the model and the observations is only reduced by 42%. This is consistent with the configuration as the observations have less weight in the optimization problem than for $\alpha_b = 0.05$. This trend is confirmed by the third experiment carried out with $\alpha_b = 0.0005$: the confidence in the background is predominant and thus, no correction of the background is applied as $D_a = 0.0204$.

- Inversely, the assimilation algorithm is expected to converge towards $D_t = 0.1$ if the confidence in the observations is higher and higher. Results show, however, that it is not the case. For instance, if $\sigma_o^2 = 2.42 \times 10^{-19}$ and $\sigma_b^2 = 1 \times 10^{-14}$, $D_a = 0.0429$. This means that the analysis trajectory stays at equal distance from the background and from the observations even though the observation error is negligible compared to the background error. This result may be linked to the validity of the linear tangent $\mathbf{H}$ as the interval $[D_b; D_t]$ may be too large to guarantee an optimal solution. Once D_a is too far away from D_b, or equivalently once $\sigma_o^2 << \sigma_b^2$, non-linearities may interfere in the data assimilation algorithm and degradate the analysis.

To check the good behavior of the algorithm when the level of confidence in the observations is high, another assimilation configuration is tested with $D_b = 0.095$ and $D_t = 0.1$. The size of the interval $[D_b; D_t]$ is voluntarily restricted. Results, presented in table 3.2, shows that when the confidence in the observations is predominant, the analysis is equal to the observation with $D_a = 0.0999$. In this case, the RMS of the distance between the model and the observations is reduced by 99.8%, confirming that the non-linearities have a much lower impact on the solution when the size of the interval $[D_b; D_t]$ is of the same magnitude as the perturbation δD. The basic diagnostic is also satisfied as D_a is close to D_b when a strong error is prescribed to the observations.

α_o	α_b	σ_o^2	σ_b^2	D_a	RMS(BMO)	RMS(AMO)
0.05	0.05	2.42×10^{-5}	2.25×10^{-5}	0.09987	5.94×10^{-3}	1.51×10^{-4}
0.05	1	2.42×10^{-5}	9.02×10^{3}	0.09999	5.94×10^{-3}	1.086×10^{-5}
1	0.05	9.68×10^{-3}	2.26×10^{-5}	0.09544	5.94×10^{-3}	5.39×10^{-3}

Table 3.2: Analysis for a restricted interval $[D_b; D_t] = [0.095; 0.1]$.

Conclusion

This simple assimilation algorithm proves the feasibility of the diffusion parameter calibration with an algorithm of type BLUE. Its good behavior has been validated by changing the error variance associated to the background and the observations: the analysis is located between the background and the observations as an intermediate state, but moves closer to one or another depending on the errors.

However, observations are assumed to be perfect, while a measurement error is prescribed. So a complete validation of this assimilation prototype requires to prescribe background and observation errors that are consistent with the perturbations introduced in the parameters. Furthermore, this preliminary study shows that a particular attention is required when using the tangent linear of the observation operator. One solution would be to consider analysis as an iterative process with the setting up of external loops so as to take into account, at least partially, the non-linearities of the model.

3.3.2 Rigorous twin experiments

The error variances are prescribed according to the distances between the background and the true states on the one hand, between the observations and the true state on the other hand. So D_b is prescribed as a perturbation of D_t such that $D_b = D_t + \sigma_b$, with $\sigma_b = \alpha_b \times D_t$ the background error standard deviation ($\mathbf{B} = \sigma_b^2$). As to the observation error, its standard deviation is given by $\sigma_o = \alpha_o \times \overline{\mathbf{Y}^o}$. The noise vector added to the observations is generated via a vector of random numbers, whose probability function is a centered Gaussian distribution of variance σ_o^2.

In this context of rigorous twin experiments, a complementary diagnostics of the analysis optimality is the reduction of the distance between the background trajectory and the true trajectory in average. The

following condition shall therefore be satisfied:

$$\text{RMS(TMA)} < \text{RMS(TMB)} \tag{3.8}$$

with RMS(TMB) $= \mathbf{x}^t - \mathbf{X}^b$ and RMS(TMA) $= \mathbf{x}^t - \mathbf{X}^a$.

Results

Different experiments are carried out for $D_t = 0.1$ with the background and observation variances as parameters. This means that the background control parameter varies when a different value of α_b is imposed. Results are presented in table 3.3, and show the consistency of the methodology as RMS(OMA) < RMS(OMB) for all tested configurations.

series	α_o	α_b	σ_o	σ_b	D_b	D_a	RMS(BMO)	RMS(AMO)
1	5%	5%	4.92×10^{-3}	5×10^{-3}	0.105	0.10017	6.81×10^{-3}	4.52×10^{-3}
	10%	10%	9.8×10^{-3}	1×10^{-2}	0.11	0.10005	1.33×10^{-2}	9.06×10^{-3}
	50%	50%	4.92×10^{-2}	5×10^{-2}	0.15	0.091	5.93×10^{-2}	4.75×10^{-2}
2	5%	0.1%	4.92×10^{-3}	1×10^{-4}	0.1001	0.1001	4.528×10^{-3}	4.527×10^{-3}
	0.1%	5%	9.8×10^{-5}	5×10^{-3}	0.105	0.096	5.51×10^{-3}	4.32×10^{-4}
3	0.1%	0.1%	9.8×10^{-5}	1×10^{-4}	0.1001	0.1	1.39×10^{-4}	9.03×10^{-5}
	5%	5%	4.92×10^{-3}	5×10^{-3}	0.095	0.1002	7.82×10^{-3}	4.519×10^{-3}
	50%	50%	4.92×10^{-2}	5×10^{-2}	0.05	0.082	0.108	5.27×10^{-2}

Table 3.3: Data assimilation results for rigorous twin experiments.

- SERIES 1: It can be deduced that for reasonable errors, of same magnitude between observations and background, the analysis is close to D_t. Furthermore, the analysis trajectory is closer to the true trajectory than the background trajectory. For instance, for $\alpha_o = 5\%$ and $\alpha_b = 5\%$, RMS(TMB) $= 4.09 \times 10^{-3}$, while RMS(TMA) $= 1.48 \times 10^{-4}$. Projected onto the control space, this means that D_a is closer to D_t than to D_b, as $D_b - D_t > D_a - D_t$.
- SERIES 2: In this second series of experiments, the background and observation errors do not have the same magnitude. The analysis is equal to the background when the confidence in the background is predominant. However, the analysis is not close to the true coefficient when the confidence in the background is damaged: $D_a = 0.096$, while $D_t = 0.1$ and $D_b = 0.105$. So as to explain this behavior of the algorithm, the background coefficient is modified such that $D_b = D_t - \sigma_b$, instead of $D_b = D_t + \sigma_b$. The perturbed diffusion coefficient used to determine $\mathbf{H}$ is then $D_p = 0.09975$, instead of $D_p = 0.11025$. Using the same configuration with a strong confidence in the observations, the analysis is close to the true state with $D_a = 0.0999$. This result is due to the sensibility of $\mathbf{H}$ with respect to the diffusion coefficient: only in the second case, D_p is in the interval $[D_b; D_t]$.
- SERIES 3: The third series of data assimilation tests confirms the non-validity of the tangent linear if the background is too far away from the true diffusion coefficient. Indeed, when $\alpha_o = 1\%$ and $\alpha_b = 1\%$, the analysis is equal to the true coefficient. When the background error grows, independently from the ratio between observation and background errors, this is no longer the case: the analysis will at some points exceed the true coefficient and be outside of the interval $[D_b; D_t]$. These results prove that rigorous OSE are not sufficient to handle the non-linearities of the problem. Another approach needs to be enquired.

3.3.3 Analysis as an iterative process

One solution to curb the impact of the non-linearities could be to implement the assimilation as an iterative process. In this configuration, the analysis results from a succession of corrections on the background, and for each correction $\mathbf{H}$ is updated at a new reference diffusion coefficient (e.g., the analysis of the previous iteration). The process is fully described in the following algorithm.

In this work, one strategy is experimented: the tangent linear is the only updated quantity as the background $\mathbf{X}^b$ stays unchanged. $\mathbf{B}$ can be updated or not. If so, it is replaced by the analysis error covariance matrix $\mathbf{A}$ of the previous iteration. Note that in this iterative process, the observations are supposed to be perfectly known as in the simple assimilation.

Algorithm

1. Determination of the true trajectory.
2. Construction of the observations, directly extracted from the true state.
3. Determination of the background trajectory.
4. Start of external loops:
   (a) Determination of the reference diffusion coefficient $\mathbf{X}^g$:
   - iteration 1, $\mathbf{X}^g = \mathbf{X}^b$.
   - all other iterations, $\mathbf{X}^g = \mathbf{X}^a$.
   (b) Determination of the reference trajectory.
   (c) Construction of the tangent linear of the observation operator in the vicinity of the reference control parameter $\mathbf{X}_g$.
   (d) Modeling of the background error covariance matrice $\mathbf{B}$:
   If variable,
   -iteration 1, $\mathbf{B} = \sigma_b^2$.
   -all other iterations, $\mathbf{B} = \mathbf{A}$.
   (e) Modeling of the observation error covariance matrix $\mathbf{R}$.
   (f) BLUE application.
   (g) Integration of the analysed trajectory.
5. End of external loops.

Results

As previously, $D_t = 0.1$. Observations are built using $\alpha_o = 0.05$ (equivalently, $\sigma_o^2 = 2.42 \times 10^{-5}$). The background coefficients, α_b and D_b, are used as parameters as indicated in table 3.4, where results are presented for a 4-iteration-loop.

- SERIES 1 ($\mathbf{B}$ fixed): The update of the tangent linear, without modification of $\mathbf{B}$ neither of D_b, changes the analysis at each iteration. This is a proof of the existence of non-linearities in the problem, in particular with $D_b = 0.02$ as the assimilation interval $[D_b; D_t]$ is larger.
  Furthermore, this gives an insight of the sensitivity of these non-linearities to the diffusion coefficient. This approach shall indeed provide a more valid linear approximation in the vicinity of the observations, and thus a more correct analysis. However, the analysis exceeds significantly D_t for $\alpha_b = 5\%$: $D_a = 0.128$ with $\mathbf{B} = 0.06$, and $D_a = 0.15$ with $\mathbf{B} = 0.02$. This confirms that the effect is amplified when the interval $[D_b; D_t]$ is larger and when the observation variance is lower.
- SERIES 2 ($\mathbf{B}$ variable): Along the iterations, the confidence in the background increases. D_a converges indeed towards D_b as $\mathbf{A} < \mathbf{B}$ at each iteration and $\mathbf{B}$ is updated with $\mathbf{A}$ at the next iteration. Unlike in the first series of experiments, the analysis is now in the interval $[D_b; D_t]$ for $\alpha_b = 5\%$ and for both values of D_b, which is more consistent with the method.

This approach has a serious drawback: at each iteration, the algorithm gives a higher weight to the background at the expenses of the observations, independently of their intrinsic errors, while its objective is to use the information extracted from the observations to adjust the model variables.

Case	D_b	α_b	D_a^1	D_a^2	D_a^3	D_a^4
B fixed	0.02	2%	4.22×10^{-2}	7.24×10^{-2}	7.81×10^{-2}	7.61×10^{-2}
	0.02	5%	4.28×10^{-2}	8.78×10^{-2}	0.15	0.15
	0.06	2%	8.56×10^{-2}	9.67×10^{-2}	9.99×10^{-2}	0.10
	0.06	5%	8.78×10^{-2}	0.10	0.11	0.128
B variable	0.02	5%	4.28×10^{-2}	2.67×10^{-2}	2.97×10^{-2}	2.69×10^{-2}
	0.06	5%	8.78×10^{-2}	7.12×10^{-2}	7.20×10^{-2}	6.86×10^{-2}

Table 3.4: Data assimilation results for external loops.

An alternative would be to update the background $\mathbf{X}^b$ at each iteration with the analysis of the previous iteration, so as to satisfy the consistency between the background and its uncertainty. This leads to a solution which simulates a state closer to the observations, as the background moves closer to the observations at each iteration. This is a possible strategy if the domain of application implies a much higher confidence in the observations. Note that in this case the computation of the innovation vector is different: instead of $\mathbf{d}^{ob} = \mathbf{Y}^o - H(\mathbf{X}^b)$, it shall be defined as: $\mathrm{d}^{ob} = \mathbf{Y}^o - \mathbf{H}\Big(\mathbf{X}^b - \mathbf{X}^g\Big)$ with $\mathbf{H}$ calculated in the vicinity of the reference control parameter $\mathbf{X}^g$.

Conclusion

From this sample study, it appears that data assimilation does not only consist into a comparison of the model outputs and the experimental measures, nor into an automatic approach where the objective is to control the input so as to obtain the expected outputs in real-time. In the contrary, this method compares statistically an a priori knowledge of the model with experimental measures, directly in the course of the simulation, so as to approach as best as possible the true state of the system. In meteorology, the uncertainty in the system is mostly due to the initial condition, but in general it arises from physical properties as well as from boundary conditions.

So data assimilation is equivalent to an optimization problem with the objective of extracting the best of the model and of the observations. More precisely, information extracted from observations accumulate into the model and propagate to all variables by taking advantage of the constraints prescribed by the laws of time evolution and the physical properties. This leads therefore to a more realistic description of the system than if either source of information were considered separately.

As none of the data are perfectly known, the optimal solution is proportional to the discrepancies between the background in the observation space and the observations, the so-called innovation vector OMB. The analysis increment is therefore significant when the level of confidence in the background is low, or equivalently when the level of confidence in the observations is high. This leads to the definition of the analysis, which shall satisfy the condition OMA $<$ OMB for optimality. In this sample study, this condition was not always satisfied as non-linearities, notably in the observation operator, can interfere with the BLUE algorithm. In this case, some more advanced algorithms need to be developed such as the external loops.

Applications of data assimilation arise in many fields of geosciences, from hydrology to atmospheric chemistry, and more generally in all topics related to control theory. Its extension to wildfire propagation is the long-term objective of this project.

Part II

Wildfire Propagation Model for Anisotropic Vegetation Distribution

Introduction

Understanding and identifying the mechanisms that are involved in the propagation of a wildfire is an essential step to improve the prediction of the direction and of the speed of the fire front. The propagation of a wildfire results indeed from a multi-scale interaction between multiple factors, for instance the local vegetation characteristics, topography and wind conditions. The wildfire models range from the purely physical (based on fundamental understanding of the physics and chemistry involved in the behavior of the fire) through the purely empirical (based on the phenomenological description of the fire propagation) [19][20][21]. In-between different approaches using mathematical/statistical tools exist thanks to the development of the field of spatial data analysis (geographic information systems, remote sensing). However, none of them account accurately for all the relevant physical processes: the model parameters are only partially known and the multi-scale and multi-physics phenomena are not fully described.

A wildfire can be considered as the multi-scale combination of two processes: 1. exothermic chemical reactions occuring at the flame scale (e.g., at the molecular scale) between oxygen and the hot gases resulting from the pyrolysis of the vegetation; 2. transport of the energy released (in the form of heat) to the surrounding unburnt environment leading to the fuel ignition and thus to a flame propagation at a larger scale (from millimetres up to kilometres). This is the interaction of these processes over the wide range of temporal and spatial scales that makes the modeling of wildfire behavior a scientific challenge.

This work focuses on the data assimilation method itself, and not directly on the physics of a wildfire. The physical processes governing a fire propagation are therefore described at a macroscopic scale, which also corresponds to the scale at which the observations are available and which is therefore consistent with the data assimilation methodology. At this scale, the wildfire can be considered as an interface between two zones, where the hot gases have burned on one side and where the vegetation is still fresh on the other side. In this study, the wildfire has therefore a front-like topology.

This part of the thesis defines the model which simulates the evolution of a wildfire in a two-dimensional surface layer just above the ground. This model based upon the reaction-diffusion equation integrates the main features of a fire: a kinetic term is coupled to diffusion so as to create a propagating front in a domain where the vegetation may be randomly spread. A new formulation is adopted in order to define the local flame speed (i.e., the local rate of spread) as the main physical quantity in the model. This local flame speed depends on a single variable that represents the effects of a non-uniform vegetal fuel distribution.

4. Physics and Chemistry of a Wildfire

4.1 Combustion of vegetation

4.1.1 Definition of a fire

A fire requires an external source of heat to be started, but once the ignition stage is reached it can self-sustain thanks to a series of chemical reactions between oxygen (at least, an oxygen-rich compound) and some combustible materials (provided there is a continuous supply of reagents). This so-called oxidation reaction is represented as

$$\text{Fuel(F)} + \text{Oxygen}(O_2) \quad \Rightarrow \quad \text{Products(P)} + \text{Heat} \tag{4.1}$$

where the fuel consists mostly of carbon (C), hydrogen (H) and oxygen (O) atoms, forming a molecular structure of the form $C_x H_y O_z$.

In this process of combustion, a large amount of heat is released and then transferred to the surrounding unburnt fuel, leading to the propagation of a flame over a large scale. This flame is the visible part of a fire and indicates the position of the fire front, that is to say the zone where the chemical reactions occur continuously and where the unburnt combustible meets active flames. Note that non-flaming combustion might occur when the fuel is in solid phase or at low temperature. The process is then called smoldering.

4.1.2 Diffusion flame versus premixed flame

In general, a fire can be classified into two different categories, either a premixed flame or a diffusion flame. In the former fuel and oxidizer are mixed before the fire ignition (which is due to a significant increase of temperature), while the latter corresponds to the scenario where fuel and oxidizer are initially separated and where the combustion process is confined at the interface between both components. In this case of diffusion flame, both fuel and oxidizer combine by diffusion before burning. So the fuel-oxidizer ratio varies throughout the flame, and the flame rate of spread is limited by the rate of diffusion.

In this study, the propagation of a wildfire is studied at a scale and is therefore identified as a front, separating the zone where the fuel has burnt from the zone where the vegetation is still fresh. At this scale, this description of a wildfire corresponds to a premixed flame.

In the vicinity of the fire front, two regions can be identified as illustrated by figure 4.1. The combustion region defines the zone where the chemical reactions take place and where a large amount of heat is released. Ahead of the combustion zone, in the direction of the fresh fuel, there is the pre-heated region. This represents the zone which receives a significant part of the heat transferred from the flame (mainly by radiation), leading to an increase of the temperature of the unburnt mixture up to its ignition temperature T_{ig}. This characteristic temperature indicates the boundaries between the combustion zone and the pre-heated region.

Experimental data show that the wider the preheat region, the faster vegetation reaches the ignition temperature and so the faster the fire spreads. This is what happens when a fire spreads uphill with a favorable wind: the flame is tilt towards the unburnt region and heat is transferred (via radiation) to a larger vegetation area ahead of the fire front, leading the vegetation to its ignition temperature in a shorter amount of time.

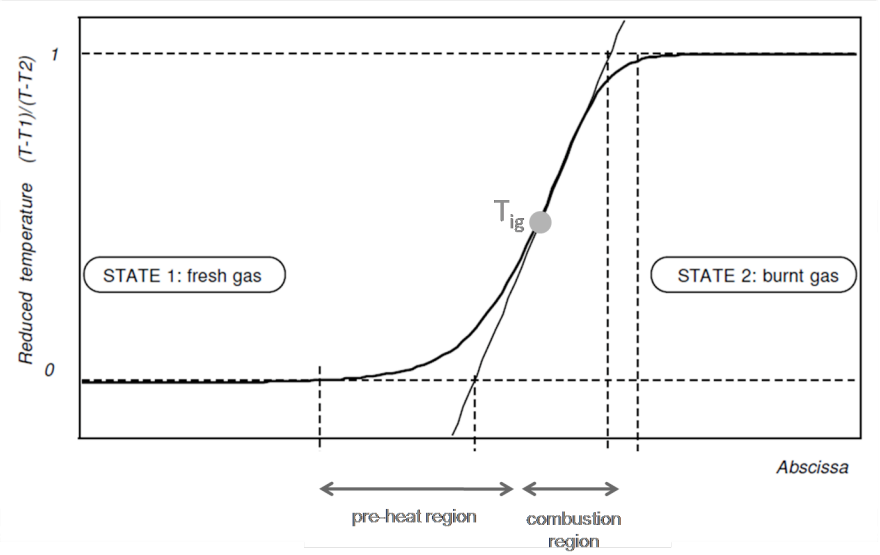

Figure 4.1: Two states in the vicinity of the fire front: fresh gas/burnt gas.

4.1.3 Combustion of a wildfire

In industrial applications, combustion systems are carefully controlled so that they involve a relatively limited set of fuels, and the mass fraction of all these compounds are precisely controlled. However, this does not applied for a wildfire. Wild biomass fuel is made of twigs, bark, wood, grasses, shrubs, savannas, forests, etc., in different states depending on their age and level of biological decomposition. It covers therefore a wide range of physical structures and chemical components. What is more, all these materials can absorb water from the atmosphere, a process which changes drastically their physical and chemical properties. So the vegetation compostion is complex and mostly unknown due to the nature of the fuel and the range of conditions encountered.

However, vegetation and wood are made of organic matter with carbon, oxygen, hydrogen and nitrogen elements. These elements combine to form biopolymers, such as cellulose of the form $(C_6H_{10}O_5)_n$ and which is the main component of a wild biomass fuel (40% to 50% of the wood composition).

Cellulose has a very complex path to a gaseous fuel and ignition. Before burning, the organic materials shall indeed undergo a series of transformations:

1. a phase transition from solid to gas, called pyrolysis.
   Due to the heat transferred from the flame (through convection and radiation), the vegetation ahead of the front undergoes a thermal decomposition. First, wood is dried as water is vaporized and some Volatile Organic Compounds (VOCs) might be emitted. Then, the pyrolysis temperature is reached and flammable gases are released. Due to the volatilisation, wood is said to be only partially gasified. The time required for the pyrolysis to proceed depends on the thermal properties of the materials about to burn and in particular to their thermal inertia.

2. the fuel gas transport from the ground layer to the surface of the fluid boundary layer.
   Combustion can only proceed if the flammable gases are in contact with an oxidizer, typically the ambient air for a wildfire. So these gases need to be transported through the vegetation layer by diffusion and convection.

3. the onset of the chemical reaction.
   Once the flammable gases are in contact with the atmosphere, if their temperature has reached the ignition temperature T_{ig}, then the chemical reactions can start and a flame can develop in a layer above the ground. A part of the energy produced by the flame is then transferred to the vegetation ahead of the fire and so the gasification keeps going. However, this onset of combustion is highly dependent on the weather conditions. For instance, wet wood is difficult to ignite and it may be even impossible

above a characteristic threshold of moisture content, called the moisture of extinction.
Ignition and combustion of biomass fuel is mainly based on the pyrolysis of cellulose and on the reactions between the pyrolysis products and the atmospheric gases such as oxygen. As the reactions proceed, fuel and oxidizer are consumed, but due to the constant interaction with the atmosphere and the (unbounded) amount of fuel available, a fire may not stop.

4.2 Heat and mass transfers

Combustion is characterized by simultaneous heat and mass transfers. Assuming that the gas flow can be considered as a continuous medium, convection and radiation are the two key processes governing a wildfire propagation.

Convection is linked to the bulk motion of a fluid, in this case the hot gases that are released within the combustion zone. It leads to a reduction in density, to an increase of the gases buoyancy, and thus to a turbulence in the atmospheric flow. If the buoyancy-induced flows interact with the upper layers of the atmosphere, then a feedback mechanism can occur, modifying the local wind or the moisture, and therefore the conditions of the fire propagation.

As to radiation, it corresponds to the energy transferred from one material to another by the motion of electromagnetic waves. It increases the molecular activity of the substance and leads to an increase of the temperature. At the fire front, radiation occurs at very different scales, inside the porous fuel bed as well as in the gaseous phase of the flame above the fuel bed. While the heat transfer inside the fuel bed is commonly modeled by diffusion, radiation from the flame surface towards the fresh vegetation depends on the local conditions (topography, wind conditions, tilt angle of the flame with the ground surface).

In addition to heat transfer, a wildfire is also associated with mass transfer with the release of burning particles at the fire front. Indeed, the thermal decomposition of the solid vegetation is not complete and this leads to the formation of soot. These particles suspended in the ambient air grow, agglomerate or coagulate, and even oxidize once they reach the top of the flame, where the chemical reactions are less intense than at the interface with the vegetation layer.

The propagation of a fire is highly dependent upon the processes occuring at the front, at the interface between the burnt and unburnt vegetation. A flame is therefore defined by the complex interaction, in space and time, between the domain of chemistry kinetics (occuring on the scale of molecules) and the domain of heat transfer (occuring on scales ranging from millimetres up to kilometres). The characterization of the combustion is relevant at a fine scale where the theory of turbulence can be applied, whereas the flame propagates at a large scale depending on the medium in which the fire is ignited. Due to the heterogeneous conditions on the ground surface, the rate of spread changes locally, so the fire front may split into multiple heads moving at different speeds. These speeds are defined by the ratio of chemical energy release rate by the energy needed to raise the vegetation to its ignition temperature [22].

5. Premixed Combustion Model

This chapter presents the construction of the two-dimensional combustion model based on Jan Mandel's work [13], which integrates the main features of a fire via the reaction-diffusion equations. It will give a first insight on the behavior of the fire front speed, in particular in terms of the vegetation characteristics, one of the four parameters defining the wildfire rate of spread in reference [22]. The idea is therefore to study the efficiency of data assimilation when the flame speed is dependent on the vegetation distribution in the computational domain, assuming the initial location of the fire is known. More precisely, this chapter discusses the equations to solve and the validation of the code using an analytical solution derived from the KPP analysis.

5.1 State of the art: data assimilation for wildfire propagation

In reference [13] Jan Mandel applies the Ensemble Kalman Filter, a Monte-Carlo implementation of the Bayesian update problem developed by Evensen [23], as a data assimilation tool to improve the prediction of a wildfire propagation. The objective is to show the feasibility of this technique so as to reduce the uncertainties in a fire propagation, in terms of model parameters and initial flame position.

To this purpose, a simple model based on a PDE approach is used so as to insure a good physical behavior. Reaction-convection-diffusion equations are considered to model a fire in a surface layer just above the ground surface. Two variables, the temperature and the fuel mass fraction, are defined over a two-dimensional model, and they are coupled through the reaction rate, based on the Arrhenius equation. It is known that such model tracks the development of a sharp wave, whose characteristics (such as the width and the propagation speed) are defined by the prescribed model parameters. In case of a fire, a significant uncertainty in them leads directly to an erroneous flame propagation. Due to this inherent uncertainty in the model, Jan Mandel's work aims at assimilating the fields using measurements of temperature at selected points during the simulation. In practice, these observations could derive from multi-spectrum infrared photographies taken from airplanes or from sensors that are located along the fire path. Furthermore, as a forest fire starts in general at a single location and develops primarily as a circle, a homogeneous fuel load is modeled everywhere except at the initial location of the fire in the center of the domain.

Considering a fire in a surface layer just above the ground, the reaction-convection-diffusion equations are of the following form:

$$\begin{aligned} \frac{dT}{dt} &= \nabla(k\nabla T) - V\cdot\nabla T + A\Big(S\exp\Big[-\frac{B}{T-T_1}\Big] - C\,(T-T_1)\Big) \\ \frac{dY}{dt} &= -C_Y\,Y\,r(T) = -C_Y\,Y\exp\Big[-\frac{B}{T-T_1}\Big] \end{aligned} \tag{5.1}$$

with:

- $T\,(K)$: the temperature of the fire layer,
- $Y \in [0;1]$: the relative amount of fuel remaining,
- $k\,(m^2 s^{-1})$: the thermal diffusivity,
- $A\,(K s^{-1})$: the temperature rise per second at the maximum burning rate with full initial fuel load and no cooling present,
- $B\,(K)$: the proportionality coefficient in the Arrhenius law,

- $C\,(K^{-1})$: the scaled coefficient of the heat transfer to the environment,
- $C_Y\,(s^{-1})$: the fuel relative disappearance rate,
- $T_1\,(K)$: the ambient temperature,
- V: the homogenized wind velocity of the air, calculated according to the local topography.

The reaction rate $r(T)$ couples the reaction process with the diffusion via the temperature variable T. There is an offset in the Arrhenius law so as to force zero reaction at ambient temperature T_1 and to concentrate the reaction zone in the vicinity of the fire front. As reaction only proceeds in a very thin region of the domain, there is enough fuel to sustain combustion and to allow flame propagation. Otherwise, if there were combustion at ambient temperature T_1, by the time a combustion wave would get to a location far away from the initial source, the fuel would be totally consumed by the ongoing reaction at T_1. In terms of heat transfer, the short-range radiation and turbulent process is modeled by diffusion, which leads to the heating of the region ahead of the flame until it reaches its ignition temperature, and then to the flame propagation.

Using this approach within the context of OSE, Mandel shows that data assimilation can successfully track the propagation of the fire front even though the location of the initial combustion region is far away from the true position. The success of these experiments is, however, dependent on the quality of the temperature measurements: the perturbed solution converges towards the reference at each assimilation cycle if the data are able to bring information on the propagation process.

5.2 Reaction-diffusion equations

5.2.1 PDE model

This section introduces the simple premixed model based upon conservative equations (mass, momentum, energy, species) for reactive flows. Reaction-diffusion equations describe how the concentration of temperature T and of the fuel mass fraction Y_F changes under the influence of two combined processes: 1. local chemical reactions in which the fuel is burnt and heat is released; 2. diffusion which spreads the released heat over the surface.

As the density ρ is assumed to be constant, there is no equation for the conservation of mass. Convection is neglected. Pressure is constant. The model also assumes a single-step kinetic scheme where fuel and oxidizer go to products. The pyrolysis step is not modeled. For a gaseous flame, fuel and temperature diffuse with the same coefficient D. The Lewis number, corresponding to the ratio of thermal diffusivity to chemical diffusivity, is therefore unity:

$$Le = \frac{D}{\rho\,(k\,D)\,C_p} \approx 1 \tag{5.2}$$

The model assumes stoichiometric conditions, meaning that the proportions of fuel and oxygen are such that the total amount of fuel is consumed by the reaction process and that there is no excess of oxygen. So, within the domain, the burnt region is at the hot gas temperature T_2 and there is no remaining fuel, while in the unburnt region the fuel is still preserved at the fresh gas temperature T_1. The fuel mass fraction Y_F is initially uniformly distributed over the surface, except at the place where the flame begins: $Y_F(x, y, t = 0) = Y_F^0$. Note that this vegetation initial condition will change for simulations using data assimilation so as to study the influence of the fuel distribution on the fire rate of spread.

Under these assumptions, the conservative equations for a reacting flow become [24]:

$$\frac{\partial \theta}{\partial t} = D\,\nabla(\nabla\theta) + \dot{\omega} - \lambda\theta \tag{5.3}$$

$$\frac{\partial Y}{\partial t} = k\,D\,\nabla(\nabla Y) - \dot{\omega} \tag{5.4}$$

with

- $\theta = (T - T_1)/(T_2 - T_1)$ the reduced temperature,
- $Y = Y_F/Y_F^0$ the reduced fuel mass fraction,
- D the heat diffusion coefficient,
- λ the heat loss (mainly due to radiation),
- $\dot{\omega}$ the reaction rate,
- k the diffusion control parameter: in a gaseous flame the fuel diffuses like heat ($k = 1$), but in case of a wildland fire, the fuel is supposed to be fixed on the ground and so it does not to diffuse ($k = 0$). Both cases will be investigated in this work.

It is known that this parabolic system of equations admits traveling combustion waves as solution. It models the propagation of a reactive interface at a given speed from the burnt region towards the unburnt region. It represents indeed a sharp transition between two states, where the fuel has burnt ($\theta = 1/Y = 0$) and where the fuel is still preserved ($\theta = 0/Y = 1$) on the opposite side of the front. The speed at which these waves travel defines the fire rate of speed.

5.2.2 Reaction rate

The reaction rate $\dot{\omega}$ defines the rate at which the chemical reaction between fuel and oxygen occurs given the temperature and the remnant amount of fuel. It is directly in link with the combustion characteristics such as the width of the burning region and the rate of spread.

Arrhenius reaction model

Jan Mandel considers a semi-empirical reaction rate $\dot{\omega}$ based on the following Arrhenius law:

$$\dot{\omega} = Y\, exp\Big(\frac{-B}{T - T_1}\Big) \tag{5.5}$$

There is a temperature offset so as to force zero reaction at ambient temperature T_1 and to confine the reaction in a relatively thin zone located along the flame front (where the temperature T is significantly higher than the fresh gas temperature T_1). The fuel consumption is therefore a smooth function of temperature, with B describing the characteristics of the fuel. This approach neglects the effects of turbulence in the vegetation layer and is only relevant when chemical time scales are larger than turbulent time scales (low Damköhler number), corresponding to a regime where reactants mix rapidly and burn slowly.

Eddy Break Up formulation

Since this work will focus on turbulent flames, an Eddy Break Up (EBU) is considered instead of an Arrhenius law. In this case, reaction rates are controlled by turbulent motions and are based on an analysis assuming high Reynolds and Damköhler numbers. This means that chemistry does not play any explicit role in the reaction. So the reaction zone is viewed as a collection of fresh and burnt fuel pockets carried by turbulent eddies. With this EBU formulation, the mean reaction rate is given by:

$$\dot{\omega} = a\, Y\, \theta \tag{5.6}$$

with a the reaction rate factor dependent on the turbulent kinetic energy, dissipation rate and density.
Note that this formulation does not include any effect of chemical kinetics and tends to overestimate the reaction rate. However, it provides good results as it limits the reaction to the front thickness.

5.3 Validation with an analytical solution

To validate the solver implementation, the model is simplified to a configuration which has an analytical solution. This provides therefore a reference to check the validity of the results given by the model, like the prediction of the rate of spread. This will be useful to check the precision of the code and to learn about flame propagation.

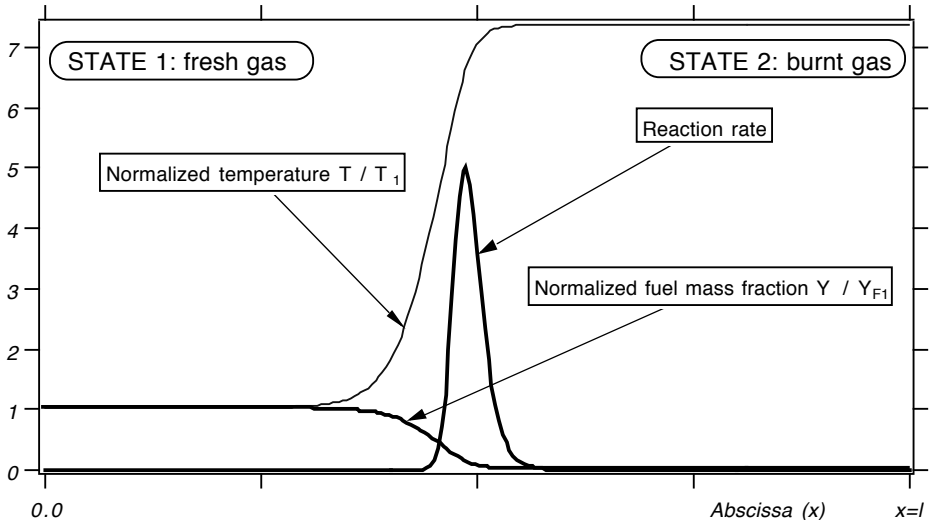

Figure 5.1: Basic configuration for computations of one-dimensional premixed flames. State 1: fresh gas quantities. State 2: burnt gas quantities. Interface: chemical reactions releasing heat.

5.3.1 KPP analytical solution

The model is reduced to a one-dimensional steady-state case with a reaction zone characterized by a laminar flame speed, corresponding to the so-called Fisher-Kolmogorov equation. The fuel is assumed to diffuse like heat ($k = 1$). Furthermore, only an adiabatic flame is considered, meaning that there is no radiation ($\lambda = 0$). For such a configuration, equations (5.3) and (5.4) become:

$$\frac{\partial \theta}{\partial t} = D \frac{\partial^2 \theta}{\partial x^2} + a\, Y\, \theta \tag{5.7}$$

$$\frac{\partial Y}{\partial t} = D \frac{\partial^2 Y}{\partial x^2} - a\, Y\, \theta \tag{5.8}$$

Additionally, the initial condition satisfies $Y + \theta = 1$. It means that the reduced temperature can be any signal going from 0 in the fresh gas to 1 in the burnt gas, as presented in figure 5.1, while the reduced fuel mass fraction goes from 1 in the fresh gas to 0 in the burnt gas. Thus, reaction can only occur in the vicinity of the flame front, when both variables θ and $(1 - \theta)$ are not zero. Therefore, the solution must be a front propagating from the burnt to the fresh gas, at a constant speed s_L once the flame is steady. The relation $Y + \theta = 1$ is therefore guaranteed at any time of the integration.

With this framework, equations (5.7) and (5.8) are equivalent to one single equation of the form:

$$\frac{\partial \theta}{\partial t} = D \frac{\partial^2 \theta}{\partial x^2} + a\,(1 - \theta)\,\theta \tag{5.9}$$

This equation can be solved analytically using a KPP analysis [24], as explained in appendix A, under the following assumptions: 1. a frozen turbulence; and 2. a flame propagation controlled by the turbulent flame leading edge. With a frame reference attached to the flame, this analysis provides an expression for the flame speed so that s_L is a function of both reaction and diffusion processes. It proves indeed that the wave solution propagates at a constant speed $s_{L,KPP} = 2\sqrt{aD}$ and has a constant flame thickness proportional to $\delta_{L,KPP} = 1/2\,\sqrt{D/a}$.

In practice, $s_{L,KPP}$ overestimates the true flame speeds, but provides all trends precisely [25]. As to the flame thickness δ_L, it is identified as the inverse of the maximum temperature gradient, denoted by δ_L^0 and represented in figure 5.2. Note that δ_L^t corresponds to the total thickness, that is to say the distance over which the reduced temperature θ changes from 0.01 to 0.99. This highlights the sharpness of the fire front. However, this is not useful in practice: slow reactions taking place in the burnt gases create in general a long temperature tail, leading to too large values for δ_L^t.

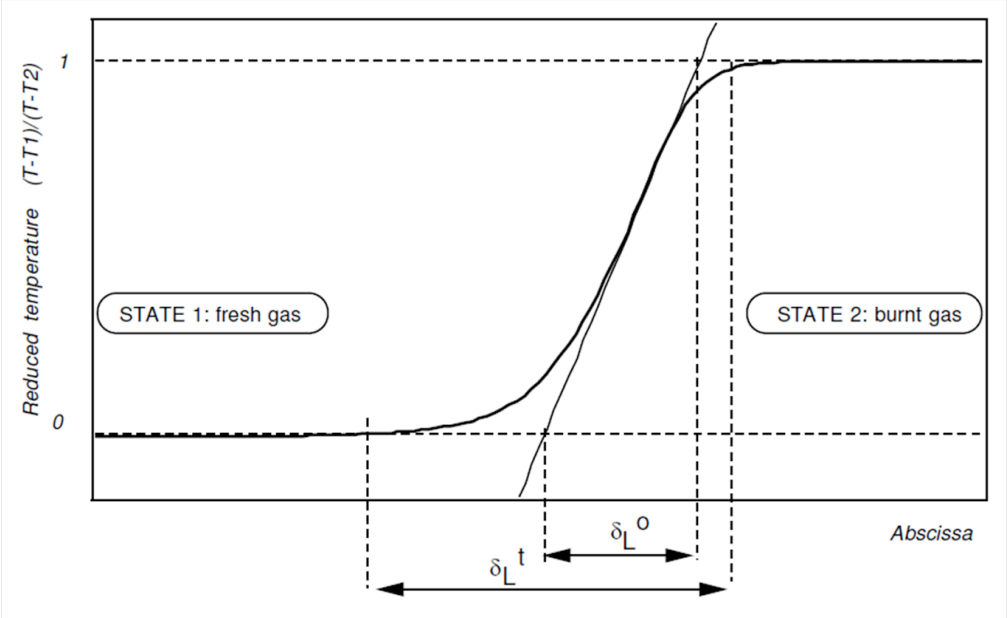

Figure 5.2: Definition of flame thickness for a premixed flame.

5.3.2 Validation for a gaseous flame

The system of conservative equations has been coded in the 2D fire solver, insuring no flux at the boundary, and is used as a fire propagation prototype in this work. This is adapted to represent the 1D configuration corresponding to the KPP analytical solution: the fire propagates along the x-axis as a plane front with the initial discontinuity located at $x = 3/4\,L$ (L representing the length of the square domain). This solver does not assume $Y + \theta = 1$, keeping an equation for both state variables θ and Y. The objective is to ensure that the flame speed and thickness provided by the solver are consistent with the KPP analytical solution.

The model is solved using a central finite difference scheme of order 2 in space, and is integrated in time using a RK4 numerical scheme. The square domain is discretized with a regular mesh ($\Delta x = \Delta y = 1$), the mesh size is 201×201 so as to capture correctly the fire front. The time step Δt is fixed. Two hundred time steps are run. These numerical parameters are chosen so as to satisfy the stability and precision requirements of the solver. For a pure diffusion, the RK4 scheme is stable if and only if [26]:

$$F = \frac{D\,\Delta t}{\Delta x^2} \leq 0.725 \tag{5.10}$$

with F the Fourier number. This condition is verified experimentally for the reaction-diffusion equation. As to the reduced reaction parameter $R = a\Delta t$, it shall be chosen according to F so as to ensure physical compatibility and to avoid the flame reaching the domain boundaries.

In this validation, $D = 0.4$ for both temperature and fuel, $a = 0.2$. $\Delta t = 0.5$ is fixed. The initial flame is placed at $x = 150$ with burnt gas on the right and fresh gas on the left. The theory predicts therefore the propagation of a wave from the burnt gas to the fresh gas at a speed of magnitude $s_{L,KPP} = 2\sqrt{aD} = 0.56$.

Figure 5.3 shows the temperature profile θ at different times corresponding to this configuration: at $t = 4$ the front is sharper, but step by step it becomes smoother until it stabilizes to a constant slope before $t = 24$. So the flame front reaches rapidly a permanent regime, and then the flame propagates without deformation as expected from the KPP analysis.

Flame speed

The flame speed $s_L = dx_c/dt$ can be measured directly by considering the wave front at different times. x_c represents the position of the front, which shall be measured at a reference temperature θ_c. Commonly, the reference is fixed to $\theta_c = 0.5$. Using this definition, the solver gives $s_L = 0.55$. So it reproduces the KPP solution with less than 2% error as $s_{L,KPP} = 0.56$.

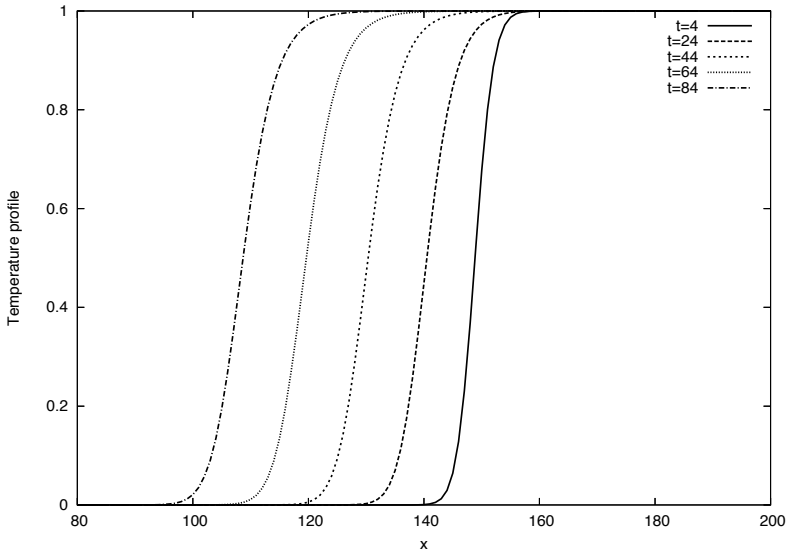

Figure 5.3: Traveling wave front from burnt gas to fresh gas (from right to left) for parameters $D = 0.4$ and $a = 0.2$ - The front represents the profile of the reduced temperature θ in the course of the model integration for constant time steps between $t = 0$ and $t = 100$.

Flame thickness

As to the flame thickness δ_L, it is determined as the inverse of the maximum temperature gradient using the θ-profile as stated in equation (5.11).

$$\delta_L = \frac{\left(\theta_{max} - \theta_{min}\right)}{\left|\max\left(\frac{\delta\theta}{\delta x}\right)\right|} = \frac{1}{\left|\max\left(\frac{\delta\theta}{\delta x}\right)\right|} \tag{5.11}$$

The temperature gradient is maximum in the vicinity of x_c, it leads to $\delta_L = 8.8$, while $\delta_{L,KPP} = 0.7$. There is therefore roughly a factor 15 between the analytical prediction and the result provided by the solver. However, it is well known that $\delta_{L,KPP}$ underestimates the real flame thickness [24] by a factor going from 2 to 4. The present factor may be explained by the non-usual form of the reaction rate considered here (the EBU form).

As to conclude, the trends provided by the KPP analysis are in excellent accordance to the results given by the 2D fire solver in terms of flame speed, but not in terms of flame thickness. Neverthless, the dependence of both s_L and δ_L with a and D are reproduced by the solver. The solution will be compared with the case $k = 0$.

5.3.3 Comparison with a fire flame

The same analysis is carried out without fuel diffusion ($k = 0$). In this case, the condition $\theta + Y = 1$ is not satisfied everywhere. So it does not correspond to the rigorous framework of the KPP analysis. However, results (presented in figure 5.4) show that $\theta + Y$ goes from 0.85 to 1.15. The KPP estimation for flame speed remains very good because the leading edge of the flame, where $\theta = 0$, is also a region where $Y = 1$. So in this region, having $k = 0$ or $k = 1$ does not make a difference.

As a result, the flame speed obtained with the fire solver does not change significantly when diffusion is cancelled in the Y-equation. From figure 5.5, it can be deduced that $s_L = 0.53$, while $\delta_L = 11.11$. These values are similar to those describing the wave propagation for a gaseous flame ($k = 1$). So the KPP formula

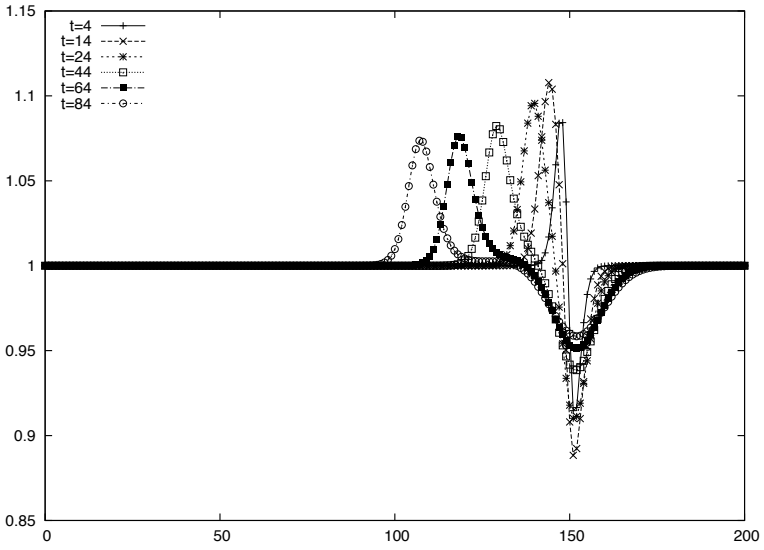

Figure 5.4: $Y + \theta$ profile over time for a fire flame with $D = 0.4$ and $a = 0.2$.

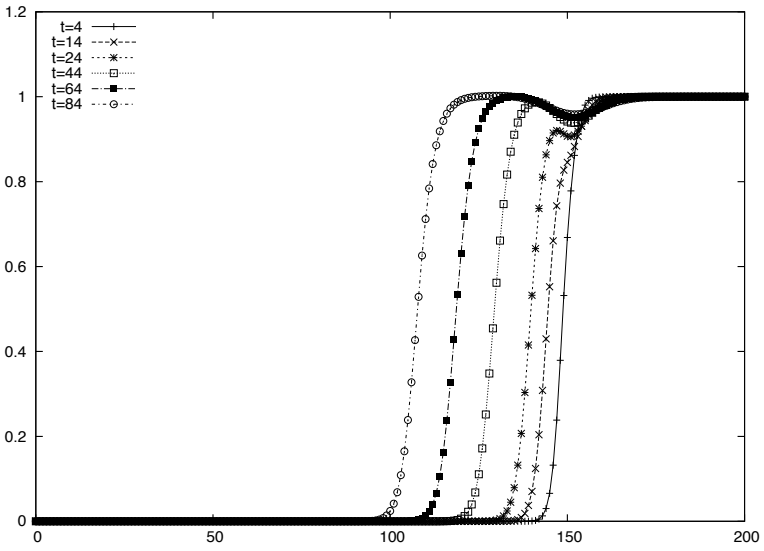

Figure 5.5: Traveling wave from burnt gas to fresh gas for $D = 0.4$, $a = 0.2$ and $k = 0$.

remains therefore valid even for $k = 0$. However, even though the flame speed is the same for $k = 0$ and $k = 1$, the temperature field is different in the burnt gases as the fuel property propagates to θ via the reaction term.

5.4 Adaptation to wildfire propagation

A model of premixed combustion has been proposed to propagate a fire front, with two state variables, the reduced temperature θ and the reduced fuel mass fraction Y. The model has been applied and validated

in a one-dimensional case using a KPP analytical solution. The equations to code in 2D are summarized below:

$$\frac{\partial \theta}{\partial t} = D\Delta\theta + aY\theta \quad (5.12)$$

$$\frac{\partial Y}{\partial t} = kD\Delta Y - aY\theta \quad (5.13)$$

with $k = 1$ for a gaseous flame and $k = 0$ for a fire, D describing the thermal diffusion.

This set of equations leads to a front propagating at a speed diagnosed by the KPP analysis, with $s_{L,KPP} = 2\sqrt{aD}$, within 2% accuracy. Its flame thickness will be given by $\delta_{L,KPP} = 1/2\sqrt{D/a}$ with roughly a factor 15. The scaling provided by the KPP analysis will be extremely useful to determine the mesh size and the flame velocities in this code.

5.4.1 Transformation from solid to gas

In the case of a real wildfire, the vegetation transforms into a combination of gases when the temperature is high enough to allow the reaction to proceed. So this ignition process occurs in the vicinity of the flame where the reduced temperature changes radically from 0 to 1. Far away from the flame, the vegetation is still at a fresh temperature T_1 and has not transformed into gases yet.

In this preliminary study, the modeling of the transformation from vegetation to gases is simplified significantly. Pyrolysis is not considered, instead the fuel is supposed to be fixed on the ground and the transformation is assumed to occur instantaneously from solid to gas. In other words, when the flame front approaches, the vegetation turns directly into gas pockets, ready to be burnt.

5.4.2 Fire initial condition

In general, a fire starts at one location and propagates as a circular front during a first phase. In the model, the fire is therefore initialized as a circular flame at the centre of the domain. Where the fuel has burnt, there is no vegetation ($Y = 0$) and the temperature is maximum ($\theta = 1$). In the rest of the domain, as the vegetation is randomly spread at a fresh temperature T_1, fuel pockets are located at random positions with a random intensity such that $0 < Y < 1$. This initial condition is represented in figures 5.6 and 5.7.

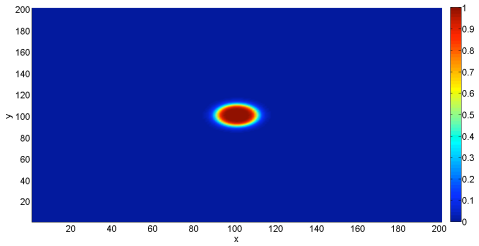

Figure 5.6: Temperature initial condition.

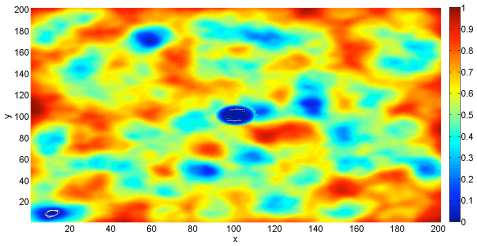

Figure 5.7: Fuel initial condition.

5.4.3 Properties of the state variables

A sample integration of the model, associated to this wildfire initial condition, is carried out with $D = 0.3$ and $a = 0.2$ as model parameters. Due to the random distribution of the fuel, the fire front splits into numerous heads propagating at a specific speed, determined by the local amount of fuel. The flame propagates in the direction of the fuel pockets of higher intensities, while it stops when it encounters a zone with a very small amount of fuel. This zone acts indeed as a barrier to the propagation. So the front does not have a circular shape, instead its geometry is defined as the isocontour $\theta_c = 0.5$. Figures 5.8 and 5.9 show the temperature and fuel fields at time $t = 100$.

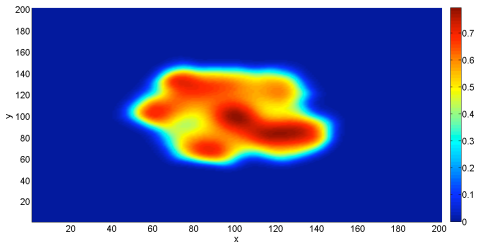

Figure 5.8: Temperature field at $t = 100$.

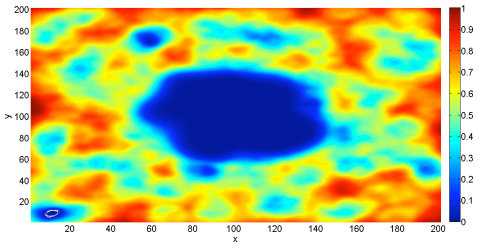

Figure 5.9: Fuel field at $t = 100$.

From this sample integration, it is clear that the temperature is the highest where there is no fuel left, inside the flame front. However, the temperature T is not exactly equal to the burnt temperature T_2. At the central location, θ is indeed about $0.7 - 0.8$, instead of 1. This property is due to a thermal diffusion process occuring at the centre of the flame, which does not occur when the fuel distribution is homogeneous ahead of the fire front, or equivalently when the condition $\theta + Y = 1$ is always satisfied. So it raises from the physics of the model: when the propagation in one direction stops, the diffusion is predominant and therefore the temperature within the fire decreases. The higher the diffusion coefficient D, the stronger the thermal diffusion within the front.

6. New Formulation of the Fire Spread Model

The main property of a front is its rate of spread, which depends on multiple factors, for instance the local vegetation characteristics, topography and wind conditions [22]. This study focuses on the influence of the vegetation distribution only, modeled as a reduced fuel mass fraction Y. In chapter 5, the premixed combustion model gives an insight of how the temperature field is affected by a random fuel distribution. It is observed that the fire moves towards the fuel pockets, while it stops when encountering non-burnable regions (also called fuel breaks such as roads, lakes or cliffs). However, in the literature, the rate of spread is recognized as the main fire feature and as the critical quantity to assimilate. The idea is therefore to define a model with the flame speed as control parameter using a parametrization of the vegetation dependence. A new model is therefore built, assuming that a fuel mapping of the region subject to a fire is available. It will be based on the KPP analysis and generalized to an anisotropic wildfire propagation.

This reformulation is also motivated by the operational constraints associated to a fire forecast. A wildfire model may not be based on conservative equations if the objective is to predict the propagation faster than real-time. Within this framework, it appears more realistic here to build a model for the rate of spread as a function of the vegetation distribution, and also as a function of the weather conditions and topography in future investigations. This means that the simulation of the evolution of the fuel load is not required. However, it could be useful for a posteriori simulations whose objective is to study the long-range fire effects on the environment and on the atmosphere (in terms of fire severity). The formulation of the model depends therefore on the motivations of the investigations that follow the simulations.

6.1 Isotropic vegetation distribution

To introduce the rate of spread, the fire model is reduced to one single PDE describing the evolution of the progress variable c. This formulation is equivalent to the premixed model of two equations if the condition $\theta + Y = 1$ is satisfied. This reformulation is based on the KPP analysis, so in a preliminary step the derivation of the model will be carried out considering an isotropic vegetation distribution ($Y = 1$) over the computational domain.

6.1.1 Introduction of the progress variable

Within the framework of the KPP analysis [24], the model is reduced to a one-dimensional steady-state case, whose solution is a front propagating from the burnt to the fresh gas at a constant speed once the flame is steady. Using D and a as model parameters, the standard reaction-diffusion PDE is given by:

$$\frac{\partial c}{\partial t} = D\,\frac{\partial^2 c}{\partial x^2} + a\,c(1-c) \tag{6.1}$$

when both convection and radiation are neglected. This means that only an adiabatic flame is considered and that the chemical reactions only occur in the vicinity of the fire front. The KPP analysis leads to the definition of the constant flame speed $s_{L,KPP}$ and thickness $\delta_{L,KPP}$ as a function of D and a. Indeed,

$$\left\{\begin{array}{l} s_{L,KPP} = 2\sqrt{aD} \\ \delta_{L,KPP} = \frac{1}{2}\sqrt{\frac{D}{a}} \end{array}\right. \quad \Rightarrow \quad \left\{\begin{array}{c} D = s_{L,KPP}\,\delta_{L,KPP} \\ a = \frac{1}{4}\frac{s_{L,KPP}}{\delta_{L,KPP}} \end{array}\right. \tag{6.2}$$

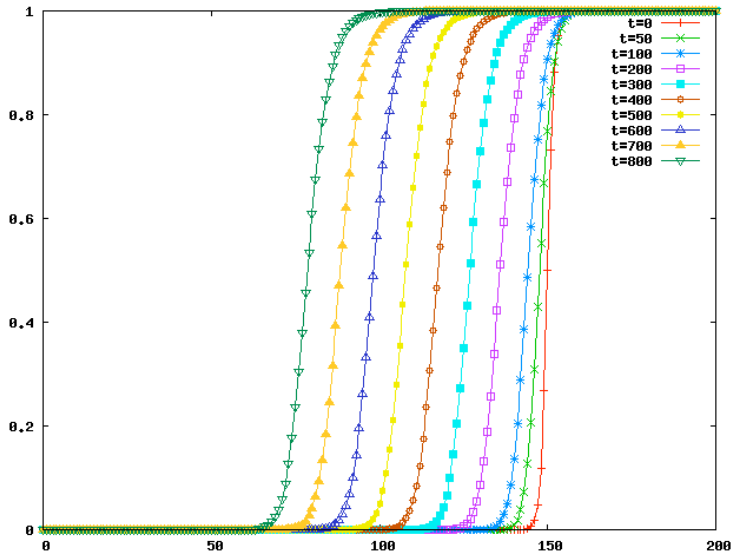

Figure 6.1: Profile of c over time - 1D initial condition, $\delta_L = 0.8$ and $s_{L,KPP} = 0.1$.

These equations define a unique relation between the coefficients (D, a) and $(s_{L,KPP}, \delta_{L,KPP})$. So the two flame properties $(s_{L,KPP}, \delta_{L,KPP})$ can be directly introduced in equation (6.1).

While the trend of the speed provided by the KPP analysis is in excellent accordance with the speed of the simulated front, it is not the case for the flame thickness. So the flame is thickened numerically to ensure a good CFD resolution and to capture properly the front. The flame thickness is therefore prescribed as a numerical parameter in terms of the grid step size: typically, $\delta_{L,o} \approx 8\,\Delta x$. It introduces a restriction on the flame velocity as the model is a hyperbolic equation solved using an explicit RK4 scheme. CFL and Fourier conditions are satisfied if and only if

$$\nu = \frac{s_{L,KPP}\,\Delta t}{\Delta x} \quad < \quad \frac{0.725}{\Delta x}$$

with ν the Courant number, and 0.725 the stability threshold associated to the RK4 scheme [26].

In this configuration, the model with $s_{L,KPP}$ as parameter is defined as follows:

$$\frac{\partial c}{\partial t} = s_{L,KPP}\,\delta_L\,\frac{\partial^2 c}{\partial x^2} + \frac{s_{L,KPP}}{4\delta_L}\,c(1-c) \tag{6.3}$$

As a validation, the behavior of the model shall be studied as a function of the numerical parameter $\delta_L/\Delta x$. This analysis aims at defining the domain of validity of δ_L, that is to say at determining for which values of δ_L the fire model approaches the prescribed speed $s_{L,KPP}$ in equation (6.3). As for the premixed model, the square domain is discretized with a regular mesh ($\delta = 1$), the mesh size is 201×201 and the time step is fixed to $\Delta t = 0.5$.

6.1.2 Thickness as a numerical parameter

$s_{L,KPP}$ is fixed to 0.1. Given the initial condition of a fire front located at $x = 3/4\,L$, the progress variable c reaches rapidly a permanent regime and the fire front propagates at a constant flame speed. For instance, figure 6.1 represents its propagation over time for $\delta_L = 0.8\Delta x$.

Results

1D parameter study

The model is solved for different values of $\delta_L/\Delta x$ in a range between 0.1 and 1, with $\Delta x = 1$. It appears that the length of the transition regime depends on the flame thickness δ_L: the higher δ_L, the longer it takes to the system to reach a constant speed. The characteristic time τ_L is indeed approximated by the ratio $\delta_L/s_{L,KPP}$.

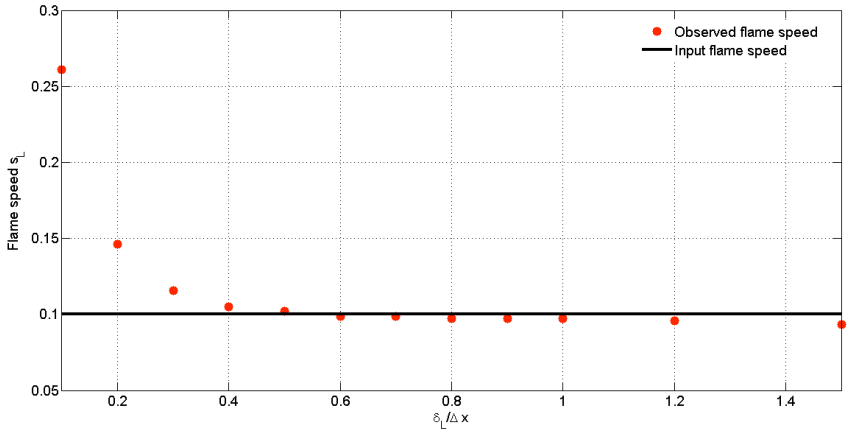

Figure 6.2: Observed flame speed as a function of the ratio $\delta_L/\Delta x$ - 1D initial condition, $s_L = 0.1$.

For each value of the ratio $\delta_L/\Delta x$, the simulated speed $s_{L,o}$ can be measured (denoted by "o" for "observation"), on the profile of c, as the distance covered by the front during the elapsed time between two integrations. The simulated flame thickness $\delta_{L,o}$ is also measured as the inverse of the maximum value of the gradient of c. Results are gathered in table 6.1, the observed speed is presented in figure 6.2.

$\delta_L/\Delta x$	$s_{L,o}$	$\delta_{L,o}/\Delta x$
0.1	0.261	5.41
0.3	0.116	6.69
0.5	0.103	9.78
0.7	0.100	13.05
0.8	0.100	15.14
0.9	0.099	17.13
1.0	0.099	18.22

Table 6.1: Measure of $s_{L,o}$ and $\delta_{L,o}$ as a function of $\delta_L/\Delta x$.

For a low ratio $\delta_L/\Delta x$, when the fire front is sharp, the flame speed does not converge towards the analytical value $s_{L,KPP} = 0.1$. More precisely, the error on the speed increases when the ratio becomes lower. For instance, for $\delta_L/\Delta x = 0.1$, $s_{L,o} = 0.261$. It is associated with a flame thickness of $\delta_{L,o}/\Delta x = 5.41$, so this high discrepancy with the KPP speed is due to the lack of resolution of the mesh size. A thickness of $5\Delta x$ is not enough to capture properly the fire front, and consequently to estimate its propagation speed.

From $\delta_L/\Delta x = 0.5$, the observed speed reproduces the KPP prediction with less than 2%. It means that if the ratio $\delta_L/\Delta x$ is high, then the flame speed is consistent with the KPP analysis. The threshold for this consistency is $\delta_{L,o}/\Delta x = 6$.

In general, there is a high discrepancy between the prescribed thickness δ_L and the simulated thickness $\delta_{L,o}$. The ratio between these two values is not constant, it is between 15 and 30 as in the premixed combustion model. As it will be explained in the following, this is due to the underestimation of the flame thickness by the KPP analysis. So as to observe a thickness $\delta_{L,o} \approx 8\Delta x$, δ_L is voluntarily low.

2D parameter study

The same study is carried out for a two-dimensional initial condition with a circular flame at the centre of the domain. As there is no fuel pocket involved, the circular fire front propagates at a constant speed in all directions. The goal is to check if the KPP analysis can predict accurately the propagation speed for this shape of the front. As to the 1D study, the thickness parameter is $\delta_L/\Delta x$ as $\Delta x = \Delta y$. Results are presented in figure 6.3.

This 2D study shows that the simulated speed $s_{L,o}$ follows the same trend as in 1D. The errors on

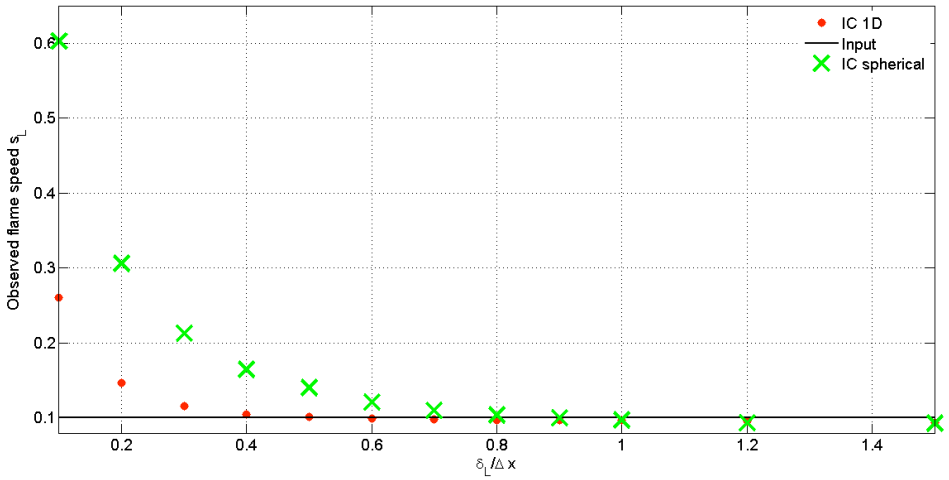

Figure 6.3: Convergence of the simulated flame speed $s_{L,o}$ towards the analytical value $s_{L,KPP} = 0.1$ as a function of the ratio $\delta_L/\Delta x$- 1D and 2D isotropic initial condition.

$s_{L,KPP} = 0.1$ grow when $\delta_L/\Delta x$ decreases, but the KPP flame speed is reproduced by less than 10% error once the condition $\delta_L/\Delta x > 0.7$ is satisfied. Indeed, for this value, $s_{L,o} = 0.11$, while $\delta_{L,o} = 14.93$. Compared to the 1D case, this configuration requires a higher flame thickness to reach the same level of accuracy of the flame speed. Indeed, in the 1D case, $s_{L,o}$ is under 0.11 as soon as $\delta_L/\Delta x > 0.3$, while the threshold is 0.7 in the 2D case.

6.1.3 Control of the flame properties

In the literature, it has been proved that the KPP analysis underestimates the real flame thickness δ_L. This has been confirmed by the previous simulations as there is a ratio of 15 to 20 between the simulated thickness and the prescribed value. However, in the context of data assimilation, it is important to control the flame thickness so as to diagnose the correct flame speed associated to the true, background or analysed trajectory. For this purpose, the expression of the parameters D and a in equations (6.2) shall be adapted in order to define an accurate diagnosis of the flame properties. A more appropriate numerical parameter to characterize the flame thickness, denoted by β, shall be introduced.

Analysis

In the context of the KPP analysis, the model is defined in the frame of reference attached to the flame. Hence,

$$\frac{\partial c}{\partial t} = s_{L,KPP}\,\frac{\partial c}{\partial x} \tag{6.4}$$

$$\Rightarrow s_{L,KPP}\frac{\partial c}{\partial x} = D\,\frac{\partial^2 c}{\partial x^2} + a\,c(1-c) \tag{6.5}$$

At the inflection point of the fire front, $\frac{\partial^2 c}{\partial x^2} = 0$ and $c \approx 0.5$. By definition of the flame thickness, the following condition is satisfied: $\partial c/\partial x = \max|\partial c/\partial x| = 1/\delta_L$. Inserting these relations into equation (6.5) leads to $\delta_L = 16\,\delta_{L,KPP}$. Indeed,

$$\begin{aligned} \frac{s_{L,KPP}}{\delta_L} &= \frac{a}{4} \\ \Rightarrow \delta_L &= \frac{2 s_{L,KPP}}{a} = 8\sqrt{\frac{D}{a}} \\ \Rightarrow \delta_L &= 16\,\delta_{L,KPP} \end{aligned} \tag{6.6}$$

as $\delta_{L,KPP} = 1/2\sqrt{D/a}$.

This analysis is consistent with the ratio $\delta_{L,o}/\delta_{L,KPP}$ measured in the simulations. To capture property the fire front, the flame thickness is prescribed so as to ensure $\delta_L = 8\Delta x$. This leads to a new definition of δ_L with a numerical parameter β, of order O(1/2):

$$\delta_L = 8\sqrt{\frac{D}{a}} = 8\,\beta\,\Delta x \tag{6.7}$$

This definition of the flame thickness in equation (6.7) leads to a new unique relation between coefficients (D, a) and $(s_{L,KPP}, \delta_L)$:

$$\left\{\begin{array}{c} \sqrt{aD} = \frac{1}{2}\,s_{L,KPP} \\ \sqrt{\frac{D}{a}} = \beta\Delta x \end{array}\right. \iff \left\{\begin{array}{c} D = \frac{1}{2}\,\beta\,s_{L,KPP}\,\Delta x \\ a = \frac{1}{2\,\beta\,\Delta x}\,s_{L,KPP} \end{array}\right. \tag{6.8}$$

The 1D model of fire propagation is defined by the following PDE:

$$\frac{\partial c}{\partial t} = \left(\frac{\beta\,s_{L,KPP}\,\Delta x}{2}\right)\frac{\partial^2 c}{\partial x^2} + \left(\frac{s_{L,KPP}}{2\beta\Delta x}\right)c(1-c), \quad \beta > \frac{1}{2} \tag{6.9}$$

Equivalently in 2D, with $\delta = \min(\Delta x, \Delta y)$,

$$\frac{\partial c}{\partial t} = \left(\frac{\beta\,s_{L,KPP}\,\delta}{2}\right)\Delta c + \left(\frac{s_{L,KPP}}{2\beta\delta}\right)c(1-c), \quad \beta > \frac{1}{2} \tag{6.10}$$

Diagnostics

So as to validate the new formulation of the model and to assimilate the fire front speed in the future experiments, it is necessary to establish diagnostics on the properties of the flame. They are presented in the following for a general framework, the propagation for a fire over a two-dimensional surface with an anisotropic vegetation distribution as represented in figure 6.4.

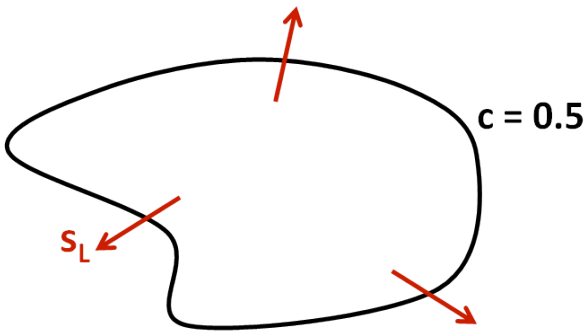

Figure 6.4: Schematic representation of an anisotropic fire propagation, with a non-constant flame speed s_L along the isocontour $c = 0.5$.

Fire propagation speed

When the vegetation is not spread uniformly over the domain, all the points of the front do not move at the same speed. However, the objective is to introduce a quantity describing the front (defined by the isocontour $c = 0.5$) at a given time. This quantity is the average speed of the front, denoted by $\bar{s}_L^*$ and defined as the following ratio:

$$\bar{s}_L^* = \frac{\displaystyle\int_{c=0.5} s_L\,dS}{\displaystyle\int_{c=0.5} dS} \tag{6.11}$$

with s_L the local flame speed at any point along the isocontour $c = 0.5$.

Using the KPP analysis, two diagnostics of $\bar{s}_L^*$ have been developed. First of all, it is proved that the flame speed is determined by the rate of change of the progress variable c over the whole spatial domain.

This leads to the first diagnostic of $\bar{s}_L^*$, given by equation (6.12):

$$s_{L,d_1} = \frac{1}{\displaystyle\int_{c=0.5} dS} \frac{d}{dt}\Big(\iint c(x,y)\, dx\, dy \Big) \tag{6.12}$$

Indeed,

$$\begin{aligned} \frac{d}{dt} \iint c(x,y)\, dx\, dy &= \iint \frac{\partial c}{\partial t}(x,y)\, dx\, dy \\ &= \int s_L(x,y)\ |\nabla c|\ dx\, dy \\ &= \int_{c=0.5} s_L\, dS \\ &= \bar{s}_L^* \int_{c=0.5} dS \end{aligned}$$

as $\partial c/\partial t = s_L\ |\nabla c|$ (generalization of the change of frame in 1D), $|\nabla c| = \Sigma = \ dS/(dx\, dy)$ (representation of the length of the flame per unit area), and as there is no transport problem at the domain boundaries (no convection, no radiation).

The definition of the reaction-diffusion equation leads to the second diagnostic in equation (6.13):

$$\begin{aligned} \frac{d}{dt} \iint c(x,y)\, dx\, dy &= \iint \frac{\partial c}{\partial t}(x,y)\, dx\, dy \\ &= \iint \Big[\Big(\frac{\beta\, s_L\, \delta}{2} \Big) \Delta c + \Big(\frac{s_L}{2\beta\delta} \Big) c(1-c) \Big]\, dx\, dy \\ &= \bar{s}_L^* \int_{c=0.5} dS \end{aligned}$$

using the relation $\displaystyle\iint \Delta c = 0$. Hence,

$$s_{L,d_2} = \frac{1}{\displaystyle\int_{c=0.5} dS} \iint \Big(\frac{s_L(x,y)\, c(1-c)}{2\beta\delta} \Big)\, dx\, dy \tag{6.13}$$

with $s_L(x,y)$ the rate of spread expressed in terms of the non-uniform vegetation distribution $Y = Y(x,y)$. This second diagnostic shows that, in this study context, the front rate of spread is also determined by the integral of the source term. However, in general, it is important to know that the rate of spread results from the combination of two processes, diffusion and reaction.

To conclude, the mean flame speed $\bar{s}_L^*$ can be either diagnosed by equation (6.12) or by equation (6.13), respectively denoted by s_{L,d_1} and s_{L,d_2}. When referring to any of these two diagnostics, the speed is denoted by $s_{L,d}$.

Fire front thickness

The flame thickness is diagnosed by the inverse of the maximum gradient of the progress variable c. While the analytical value is given by $\bar{\delta}_L^* = 8\beta\delta$, the diagnostic $\delta_{L,d}$ is defined as follows:

$$\delta_{L,d} = \frac{1}{\max \big| \frac{\partial c}{\partial n} \big|_{c=0.5}} \tag{6.14}$$

where n represents the normal direction to the propagation.

Characteristic response time

The definition of the diagnostics for the flame speed and thickness leads to a third diagnostic (6.15). Indeed, the fire spread model is associated to a characteristic response time denoted by τ_L, defined as the ratio between the flame thickness and the flame speed. This parameter is diagnosed by the value $\tau_{L,d}$:

$$\tau_{L,d} = \frac{\delta_{L,d}}{s_{L,d}} \approx \frac{\bar{\delta}_L^*}{\bar{s}_L^*} \tag{6.15}$$

Validation

This series of diagnostics is tested for different values of the numerical parameter β so as to determine the range in which it provides acceptable flame properties: 1. a flame speed sufficiently close to the analytical value $s_{L,KPP} = 0.1$; 2. a thickness which allows a good tracking down of the sharp leading edge of the fire; and 3. a characteristic response time which guarantees the convergence towards a permanent regime within a reasonable amount of time.

Numerical integration tool

In the diagnostics, the integrals are numerically computed using a composite trapezoidal rule. In a one-dimensional context, considering a function f defined over the interval $[x_{min}; x_{max}]$, its integral is approximated as follows:

$$\int_{x_{min}}^{x_{max}} f(x)\,dx \approx \Delta x \left[\frac{f(x_{min}) + f(x_{max})}{2} + \sum_{k=1}^{n_x-1} f\left(x_{min} + k\,\Delta x\right) \right] \tag{6.16}$$

if the mesh grid is uniform with $\Delta x = (x_{max} - x_{min})/n_x$, n_x representing the number of uniform subintervals. The error analysis is, in this context, of order $\mathrm{O}(\Delta x^3)$. Note that the generalization of this numerical integration to 2D is straightforward and is not developed here.

1D front propagation

The flame speed diagnostics are simplified in the case of an isotropic vegetal fuel distribution. Indeed, the simulated speed is a constant equal to $\bar{s}_L^*$. Hence,

$$s_{L,d} = \frac{d}{dt} \int_{x_{min}}^{x_{max}} c(x,t)\,dx = \left(\frac{s_{L,KPP}}{2\beta\Delta x}\right) \int_{x_{min}}^{x_{max}} c(x,t)\,(1 - c(x,t))\,dx \tag{6.17}$$

For this series of experiments, $s_{L,KPP} = 0.1$, $\delta_L = 8\beta\Delta x$ with β varying from 0.6 to 1.6. The simulated speed is diagnosed using the relation (6.17) only. Results are presented in figures 6.5-6.6-6.7 for $\beta \in [0.8-1.4]$, and summarized in table 6.2.

β	$s_{L,KPP}$	$s_{L,d}$	$\delta_L/\Delta x$	$\delta_{L,d}/\Delta x$	τ_L	$\tau_{L,d}$
0.6	0.1	0.1159	4.8	6.5	48	41
0.8	0.1	0.1058	6.4	8.2	64	61
1.0	0.1	0.1026	8	9.2	80	78
1.2	0.1	0.1013	9.6	11.7	96	95
1.4	0.1	0.1003	11.2	13.1	112	112
1.6	0.1	0.0998	12.8	15.0	120	128

Table 6.2: Comparison between parameters and diagnostics of the flame properties in 1D.

This confirms that the higher the parameter β, the larger the flame thickness, the better the diagnostics, but the longer the response time of the system. So there is a balance to determine between speed, thickness and characteristic time. $\beta \in [0.8 - 1.0]$ appears as a reasonable choice with a response time shorter than 100s and a flame speed approximating $s_{L,KPP}$ with less than 10% error. For this range, the flame thickness satisfies $\delta_L \approx 8 - 10\Delta x$.

The progress variable c is represented in figure 6.8 at time $t = 800$ for different values of β so as to visualize the influence of the thickness on the sharpness and speed of the flame.

2D circular propagation

In a two-dimensional case, when the vegetal fuel distribution is isotropic, the flame front popagates at the same speed in all directions. So the fire front stays circular over time, and at any time step it is characterized

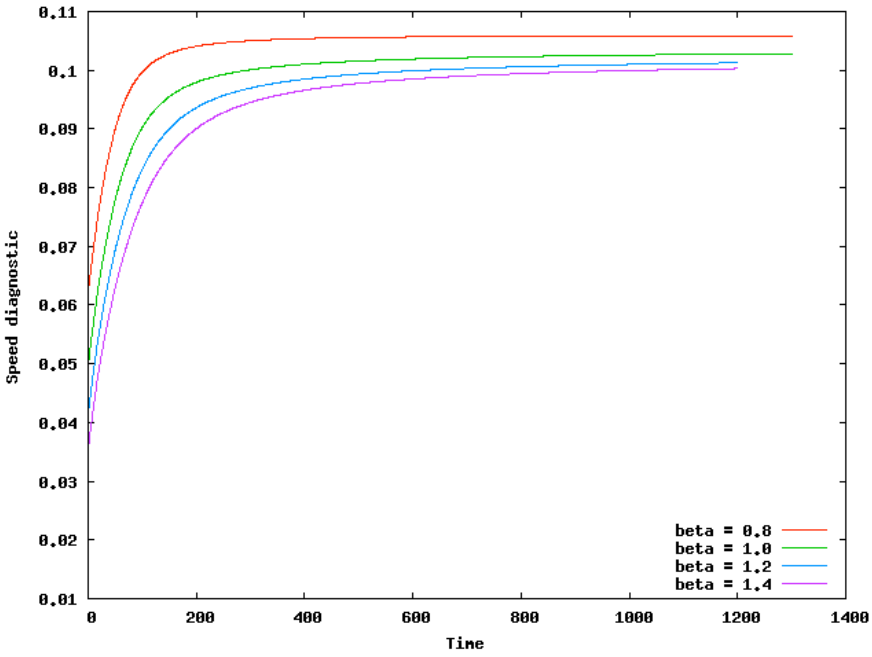

Figure 6.5: 1D diagnosed flame speed with β as parameter.

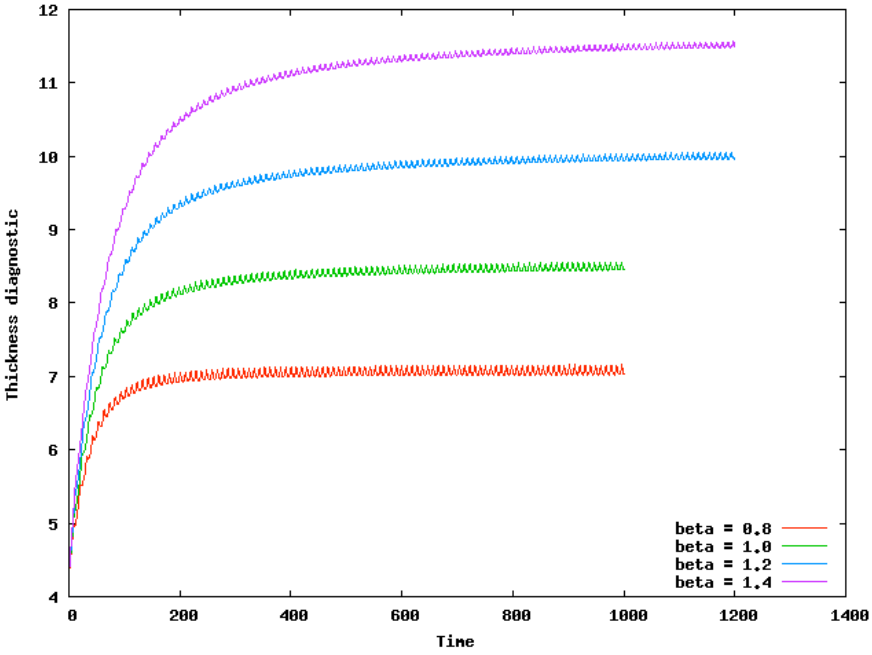

Figure 6.6: 1D diagnosed flame thickness with β as parameter.

by its radius r_f. The diagnostic of the flame speed $s_{L,d}$ is given by equation (6.18).

$$s_{L,d} = \frac{1}{2\pi r_f} \frac{d}{dt} \Big(\iint c(x,y)\, dx\, dy \Big) \tag{6.18}$$

The same model configuration is carried out as in the 1D validation. Results are presented in table 6.3. They show that the diagnostics are consistent with the parameters. $\beta \in [0.8 - 1.0]$ is also a good balance in 2D between accuracy of the speed and of the thickness, and the response time of the system.

So as to conclude, this new model with $s_{L,KPP}$ as parameter of the model behaves as expected from the KPP analysis, either in 1D or 2D. It can therefore be the basis of extensive studies when the fire rate of spread depends upon an anisotropic vegetation distribution.

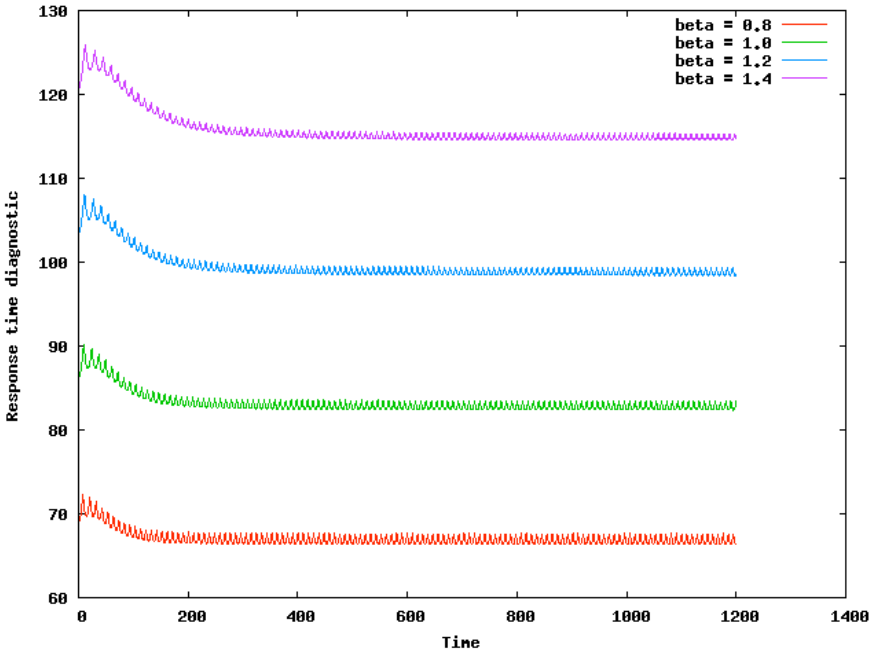

Figure 6.7: 1D diagnosed response time with β as parameter.

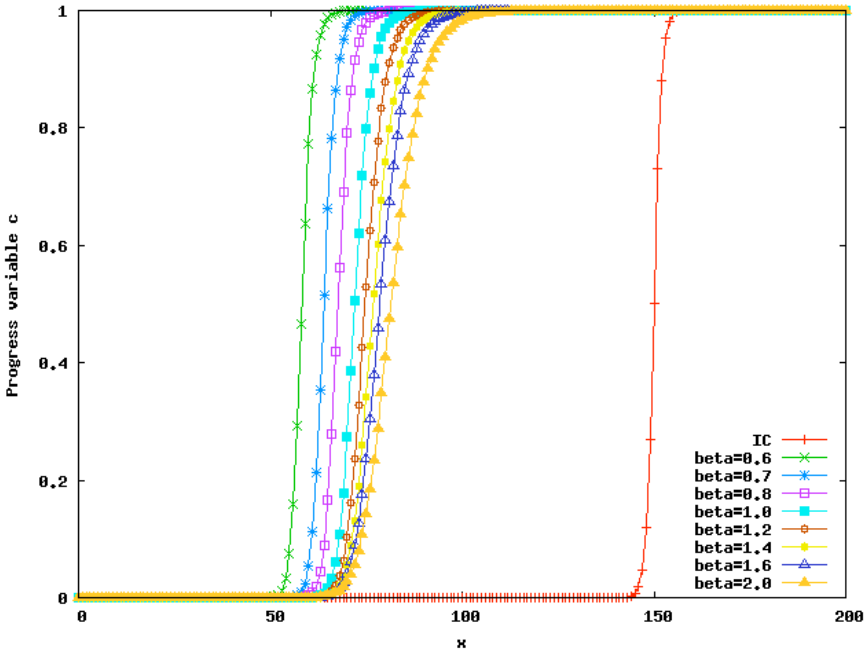

Figure 6.8: 1D Diagnosed response time with β as parameter.

β	$s_{L,KPP}$	$s_{L,d}$	δ_L/δ	$\delta_{L,d}/\delta$
0.6	0.1	0.1220	4.8	6.1
0.7	0.1	0.1125	6.4	6.6
0.8	0.1	0.1065	8	7.1
0.9	0.1	0.1020	9.6	7.7
1.0	0.1	0.0995	11.2	8.3

Table 6.3: Comparison between parameters and diagnostics of the flame properties in 2D.

6.2 Anisotropic vegetation distribution

6.2.1 Introduction of the vegetation dependence

The model in equation (6.10) shall be adapted for an anisotropic vegetation distribution to define a more realistic framework. In this study, the front rate of spread is assumed to depend linearly on the vegetation distribution, denoted by Y, with:

$$s_L(x,y) = s_{L,KPP}\, Y(x,y) \tag{6.19}$$

where $s_{L,KPP}$ is the constant of proportionality derived from the KPP analysis (if $Y = 1$ everywhere over the domain, the vegetal fuel is uniformly spread and therefore the speed parameter is the KPP value $s_{L,KPP}$).

6.2.2 1D fire propagation

Definition of the model parameter

In 1D, only a linear variation of the amount of fuel Y is considered along the x-axis, and $s_L(x) = s_{L,KPP}\, Y(x)$. In a preliminary step, the non-constant flame speed $s_L(x)$ is directly inserted into the PDE as the parameter of the model. Hence, considering a non-conservative form, the equation (6.9) becomes:

$$\frac{\partial c}{\partial t} = \Big(\frac{\beta s_L(x)\Delta x}{2}\Big)\frac{\partial^2 c}{\partial x^2} + \Big(\frac{s_L(x)}{2\beta\Delta x}\Big)\, c(1-c) \tag{6.20}$$

With a non-constant flame speed s_L, the flame speed diagnostics vary over time, depending on the local vegetal fuel present in the vicinity of the front at a given time. They read:

$$s_{L,d_1}(t) = \frac{d}{dt}\int_{x_{min}}^{x_{max}} c(x,t)\, dx \tag{6.21}$$

$$s_{L,d_2}(t) = \Big(\frac{1}{2\beta\Delta x}\Big)\int_{x_{min}}^{x_{max}} s_L(x)\, c(x,t)\, (1-c(x,t))\, dx \tag{6.22}$$

These two diagnostics shall approach the quantity $\bar{s}_L(t) = s_L(x_c(t)) = s_{L,KPP}\, Y(x_c(t))$, where $x_c(t)$ represents the position of the front at time t.

However, the model (6.20) does not satisfy these diagnostics as a high discrepancy can be denoted at each time step between the diagnosed simulated speed $s_{L,d}$ and the predicted value $\bar{s}_L(t)$, especially when the variations of Y along the x-axis are strong. For a high fuel gradient and an amount of fuel which increases in the direction of the front propagation (typically, $Y(x) = (0.2-1)/200\, x + 1$), this formulation leads to an acceleration of the flame speed and a thickening of the flame which cannot be controlled by the parameters of the model, as highlighted by figures 6.9 and 6.10. This flame thickening is explained by the variation of the velocity through the fire front due to the local variations of Y. If the amount of fuel increases while the front propagates, then the flame speed increases over time. It also means that at a given time, the cold side of the front (e.g., the side of the interface where the fresh vegetation is located, denoted by $c = 0^+$) moves faster than the hot side of the front (e.g., the side of the interface where the burnt vegetation is located, denoted by $c = 1^-$). In this case, the zone in which the reaction takes place widens, meaning that the flame thickness increases and that the reaction is enhanced. More heat is released and therefore the flame speed is higher than the predicted value.

The present model cannot handle a non-constant speed through the flame as it cannot solve properly the physics at the flame scale without considering the turbulence. The approximation is only valid if the vegetal fuel gradient is relatively small (typically, $Y(x) = (0.9-1)/200\, x + 1$); in this configuration, the diagnosed speed follows the same trend as the predicted speed $\bar{s}_L$. However, the model shall work for any vegetation field. So it shall be adapted to keep a quasi-stationary approach and simulate the fire propagation at a macroscopic scale. For this purpose, a spatial filtering is implemented: at each time step t, the speed model parameter is given by $\bar{s}_L$ which is constant over the spatial domain and which is defined as $\bar{s}_L(t) = s_L(x_c(t))$ (x_c representing the front position at the associated time step such that $c(x_c) = 0.5$. This spatial filtering is schematized in figure 6.11.

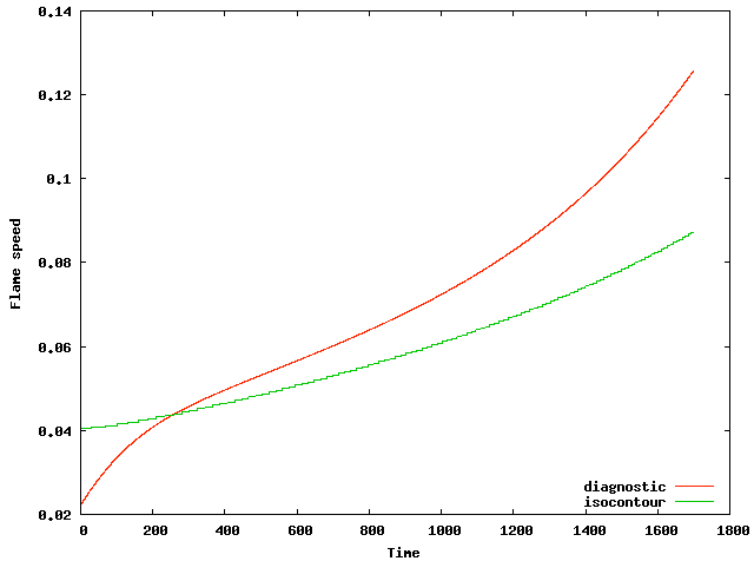

Figure 6.9: Comparison over time of s_{L,d_1} and $\bar{s}_L$ for the model (6.20)

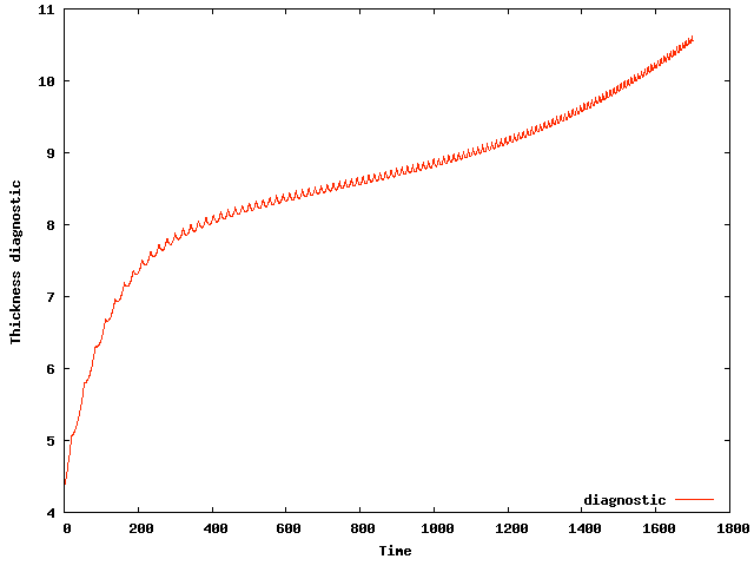

Figure 6.10: Diagnosed flame thickness over time for the model (6.20).

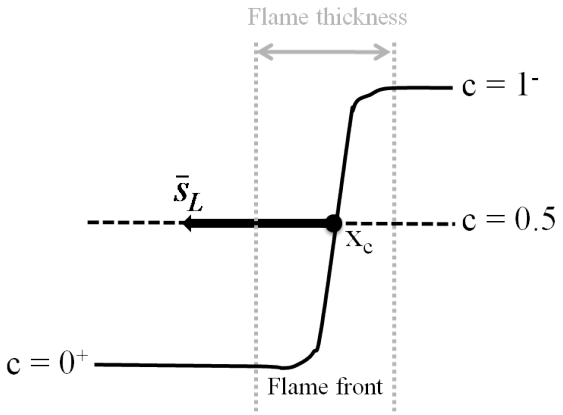

Figure 6.11: Schematic representation of the fire front at a given time.

The new model with the vegetation dependence is given by:

$$\frac{\partial c}{\partial t} = \left(\frac{\beta\, \bar{s}_L\, \Delta x}{2}\right) \frac{\partial^2 c}{\partial x^2} + \left(\frac{\bar{s}_L}{2\beta\Delta x}\right) c(1-c), \tag{6.23}$$

with $\bar{s}_L = s_L(x_c) = s_{L,KPP}\, Y(x_c)$.

Validation

High fuel gradient

The model (6.23) is tested for the same vegetation configuration than the model (6.20), that is to say for a strong variation of the amount of vegetal fuel along the x-axis ($Y(x) = (0.2-1)/200\, x + 1$), with the following parameters: $s_{L,KPP} = 0.1$ and $\beta = 0.9$.

As the fuel load increases when the front propagates, the flame speed increases as figure (6.12) shows. Furthermore, this new formulation guarantees a constant flame thickness once the quasi-stationary regime is reached, with $\delta_{L,d}/\Delta x \approx 8$ in figure 6.13. As the flame thickness is constant, the flame speed is better controlled: figure 6.14 shows indeed that both speed diagnostics s_{L,d_1} and s_{L,d_2} follow the same trend as the predicted speed $\bar{s}_L$.

The gap between the diagnostics and the model parameter is due to the numerical parameter β. Indeed, for $\beta = 1.2$, the gap is drastically reduced as figure 6.15 testifies. $\beta = 1.2$ gives indeed a better approximation of $s_{L,KPP} = 0.1$ and captures better the sharp front as the thickness is higher.

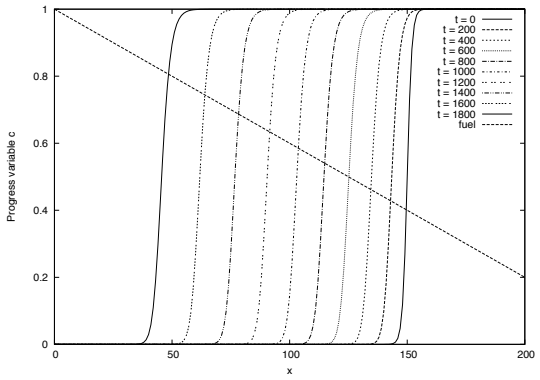

Figure 6.12: Profile of c over time for $\beta = 0.9$.

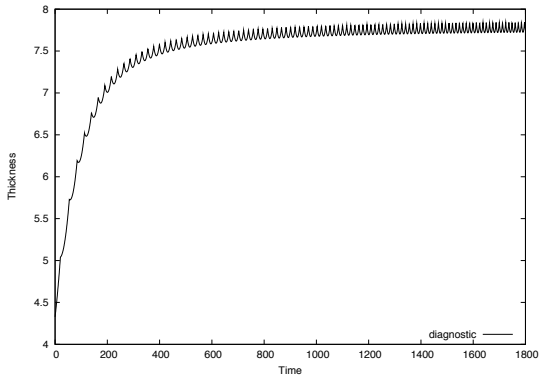

Figure 6.13: Diagnosed flame thickness for $\beta = 0.9$.

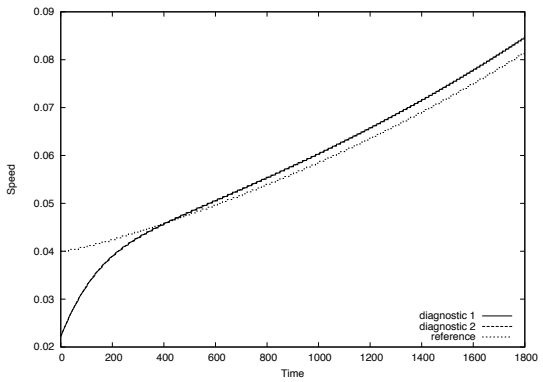

Figure 6.14: Diagnosed flame speed for $\beta = 0.9$.

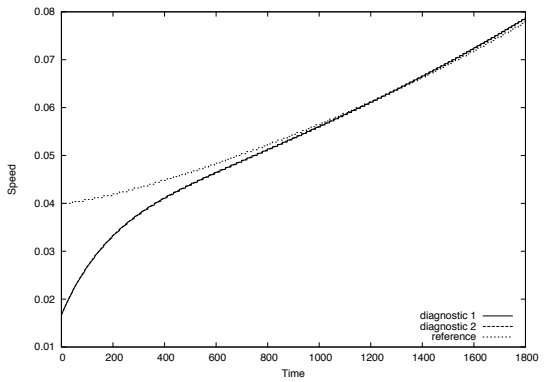

Figure 6.15: Diagnosed flame speed for $\beta = 1.2$.

Critical condition of vegetation

This model must be able to handle drastic variations of the amount of fuel as in reality an homogeneous region, like a forest, could be crossed by a road or a lake, which acts as a break to the fire propagation and which corresponds to a zero fuel load. The idea is therefore to check the robustness of the model when the fire front encounters a fuel break. Figure 6.16 shows the profile of the progress variable c over time when $Y = 0$ at $x = 100$. It appears that the flame speed reduces drastically when approaching $x = 100$. As expected, it acts as a fuel break: the flame cannot propagate further. In reality, the fire might be able to propagate further if the width of the fuel break is relatively small due to a phenomenon called fire spotting. Here the model is able to handle this critical condition of the vegetation as the diagnosed speeds follow the same slope as the reference $\bar{s}_L$.

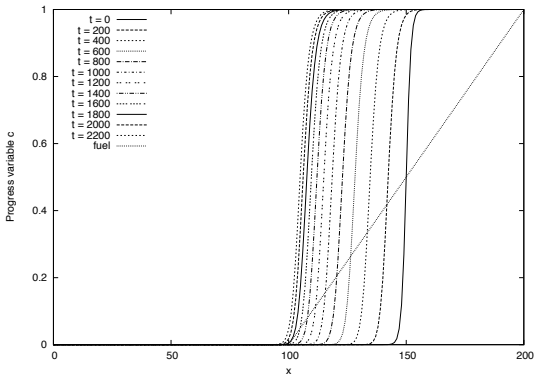

Figure 6.16: Profile of c with a fuel break at $x = 100$.

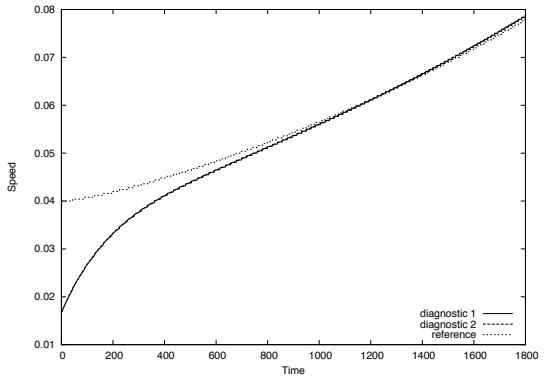

Figure 6.17: Diagnosed flame speed.

So the spatial filtering appears as a valuable solution to avoid a variation of s_L within the flame and to define a model with a rate of spread dependent on the vegetal fuel load. The next step is to generalize this technique to a 2D surface fire propagation.

6.2.3 2D generalization

The objective is to generalize this spatial filtering for the two-dimensional case when the fire propagates over a surface where the vegetation may be randomly distributed. As for the one-dimensional case, this supposes that a vegetation mapping Y is available and that the fire rate of spread is parametrized in terms of Y. In this work, it is assumed that the field s_L depends linearly upon the local amount of fuel such that $s_L(x, y) = s_{L,KPP}\, Y(x, y)$.

Principles

The spatial filtering needs to be introduced in the PDE of the progress variable c so as to avoid a significant variation of the speed within the flame thickness. In this context, the challenge is that the fire may propagate in very different directions depending on the fuel distribution, and not only in one direction like in 1D.

When propagating over a 2D domain, the fire front may split into multiple heads moving at different speeds due to the heterogeneous vegetation conditions. From the observation analysis, it is known that the fire dynamics, at a given time, is confined in the vicinity of the fire front, e.g. in the vicinity of the isocontour $c = 0.5$ where the reaction is significant. The idea is therefore to apply the 1D technique to each direction of propagation, assumed to be normal to the isocontours of the progress variable c. This means that each point close to the front shall be associated to one direction of propagation, along which a constant rate of spread is imposed. This constant speed in one direction of propagation is given by $\bar{s}_L = s_L(x_c, y_c) = s_{L,KPP}\, Y(x_c, y_c)$, where (x_c, y_c) is the estimated location of the intersection between the isocontour $c = 0.5$ and this direction of propagation.

With this technique, the velocity field $s_L(x,y)$ is corrected at each time step of the model integration by imposing a constant speed in each direction of propagation. This ensures a quasi-stationary approach and the resolution of the fire phenomenon at a relevant macroscopic scale. As for the 1D configuration, the model can be validated by comparing the reference flame speed (averaged along the front $c = 0.5$)

$$\bar{s}_L^* = \frac{\int_{c=0.5} s_L \, dS}{\int_{c=0.5} dS} \tag{6.24}$$

to the diagnosed flame speed

$$s_{L,d} = \frac{1}{\int_{c=0.5} dS} \frac{d}{dt}\Big(\iint c(x,y)\, dx\, dy \Big) = \frac{1}{\int_{c=0.5} dS} \iint \Big(\frac{s_L(x,y)\, c(x,y)(1-c(x,y))}{2\beta\delta} \Big)\, dx\, dy \tag{6.25}$$

Algorithm for spatial filtering

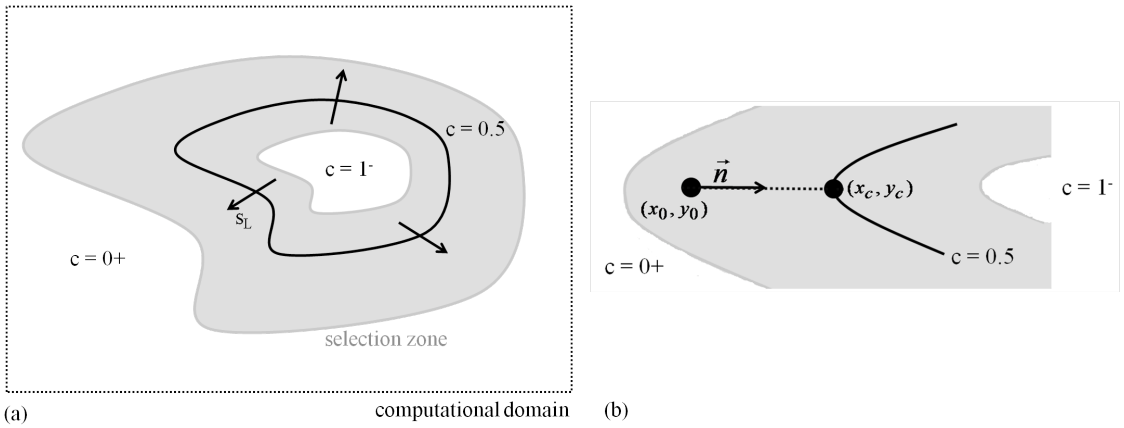

Figure 6.18: Schematic representation of the 2D spatial filtering (a) Selection zone (b) Zoom on the selection zone with point projection and spatial filtering.

The implementation of the 2D spatial filtering follows this series of steps at each time step of the model integration, illustrated in figure 6.18:

1. Discretization of the isocontour $c = 0.5$ defining the position of the front.
2. Estimation of the average speed of the front $\bar{s}_L^*$ (for comparison with diagnostics):
   - Estimation of the circonference of the isocontour $\int_{c=0.5} dS$.
   - Estimation of the mean value of the rate of spread along the isocontour $\int_{c=0.5} s_L \, dS$.
   - Deduction of $\bar{s}_L^*$.
3. Selection of the points which are sufficiently close to the front to have an effect on the system dynamics at the given time step (these points belong in general to the total flame thickness δ_L^t, corresponding to the zone over which the progress variable c changes from 0.01 to 0.99).
4. Projection for each selected point onto the isocontour $c = 0.5$:
   - Identification of the position of the point (x_0, y_0) and of its associated value of c.
   - Translation of the point (x_0, y_0) in the normal direction towards the isocontour $c = 0.5$ (until finding two points enclosing this isocontour along the normal direction).
   - Determination of the position of the point (x_c, y_c) on the isocontour $c = 0.5$ in this normal direction (by linear interpolation).

- Determination of the speed $\bar{s}_L$ associated to the isocontour point (x_c, y_c).
- Correction of the velocity field at the point (x_0, y_0) by changing the default value $s_L(x_0, y_0)$ by $s_L(x_c, y_c)$.

5. Integration of the PDE with the corrected velocity field $\bar{s}_L(x, y)$ as parameter of the model.

Validation

The spatial filtering technique aims at determining the instantaneous rate of spread of the fire front in one direction of propagation. The 1D algorithm is straightforward as there is a unique direction of propagation, while some errors are introduced in 2D by the projection technique. Indeed, the vegetal fuel distribution ahead of the fire front has a direct influence on the rate of spread, so the further the point to be projected (x_0, y_0), the more approximative the trajectory of this point towards (x_c, y_c). (x_0, y_0) is projected in the normal direction, computed locally as the normal to the isocontours of c. But these isocontours might be slightly different when the fire front is close to (x_0, y_0) further in time. However, this approximation is expected to be relatively good as the zone to cover to correct the velocity field is reduced to the total thickness: only the points which have a impact on the fire dynamics at a given time are considered for this projection.

So as to check the quality of the 2D spatial filtering, the algorithm is firstly applied to the one-dimensional configuration with a plane front moving along the x-direction from the hot gas to the fresh gas. So the results will be compare to the 1D spatial filtering (presented in section 6.2.2).

1D vegetation distribution

The two-dimensional spatial filtering algorithm is tested by simulating the 1D configuration with a plane front located initially at $x_c = 150$ for all y and moving along the x-direction towards the fresh gas. The vegetation distribution is also linear, increasing from $y = 0.2$ at $x = 200$ to $Y = 1$ at $x = 0$, and is constant along the y-direction. It corresponds to $Y(x) = (0.2-1)/200\,x + 1$ as in the 1D validation study. The model is integrated from $t = 0$ to $t = 800$s for the following parameters: $s_{L,KPP} = 0.1$ and $\beta = 0.9$.

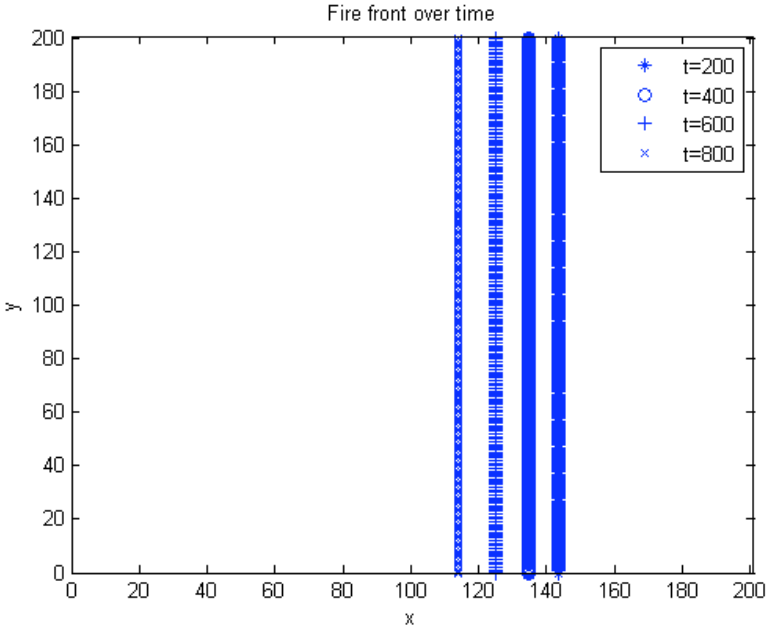

Figure 6.19: Evolution of the fire front position over time.

Figure 6.19 indicates the position of the fire front (identified as the isocontour $c = 0.5$) at $t = 200$, $t = 400$, $t = 600$ and $t = 800$. As expected from the vegetal fuel field and the initial condition of the progress variable, the front moves from right to left, from the burnt gas to the fresh gas.

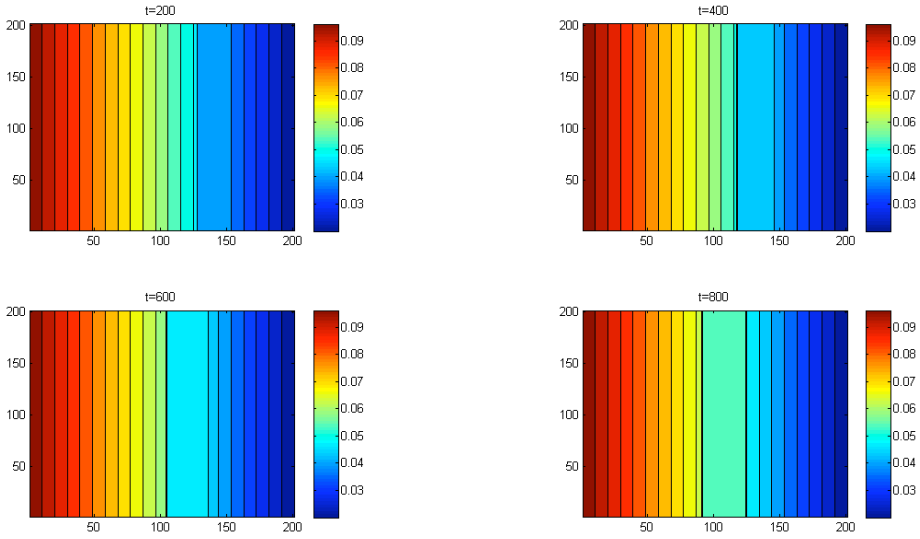

Figure 6.20: Corrected velocity field at 4 different times of the integration.

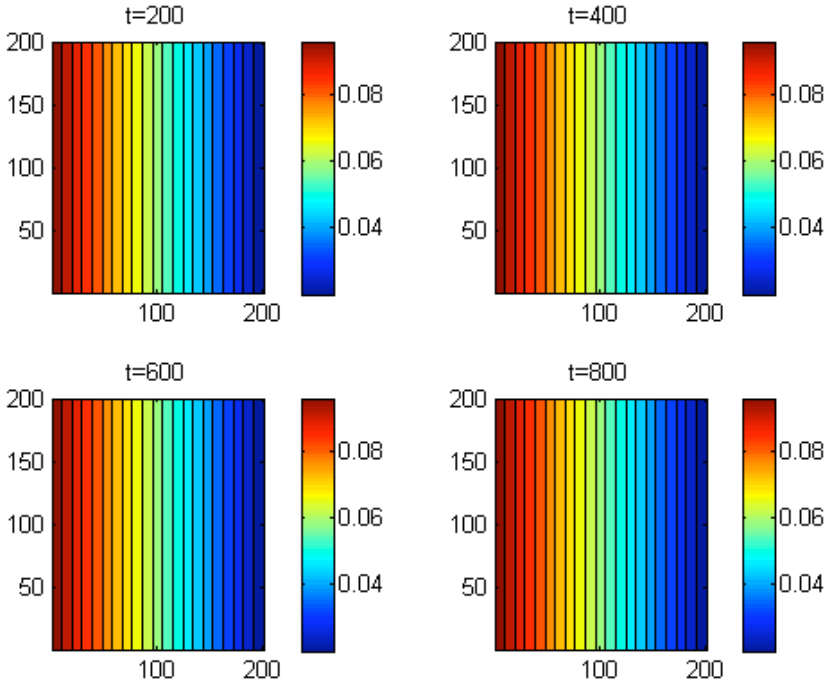

Figure 6.21: Velocity field at 4 different times of the integration without spatial filtering.

As to figure 6.20, it represents the velocity field once the spatial filtering is applied for these different times of the assimilation window. In each subfigure, there is one widener band of one colour. This corresponds to the zone where the projection is applied, in other words to the total thickness of the front. This can be compared with the velocity field if there were no spatial filtering applied, in figure 6.21.
So at one given time the front position given in figure 6.19 is located more or less in the middle of this unicolour widener band. This means that the selected points located on one side or the other of the fire front, at a given time, are projected onto the isocontour $c = 0.5$ and are therefore associated with the speed of this isocontour, denoted by $\bar{s}_L$. This behavior is consistent with the algorithm described previously.

Figure 6.22 shows that the speed diagnostic gives the same result as for the 1D algorithm (presented in

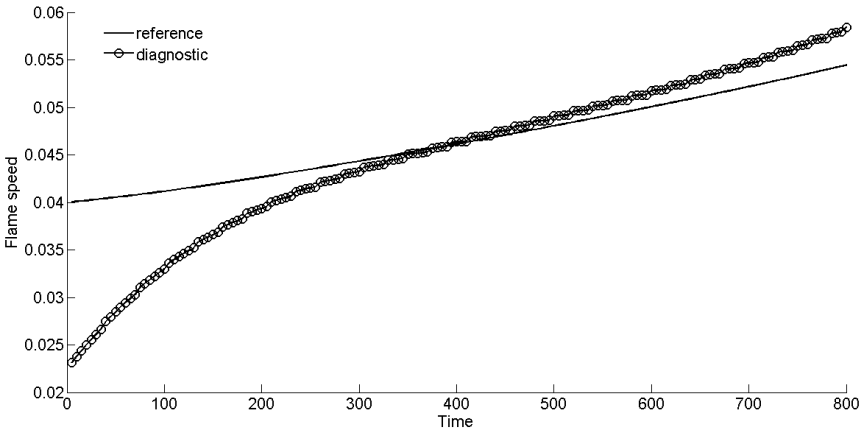

Figure 6.22: Comparison of the speed diagnostic $s_{L,d}$ to the reference flame speed $\bar{s}_L^*$ over time, using the 2D spatial filtering algorithm.

figure 6.14) for the corresponding time interval $[0; 800]$. Also, as for the 1D case, the gap between the speed diagnostic and the reference is reduced when the numerical parameter β is increased.

These results show that the 2D spatial filtering technique is able to reproduce the same speed profile over time as the 1D for this fire configuration. This study will now be extended to a 2D fire configuration.

2D vegetation distribution

In a 2D fire configuration, the initial fire is set as a circular flame of radius 5 at the centre of the square domain. The behavior of the model with the spatial filtering will be presented for the time interval [0; 800] and for two different vegetation distributions:

1. a 1D plane distribution corresponding to $Y(x, y) = \frac{(0.2-1)}{200}\, x + 1$,
2. an elliptical Gaussian distribution with

$$Y(x, y) = \exp\Big(\frac{(x-100)^2}{2\sigma_x^2} + \frac{(y-100)^2}{2\sigma_y^2}\Big)$$

which has the shape of a bell curve which reaches $Y = 1$ at the centre of the peak $(100, 100)$ and which quickly falls off towards 0 when going away from this peak. The width of the bell is controlled by the parameters σ_x and σ_y. So as to get an elliptical shape, σ_x and σ_y are not equal. In this study, $\sigma_x = 20$ and $\sigma_y = 40$.

In the first vegetation configuration, the initial circular fire front tends to spread in the x-direction towards the left side of the domain where the vegetation reaches its maximum intensity. This is highlighted by the evolution of the fire front position over time in figure 6.23. The velocity field is corrected at each time step, figure 6.24 presents this field at $t = 200$, $t = 400$, $t = 600$ and $t = 800$. The zone where the spatial filtering is applied is circular at the beginning, but its shape is more elliptical at the end of the assimilation window due to the preferential direction of the propagation. Furthermore, the magnitude of the filtered speed indicates clearly that the rate of spread is much faster in the left side of the domain (orange zone) than in the right side (blue zone).

The diagnostics of the flame thickness (averaged along the iscontour $c = 0.5$) in figure 6.25 shows that the increase of the thickness of the front is significantly reduced with the application of the spatial filtering algorithm. With the correction of the velocity field, the thickness is not constant but remains controlled. As to the speed property, figure 6.26 superposes the diagnostic $s_{L,d}$ and the reference $\bar{s}_L^*$ for both corrected and non-corrected velocity field. It appears that the gap between the diagnostic and the reference is much thinner with the spatial filtering. Even though the correction is not perfect as in the 1D configuration, the acceleration of the front is more controlled and is suitable for this study.

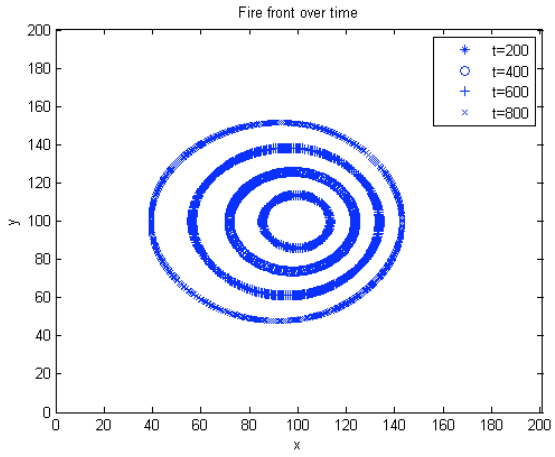

Figure 6.23: Evolution of the elliptical fire front position over time.

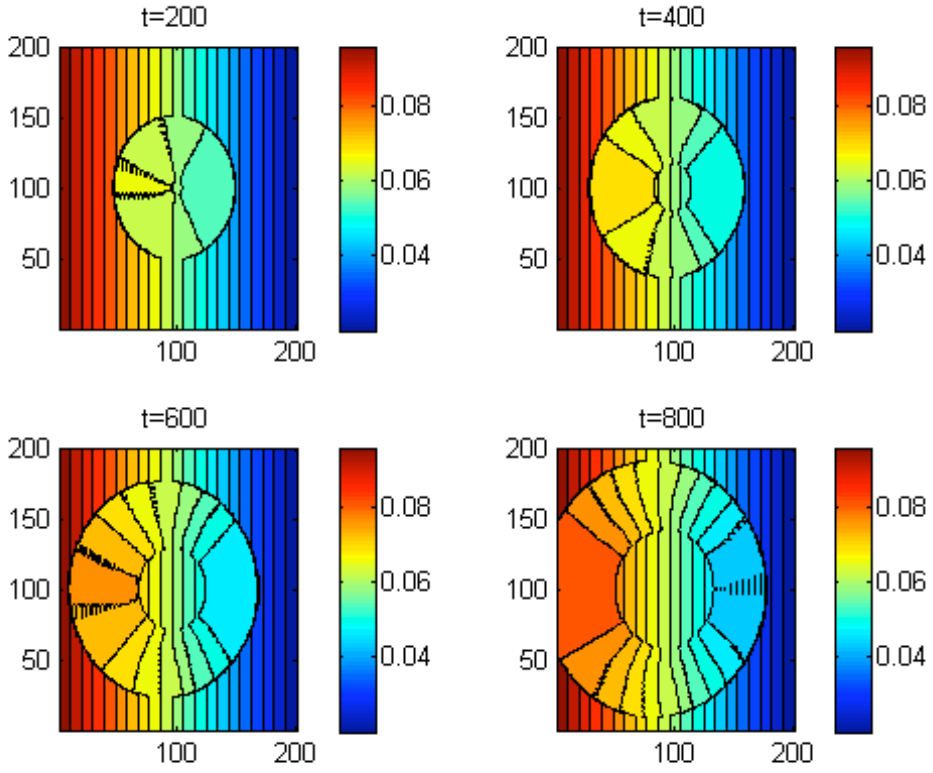

Figure 6.24: Corrected velocity field at 4 different times of the integration.

With the second vegetation configuration, the spatial filtering algorithm is tested when the rate of spread decreases over time. Indeed, the amount of fuel is high in the vicinity of the initial front position, but decreases rapidly when the front propagates. As $\sigma_y > \sigma_x$, the vegetation is spread further in the y-direction than in the x-direction. Thus, the front will tend to propagate more in the y-direction. This is visible in figure 6.27. Due to the bell shape of Y and of the rapid decrease of the amount of the fuel, the propagation is almost stopped in the x-direction.

The correction of the velocity field due to the spatial filtering can be observed by comparing figures 6.28 and 6.29. It appears that the magnitude of the front rate of spread is significantly reduced in the course of its propagation, from 0.08 at $t = 200$ to 0.03 at $t = 800$. This is confirmed by the diagnostics of the flame properties.

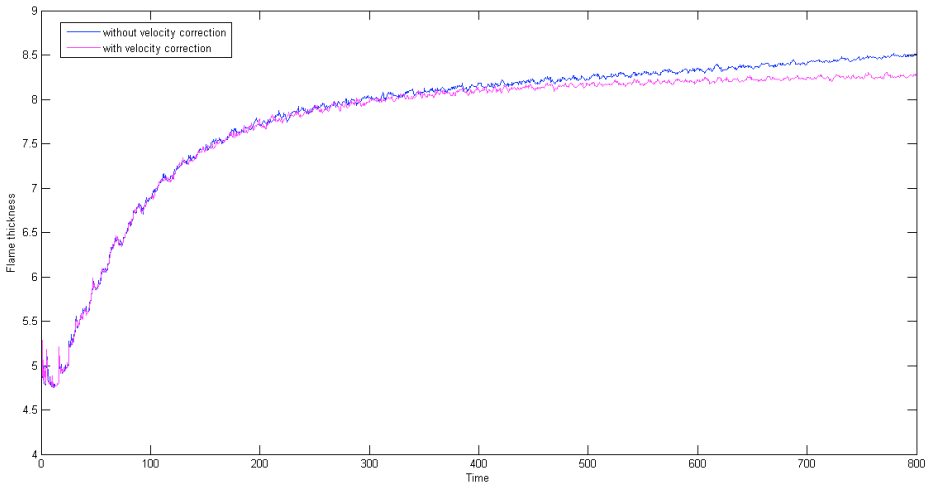

Figure 6.25: Comparison of the flame thickness diagnostic - Model with (magenta line) / without (blue line) spatial filtering.

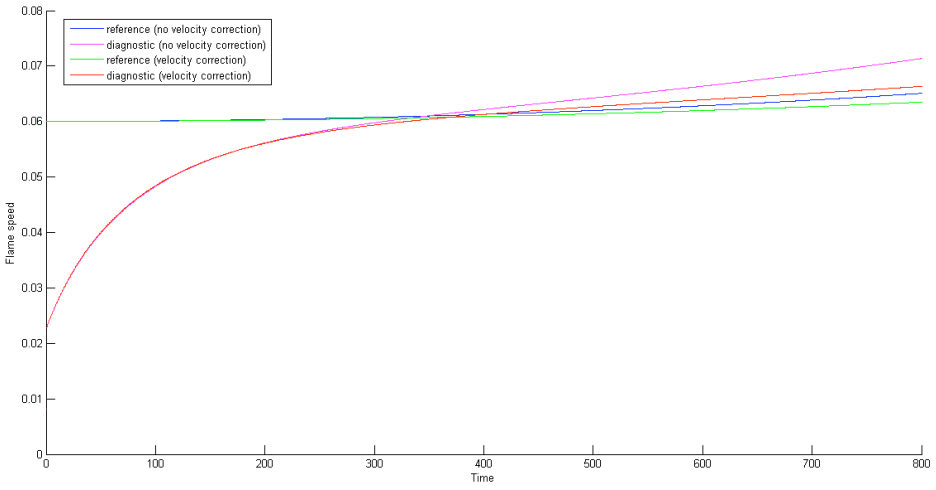

Figure 6.26: Comparison of the flame speed diagnostics to the reference $\bar{s}_L^*$ - Model with spatial filtering (red line for diagnostic and green line for reference) and model without spatial filtering (magenta line for diagnostic and blue line for reference).

Figures 6.30 and 6.31 compare the evolution of the flame thickness over time when the spatial filtering is applied or not respectively. While the flame thickness decreases significantly when there is no spatial filtering applied during the model integration, it reaches a constant value, consistent with the previous simulations ($\delta_L \approx 8\delta$), at some time of the integration. This means that the propagation is due to the propagation and not to an increase of the width of the reaction zone, implying an increase of the heat release while the amount of fuel does not change. As to the speed, the gap between the diagnostic $s_{L,d}$ and the reference $\bar{s}_L^*$ is significantly reduced when the spatial filtering is applied in figure 6.32 (compared to the gap when no spatial filtering is applied in figure 6.33).

The consistency of these diagnostics with the input data was expected with the implementation of the spatial filtering for a 2D fire configuration. These results for different vegetation distributions prove that the algorithm works properly and provides a valuable framework to apply data assimilation to the fire model, which is summarized in the following section.

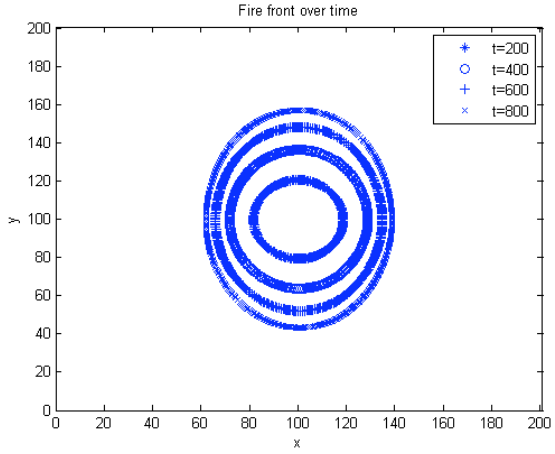

Figure 6.27: Evolution of the elliptical fire front position over time.

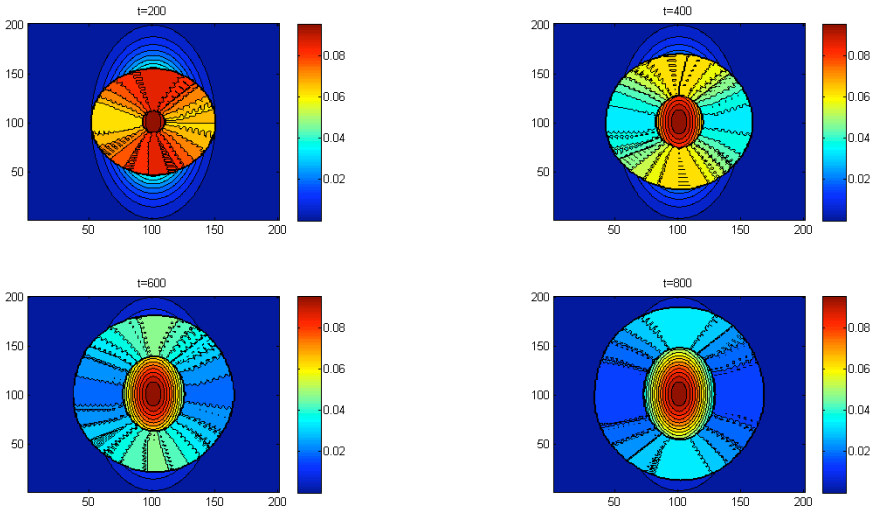

Figure 6.28: Corrected velocity field at 4 different times of the integration.

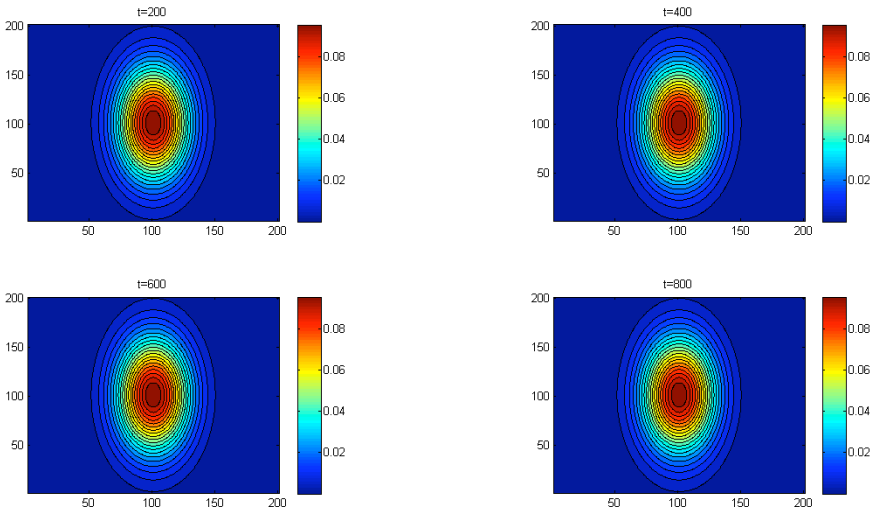

Figure 6.29: Velocity field at 4 different times of the integration without spatial filtering.

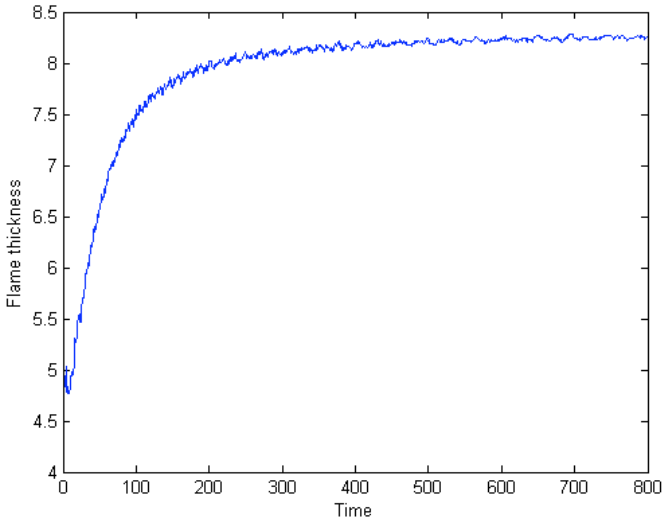

Figure 6.30: Diagnostic of the flame thickness over time for the model with spatial filtering.

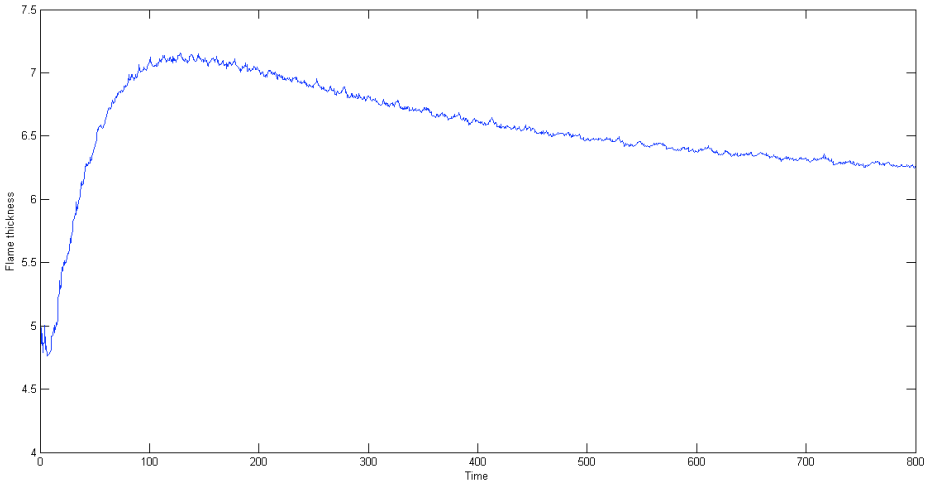

Figure 6.31: Diagnostic of the flame thickness over time for the model without spatial filtering.

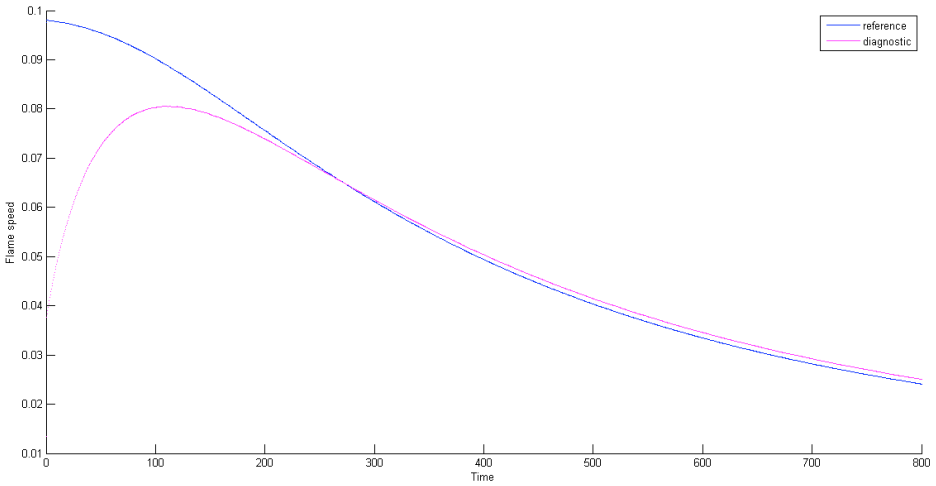

Figure 6.32: Comparison of the flame speed diagnostic to the reference $\bar{s}_L^*$ over time for the model with spatial filtering.

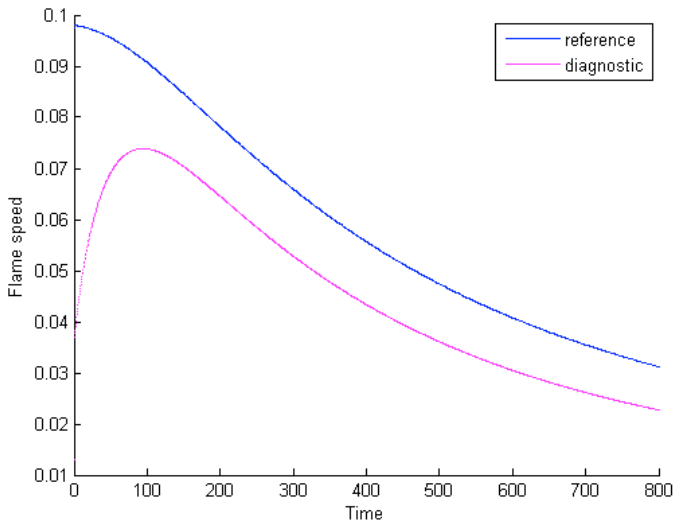

Figure 6.33: Comparison of the flame speed diagnostic to the reference $\bar{s}_L^*$ over time for the model without spatial filtering.

6.3 Model formulation

The 2D fire propagation is modeled by a single PDE with the progress variable c as state variable:

$$\frac{\partial c}{\partial t} = \Big(\frac{\beta\,\delta\,\bar{s}_L}{2}\Big)\Delta c + \Big(\frac{\bar{s}_L}{2\,\beta\,\delta}\Big)c(1-c) \tag{6.26}$$

with:

- c: the progress variable satisfying $0 < c < 1$, with $c = 1^-$ representing the burnt region and $c = 0^+$ the unburnt region,
- Y: the fuel mass fraction (the relative amount of fuel remaining) satisfying $0 < Y < 1$,
- $\bar{s}_L$: the rate of spread after the spatial filtering of the local rate of spread s_L,
- s_L: the local rate of spread assumed to depend linearly on Y such that $s_L(x,y) = s_{L,KPP}\,Y(x,y)$, with $s_{L,KPP}$ the constant of proportionality,
- β: the thickness numerical parameter with $\beta = O(1/2)$,
- δ: the grid stepsize with $\delta = \min(\Delta x, \Delta y)$.

This model represents the propagation of a front, assimilated to a very strong gradient of the progress variable c (the front is typically localized along the isocontour $c = 0.5$), from the burnt region to the surrounding fresh environment. As for the premixed combustion model, the pyrolysis is not modeled and the transformation from solid to gas is supposed to occur infinitely fast when the fire front approaches. The vegetation distribution Y can be of any type, for instance linear, Gaussian or random. As to the initial condition, the model sets an initial circular flame of a fixed radius at the centre of the domain.

This spatial filtering technique appears as a powerful tool to study the propagation of a flame front at a macroscopic scale taking into account the effects of a non-uniform vegetation distribution. The uncertainty in the formulation of the model or in the parameters of the model could then be reduced using data assimilation, as it will be demonstrated in the following.

Conclusion

In the literature, it has been shown that the wildfire rate of spread depends on a combination of factors, primarily a combination of fuel characteristics, weather conditions and local topography effects [22]. In this preliminary work, two models have been built so as to focus on the effect of the vegetation, while Jan Mandel's model assimilates the impact of the wind and the initial position of the fire.

The premixed combustion model presents how the temperature field is affected by a random fuel distribution. It has been observed that the head of the fire splits into multiple parts, each part propagating at a specific speed, depending on the local conditions of vegetation. Indeed, the fire moves towards the fuel pockets, while it stops when encountering non-burnable regions. Reaction cannot take place any longer as there is no supply of fuel in these areas, instead diffusion is predominant and enhances the decrease of the temperature at the flame centre. While this model does not provide a precise diagnosis of the rate of spread in 2D, it is able to give a general picture of the evolution of the temperature as a function of the diffusion and reaction coefficients, and is suitable to establish the basic diagnostics associated with data assimilation. This model will indeed be the basis of data assimilation experiments in terms of observations and control parameters.

However, this project leads to the assimilation of the parameterized front rate of spread as it is recognized as the main feature of the flame. So a new model has been built with the progress variable c as single state variable. This model characterizes the propagation of an interface from the burnt region to the unburnt areas, in terms of speed and thickness, at a macroscopic scale. The rate of spread has been introduced as a model parameter by generalizing the basic results of the KPP analysis, so the model is able to track the propagation of a two-dimensional flame for any type of fuel distribution and to provide precise diagnostics of its properties over time. This 2D wildfire propagation model will be helpful to define the assimilation of the speed parameter(s), which is the long-term objective of this project.

Part III

Calibration of Fire Model Parameters

7. Diffusion Parameter Calibration

This initial approach of data assimilation holds on the research carried out by Jan Mandel [13], using the premixed combustion model, which controls the evolution of two state variables, the temperature θ and the fuel load Y. Here one single parameter is calibrated, the diffusion coefficient D, using observations of the temperature fields at fixed grid points, so as to introduce the tools associated with data assimilation and useful to ensure the optimality of the analysis. This strategy allows to describe a more complete physics of the fire phenomenon, leading to a better understanding of the factors enhancing the propagation of the fireline, often empirically defined in front tracking models.

7.1 Validation of the assimilation prototype

With D as single control component, the control space is of dimension 1. As to the observations, only the temperature field θ is observed. This approach assumes that in situ and remote sensors are available to measure temperatures over time in practice. For this preliminary prototype, no noise is introduced to the observations. Consequently, the temperature measurements are directly extracted from the true trajectory at a fixed space and time frequency, so as to form the observation vector $\mathbf{Y}^o$. As for the 1D sample assimilation, each observation is supposed to have an independent error, $\mathbf{R}$ is a diagonal matrix. Their variance is equal to a percentage of the mean value of the true temperature field, denoted α_o.

In the course of data assimilation, the model trajectory is determined at least three times (background, true, analysis) with a different diffusion coefficient D, while the mesh size does not change. So the RK4 stability condition may be overcome at one point if D_b and D_t are not chosen carefully. To avoid this problem, Δt is chosen so as to satisfy the stability condition in the worst conceivable case. Hence, $\Delta t < 1/D_{max}$ if D_{max} represents the maximum value of the diffusion coefficient.

Once the assimilation algorithm is implemented, a first validation of this prototype consists in prescribing a high confidence in the background, and in ensuring that the analysis is close to the background. Note that for this validation step the model represents a gaseous flame ($k = 1$)[1]. Furthermore, $D_b = 0.3$, $D_t = 0.5$, $\alpha_o = 0.5$ ($\epsilon^o = 5.21 \times 10^{-4}$). Temperature measurements are taken each two grid points and each two time steps. The analysis is studied with the background uncertainty as parameter, α_b representing the percentage of the perturbation in the true diffusion coefficient D_t. As this prototype does not define rigorous OSE ($\mathbf{B}$ is not consistent with the definition of D_b), the background D_b does not change during the series of experiments. Results are presented in table 7.1.

α_b	ϵ^b	D_a	RMS(BMO)	RMS(AMO)
1×10^{-6}	9×10^{-14}	0.300	2.849×10^{-2}	2.849×10^{-2}
1×10^{-4}	9×10^{-10}	0.307	2.849×10^{-2}	2.746×10^{-2}
1×10^{-2}	9×10^{-6}	0.4754	2.849×10^{-2}	3.381×10^{-3}
5×10^{-2}	2.25×10^{-4}	0.4758	2.849×10^{-2}	3.324×10^{-3}
1×10^{-1}	9×10^{-4}	0.4758	2.849×10^{-2}	3.324×10^{-3}

Table 7.1: Analysis as a function of the background uncertainty σ_b^2.

The analysis gives an intermediate state between the background state and the true state. The following series of figures shows the reduced temperature and the reduced fuel mass fraction fields at $t = 100$, obtained for $D_b = 0.05$, $D_t = 0.6$, $\alpha_o = 0.5$ and $\alpha_b = 0.01$, and resulting in $D_a = 0.25$.

[1] k : Lewis number defined as the ratio of thermal diffusivity to chemical diffusivity, in equations (5.12) and (5.13).

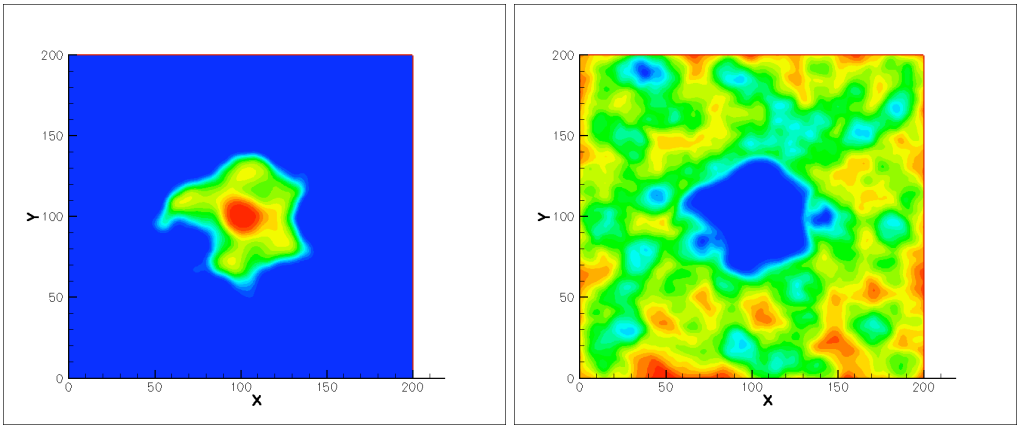

(a) Temperature field (b) Vegetal fuel field

Figure 7.1: Background state.

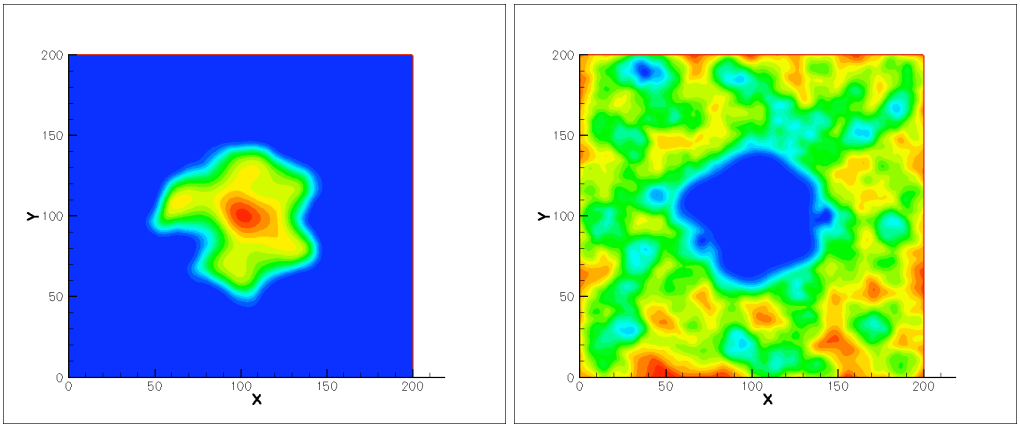

(a) Temperature field (b) Vegetal fuel field

Figure 7.2: Analysed state.

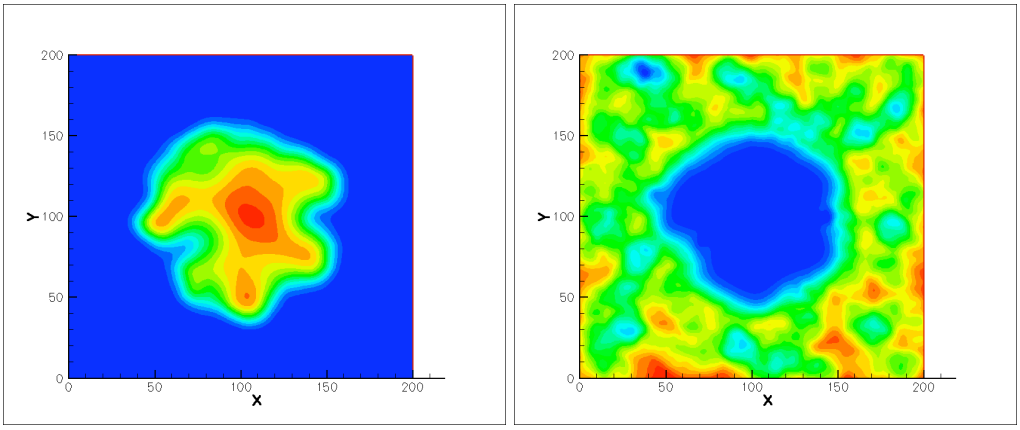

(a) Temperature field (b) Vegetal fuel field

Figure 7.3: True state.

As expected the analysis is closer to the observations than to the background in average with RMS(AMO) < RMS(BMO) for all cases. This is highlighted by the representation of the normalized Gaussian PDF of these different errors in figure 7.4: the uncertainty is much lower for the analysis than for the background and the observations as the Gaussian function is much thinner for the analysis. Equivalently, $\epsilon^a < \epsilon^o$ and $\epsilon^a < \epsilon^b$. So the analysis provides a parameter which is granted a higher confidence than both background and true control parameters. It defines therefore a more accurate state of the system once the model is integrated

with the analysis as parameter of the model.

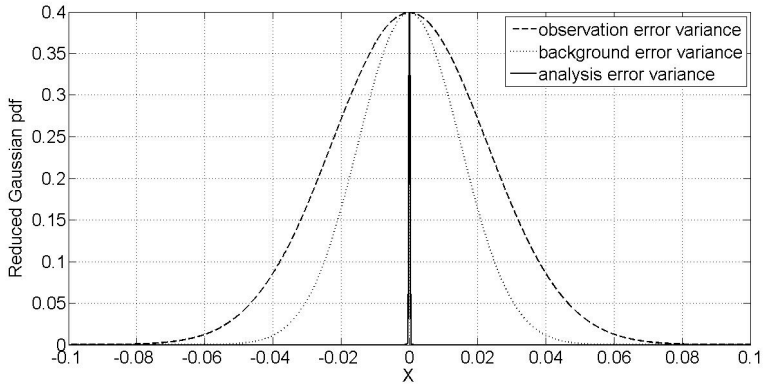

Figure 7.4: Normalized PDF of the observation/background/analysed errors in the experiment $\alpha_b = 0.05$.

From these results it appears that the transition between an analysis close to the observations and an analysis close to the background is very fast. When the confidence in the background is predominant ($\alpha_b \leq 1 \times 10^{-4}$), then the analysis converges towards D_b. However, it is closer to D_t even if there is a ratio of 100 between ϵ^b and ϵ^o. This is due to the number of observations taken into account, while there is a single control parameter to calibrate: even if the confidence in the background is high, observations still have a significant weight in the optimization problem due to their number.

7.2 Analysis sensitivity to observations

The number of observations and their respective position in space and time have a strong influence in the assimilation as it can give more or less weight to the observations, independently from the prescribed observation and background errors. Is there a threshold from which the analysis does not change if the number of the observations increases? What is the contribution of the observations to the analysis? Such questions are the subject of this investigation.

7.2.1 Combination of sets of observations

In the context of a real fire, observations can be recorded on the ground by the firefighters as well as from airplanes and satellites. This motivates the implementation of three different sets of observations from which new information on the fire system may be extracted:

- in situ observations (*ins*): spread over the whole domain with a prescribed space frequency (figure 7.5), the temperature measurements are taken at each observational time, so that there are multiple observations at a same grid position over an assimilation window.

- geostationary observations (*geo*): a satellite may only cover a part of the domain subject to a fire, then it provides observations in this reduced zone with a certain space and time frequency as for the in situ observations. In this work, the reduced zone corresponds to the left bottom corner of the square domain as represented in figure 7.6.

- observations from a low-orbit-satellite (*sat*): a satellite, whose altitude is lower than 1000km, does not cover the same zone over time, it provides instead observations on a trail which changes at each time it goes over the region. One trail corresponds to one observational time (figure 7.7). Unlike in situ and geostationary observations, there is therefore only one observation at one grid position for a whole assimilation window.

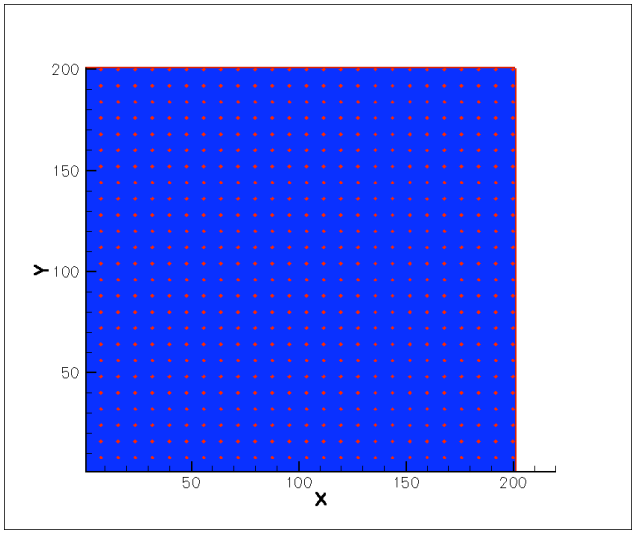

Figure 7.5: In situ observations at a given observation time for a space frequency of 8.

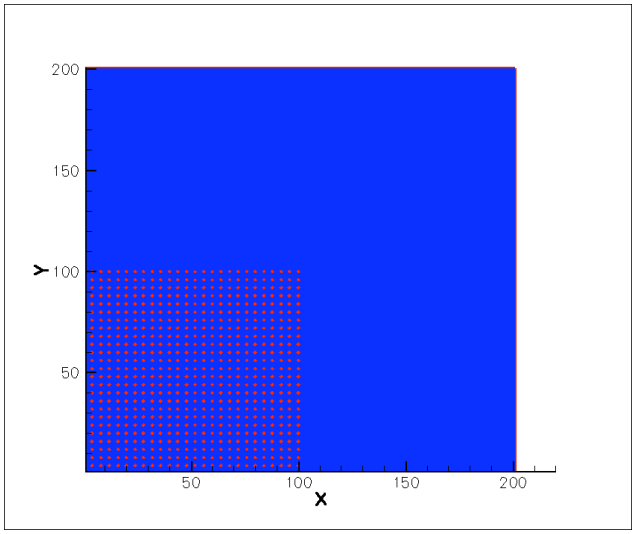

Figure 7.6: Geostationary observations at a given observation time for a space frequency of 4

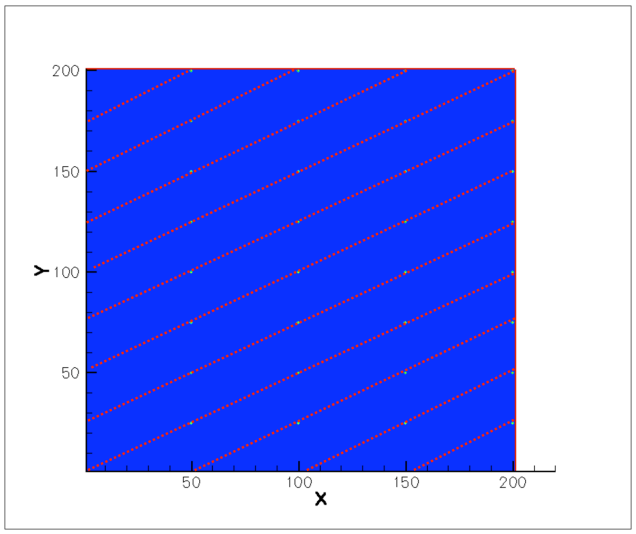

Figure 7.7: Satellite observations with 11 trails.

The assimilated observations are gathered into one series of observations $\mathbf{Y}^o$ of length p. Each subset of data has a specific dimension depending on the prescribed space and time frequency. Consequently, $\mathbf{H} = [\mathbf{H}_{ins}; \mathbf{H}_{geo}; \mathbf{H}_{sat}]^T$ and $\mathbf{R}$ is prescribed as a diagonal matrix such that:

$$\mathbf{R} = \begin{bmatrix} \sigma_{ins}^2 & 0 & 0 \\ 0 & \sigma_{geo}^2 & 0 \\ 0 & 0 & \sigma_{sat}^2 \end{bmatrix}$$

with $\sigma_{ins}^2 = (\alpha_{ins} \times \overline{\mathbf{Y}^o})^2$, $\sigma_{geo}^2 = (\alpha_{geo} \times \overline{\mathbf{Y}^o})^2$ and $\sigma_{sat}^2 = (\alpha_{sat} \times \overline{\mathbf{Y}^o})^2$. This will allow the study of the analysis as a function of the observations in terms of uncertainty, number and location.

In data assimilation, one method to objectively assess the quality of the assimilation is to check the analysis against independent unbiased data. Some observations may be kept so as to carry out an a posteriori validation of the analysis. However, this only works if the independent observations are on the way of the front. They shall indeed contain information on the dynamics of the fire which are concentrated at the interface between the burnt and unburnt regions.

7.2.2 Contribution of observations to the analysis

Quality of the analysis

In situ observations

A first series of experiments is carried for in situ observations only, each experiment has a different number of assimilated observations. $D_t = 0.5$, $D_b = 0.3$, $\alpha_o = 0.5$ and $\alpha_b = 0.01$ ($\sigma_b^2 = 9 \times 10^{-6}$) are the input parameters. Results are presented in table 7.2.

nbt	nbx/nby	p	σ_o^2	D_a	RMS(BMO)	RMS(AMO)
100	101/101	1,020,100	5.798×10^{-4}	0.4691	3.34×10^{-2}	5.01×10^{-3}
50	101/101	510,050	5.921×10^{-4}	0.4688	3.38×10^{-2}	5.11×10^{-3}
25	101/101	255,025	6.174×10^{-4}	0.4682	3.44×10^{-2}	5.32×10^{-3}
12	101/101	122,412	6.054×10^{-4}	0.4667	3.37×10^{-2}	5.43×10^{-3}
3	101/101	30,603	9.634×10^{-4}	0.4586	4.13×10^{-2}	8.49×10^{-3}
1	101/101	10,201	2.999×10^{-3}	0.4337	6.53×10^{-2}	2.23×10^{-2}

Table 7.2: Analysis as a function of the number of in situ observations. nbt represents the number of observations over time, nbx and nby the number of observations along the x-axis and the y-axis respectively, so p = nbt × nbx × nby gives the number of observations.

As expected, the analysis is moving away from D_t, in the direction of the background, when the number of observations p decreases. Nevertheless, even for one observation time and even for a ratio of 10^3 between the background variance and the observation variance, the analysis is still closer to D_t than to D_b. This is due to the large number of observations taken into account.

Geostationary observations

In a first experiment, only one observation is located at the centre of the domain, at the position of the initial flame where the temperature and fuel quantities are a priori known. Results are presented in table 7.3. About 100 observational times are required to obtain an analysis closer to the true coefficient than to the background ($D_a = 0.4247$ for p = 100).

One may consider that if the background and its associated uncertainty are fixed and if the analysis is studied as a function of the time observation frequency, the analysis will not change. No new information on the dynamics shall be extracted. However, this is not what is observed. It appears that the analysis changes when the number of time steps observed is modified. This means that the observation at the centre of the domain brings significant information on the system to allow a non-zero background correction. This

is explained by the thermal diffusion process occuring within the flame: the rate of diffusion gives indeed an insight of the magnitude of the rate of spread.

p	D_a	RMS(BMO)	RMS(AMO)
1	0.3086	9.08×10^{-2}	8.60×10^{-2}
4	0.3204	8.43×10^{-2}	7.43×10^{-2}
25	0.3693	7.88×10^{-2}	4.86×10^{-2}
100	0.4247	7.80×10^{-2}	2.65×10^{-2}
200	0.4450	7.78×10^{-2}	1.90×10^{-2}

Table 7.3: Analysis with only one observation at the centre of the domain.

A second step consists in studying the sensitivity of the analysis to the observation uncertainty, instead of to the number of assimilated observations, with $\alpha_b = 0.01$ and $\sigma_b^2 = 9 \times 10^{-6}$. The observations are only taken at one time step and more precisely at the end of the assimilation window ($t = 100$). Two different configurations are compared:

- case A: only one observation at the centre of the domain with a very high uncertainty.
- case B: 144 geostationary observations with a low uncertainty.

Results are presented in table 7.4. The objective of this study is to determine for which uncertainty, cases A and B lead to the same analysis diffusion coefficient. For instance, $D_a \approx 0.45$ for $\alpha_o = 0.0001$ in case A and for $\alpha_o = 0.06$ in case B. So there is a ratio of 6×10^3 in the observation variance between these two cases. This shows that despite of a low uncertainty, a large number of observations can be equivalent to one observation with a high confidence.

Case	α_o	σ_o^2	D_a	RMS(BMO)	RMS(AMO)
A	0.0001	5.25×10^{-9}	0.455	9.08×10^{-2}	1.61×10^{-2}
	0.001	5.25×10^{-7}	0.433	9.08×10^{-2}	2.51×10^{-2}
	0.003	4.73×10^{-6}	0.361	9.08×10^{-2}	5.05×10^{-2}
	0.004	3.28×10^{-6}	0.342	9.08×10^{-2}	6.74×10^{-2}
B	0.01	9.11×10^{-7}	0.485	6.83×10^{-2}	5.30×10^{-2}
	0.03	8.20×10^{-6}	0.476	6.83×10^{-2}	1.10×10^{-2}
	0.05	2.28×10^{-5}	0.461	6.83×10^{-2}	1.39×10^{-2}
	0.06	3.28×10^{-5}	0.452	6.83×10^{-2}	1.72×10^{-2}

Table 7.4: Analysis as a function of the observation uncertainty σ_o^2.

Furthermore, cases A and B gives a similar variance $\epsilon^o \approx 5 \times 10^{-6}$ for $\alpha_o = 0.004$ in case A ($D_a = 0.3416$) and $\alpha_o = 0.03$ in case B ($D_a = 0.4764$). An additional assimilation is carried out for 9 spatial observations, then the same level of variance is reached for $\alpha_o = 0.015$ ($D_a = 0.357$). Recall that the variance is prescribed equally to each observation, so even if the variance has the same level for the three different cases, it means that the confidence in the observations is degraded when there is a large number of observations. However, this degradation is counterbalanced, and even removed, by the number of assimilated observations. The analysis is indeed much closer to the true coefficient in case B than in the others.

So as to conclude, these three series of experiments show the impact of the number of observations and of their uncertainty on the analysis. Even though only few observations are available, if they are located along the fireline and if they are provided with a high confidence, they can bring significant information to the analysis. Nevertheless, the analysis will drop rapidly towards the background if this confidence is degraded. What is more, if there are numerous observations with a relatively high uncertainty, they can have a significant impact on the analysis as each observation carries an important amount of information when agregating all together, which can balance the information of one single observation of high confidence.

Quantitative contribution of the observations

Each observation, and at a larger scale each set of observations, contributes to the analysis at a different level. Indeed, the information extracted from these observations depend naturally on their respective position in the domain. Consequently, if the fire front is at some time close to one observed position, then this observation will likely have a precious information to bring to the assimilation.

This level of importance of the observations is determined by a quantity called DFS[2], defined in details in appendix B. This quantity diagnoses the contribution of a set of observations k on the reduction of the error variance in the analysis such that $DFS_k = \mathbb{E}[J_k^o(\mathbf{x}^a)]$ (J_k^o representing the cost function associated to the set k of observations, in other words the discrepancies between these observations and the background in the associated subset of the observation space).

In a first experiment, the three sets of observations are assimilated. According to [27], the sum of the contributions, background and observations, is equal to the dimension of the control space, so $n = 1$. However, the prototype only computes the DFS associated with the observations, while this diagnosis includes both background and observation contributions. So $n = 1$ is not reached for all assimilation configurations, especially if the background contribution is not negligible. This could be diagnosed by the value of the cost functions J^o and J^b at the analysis $\mathbf{x}^a$ as stated in equation (7.1).

$$\mathbb{E}[J(\mathbf{x}^a)] = \mathbb{E}[J^o(\mathbf{x}^a)] + \mathbb{E}[J^b(\mathbf{x}^a)] = \frac{p}{2} \tag{7.1}$$

Observations are extracted for a space and time frequency of 2. $D_b = 0.3$ and $\alpha_b = 0.01$, while $D_t = 0.5$ and $\alpha_o = 0.01$. This configuration gives an analysis of $D_a = 0.4719$, closer to $D_t = 0.5$ than to $D_b = 0.3$, with RMS(BMO) $= 4.47 \times 10^{-2}$, while RMS(AMO) $= 6.33 \times 10^{-3}$. This is consistent with the number of observations taken into account.

Quantification per set of observations

In this configuration, the contribution of all the assimilated observations to the analysis is DFS $= 0.998$, almost 1 as expected from the theory. The DFS can also be presented per set of observations so as to study which type of observations provides more information to the data assimilation algorithm. Results are given in table 7.5.

set	σ_o^2	RMS(BMO)	RMS(AMO)	DFS
ins	5.92×10^{-7}	4.99×10^{-2}	7.10×10^{-3}	0.532
geo	3.85×10^{-7}	4.88×10^{-2}	7.14×10^{-3}	0.179
sat	2.02×10^{-7}	2.88×10^{-2}	3.73×10^{-3}	0.287

Table 7.5: DFS diagnostic for the three sets of observations.

The highest contribution comes from the in situ observations: they cover indeed the whole domain with a high space and time frequency, while the geostationary observations are limited to one-quarter of the domain and the satellite observations are less dense. So in situ temperature measurements provide more information on the flame front, which does not propagate at the same speed in all directions. Furthermore, the contribution of the satellite observations is higher than the contribution of the geostationary observations. One explanation may come from the propagation of the flame, which tends to develop more towards the top of the domain where there is no geostationary observation.

Another assimilation is run with the same configuration, except that the satellite observations are not assimilated. Then, the analysis is $D_a = 0.4722$, with DFS$(ins) = 0.746$ and DFS$(geo) = 0.251$. The sum of the contributions is almost equal to 1. Furthermore, the analysis coefficient has not changed significantly. The RMS has not changed significantly either, with RMS(BMO) $= 4.97 \times 10^{-2}$ and RMS(AMO) $= 7.04 \times 10^{-3}$. This may indicate that there exists a threshold in the observation contribution to the assimilation: from a certain number of observations, the analysis does not change significantly as no new significant information on the system can be brought to the assimilation system.

[2]Degree of Freedom for Signals.

Quantification per observation

Considered as a whole for a set of observations, the DFS can also be computed per observation. In a second series of experiments, the DFS are computed per observation so as to give an insight of which observations bring the most significant information to the assimilation system with respect to their position and to their observation time.

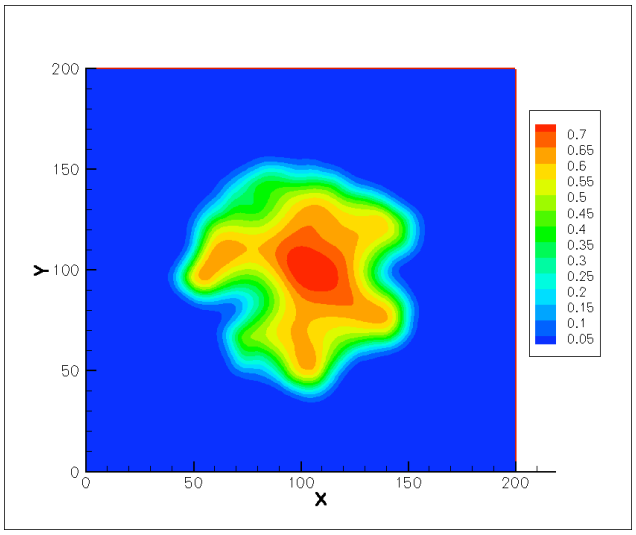

Figure 7.8: Analysed temperature field at $t = 100$.

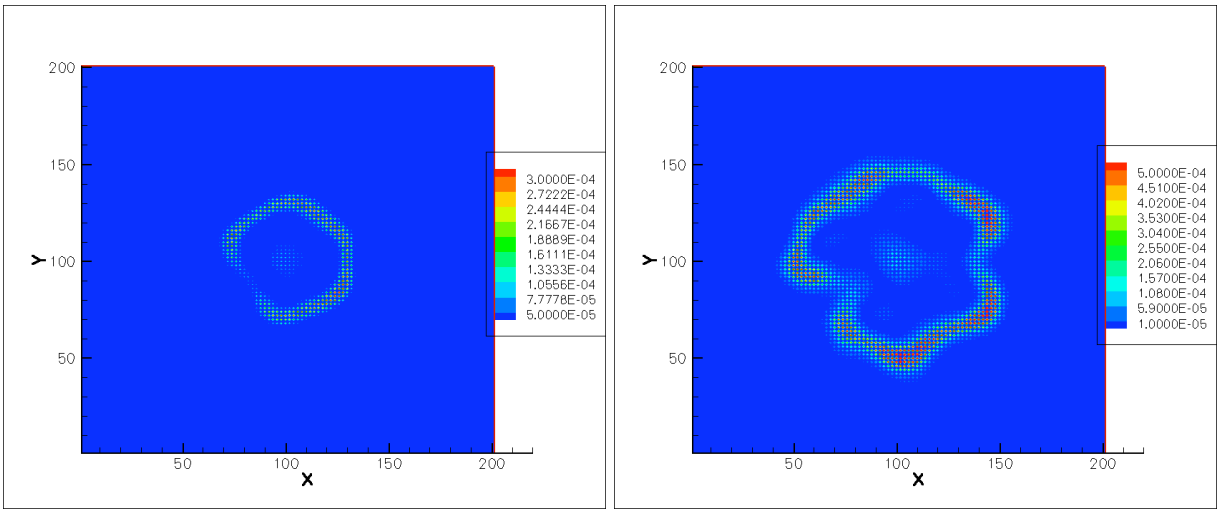

(a) Time $t = 50$ (b) Time $t = 100$

Figure 7.9: DFS of in situ observations for a spatial frequency of 2 at different times of the assimilation.

Two sets of observations (in situ and geostationary) are assimilated, with $\alpha_o = 0.01$ and an observation frequency of 2 in space and time for both sets. In this configuration, $D_b = 0.3$ and $D_t = 0.5$, leading to $D_a = 0.47$. The analysed temperature field is represented at the end of the assimilation window ($t = 100$) in figure 7.8. The DFS are represented at two different times, in the middle ($t = 50$) and at the end ($t = 100$) of the assimilation window for in situ observations. In figure 7.9(b), at the final time of the assimilation window, the DFS are strong along a more or less circular front which corresponds to the temperature front presented in figure 7.8. At the intermediate time in figure 7.9(a), they have about the same magnitude as at $t = 100$, and form a front of smaller radius, closer to the initial flame, which is associated to the front at $t = 50$. Clearly, the most important information are carried at a given time by the observations that are located along the front. This is consistent with the geostationary contributions represented in figures 7.10(a) and 7.10(b): the strong DFS are located in the same zone as for the in situ observations in the domain subset.

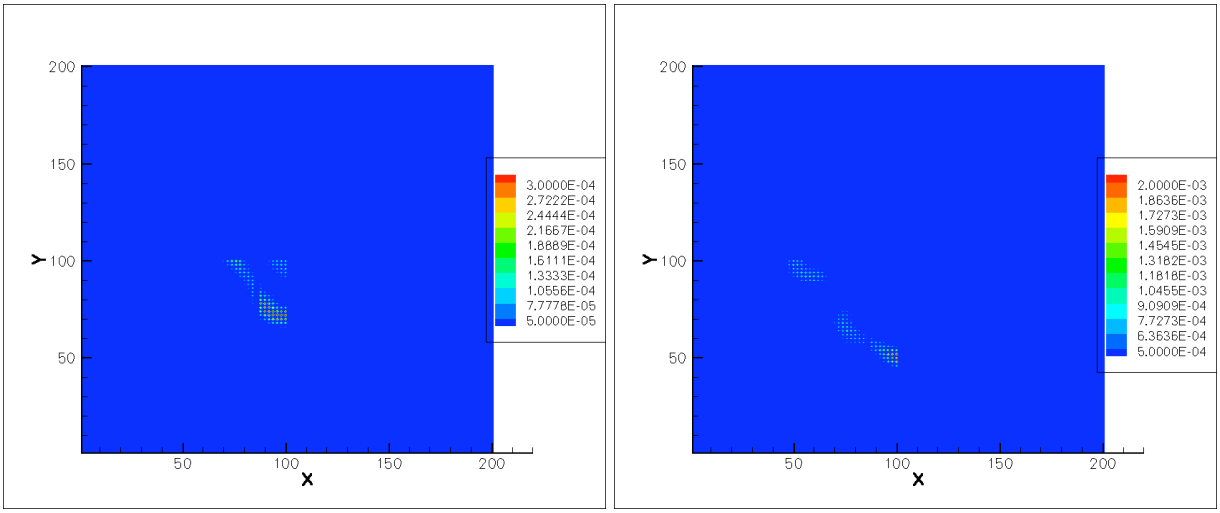

(a) Time $t = 50$ (b) Time $t = 100$

Figure 7.10: DFS of geostationary observations for a spatial frequency of 2 at different times of the assimilation.

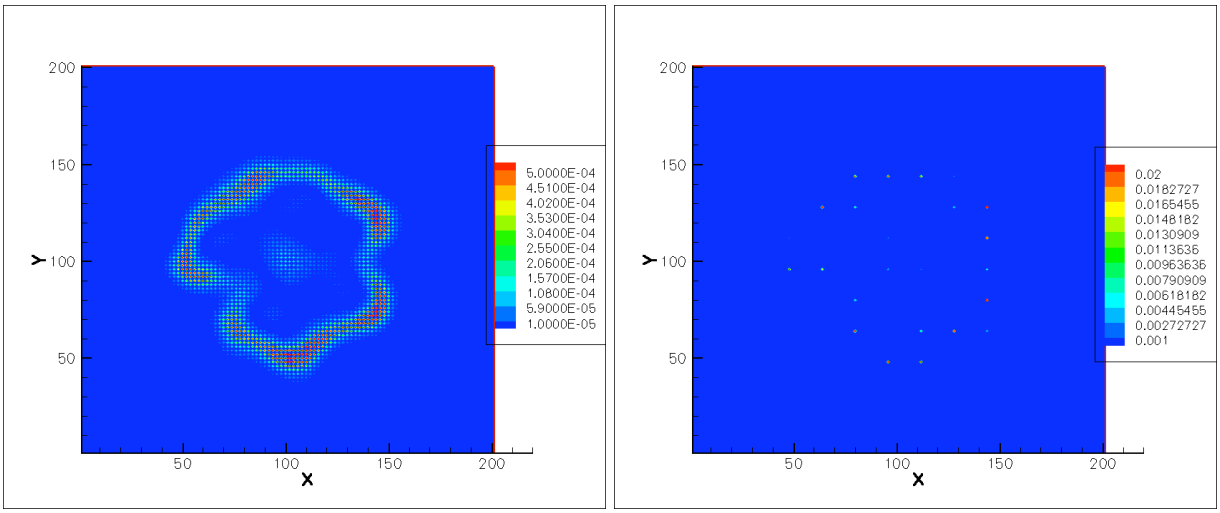

(a) Spatial frequency of 2 (b) Spatial frequency of 16

Figure 7.11: Comparison of the DFS of in situ observations at the end of the assimilation window ($t = 100$) with respect to the spatial observation frequency.

Another experiment is carried out with the same configuration, except that the space frequency is 16 instead of 2. Equivalently, there are 144 observations assimilated per observation time, instead of 10^4. The goal is to study the sensibility of the magnitude of these DFS along the flame front to the number of observations. Figures 7.11(a) and 7.11(b) confirm that for any space frequency, the most important information is concentrated along the front. Furthermore, they show that when the observation density is lower, each observation carries more information and so it has a higher contribution to the analysis. Indeed, the DFS have a maximum magnitude of 2×10^{-2} for a space frequency of 16, while this magnitude is of order 5×10^{-4} for a space frequency of 2.

So as to conclude, all these experiments highlight that the information on the fire system is located in the surrounding of the front, which moves over time depending on the location of the fuel pockets. The DFS are also relatively high within the fire, at the centre of the domain, due to the ongoing thermal diffusion. The DFS appear therefore as a powerful tool to measure which observations carry the most important information on the fire dynamics.

7.3 Data assimilation a posteriori diagnostics

More rigorous diagnostics of the data assimilation algorithm exist to ensure its consistency with the theory. In this work, they are applied within the framework of rigorous OSE: the background control parameter is specified as a perturbation of the true control parameter (which is used to define $\mathbf{B}$), and the observations are not perfect (their noise follows a smooth Gaussian distribution defining the uncertainty ϵ^o).

7.3.1 PDF of the innovation and residual vectors

So as to simplify the interpretation of the PDF of the BMO/AMO, the model is initialized with the isotropic fuel field without any random fuel pockets. So the relation $\theta + Y = 1$ is satisfied for all time steps, and the fire propagates as a circular front. Assimilation is carried out for $D_t = 0.3$ and $D_b = 0.27$, so $\sigma_b = 3 \times 10^{-2}$. 1728 observations are assimilated, corresponding to an observation frequency of 16 in space and time. The reaction coefficient is $a = 0.15$ and is constant during the whole assimilation window.

As $D_t > D_b$ and a is fixed, the true fire front propagates faster than the background. This means that the discrepancies between the true and background trajectories with respect to the centre of the flame are expected to be all negative, and to have the highest magnitude where the fire front is not well located. This is the result presented in figure 7.12: the diffusion coefficients are not too far away from each other, so the discrepancies reach only a maximum magnitude of 0.008 and are concentrated along the fire front in the vicinity of $x = 50$ and $x = 150$. Away from this circular front, they are indeed almost zero as the histogram 7.13 shows: most of the observations have indeed a BMT lower than 10^{-3} in absolute value, only few cover the range $[-8 \times 10^{-3}, -1 \times 10^{-3}]$.

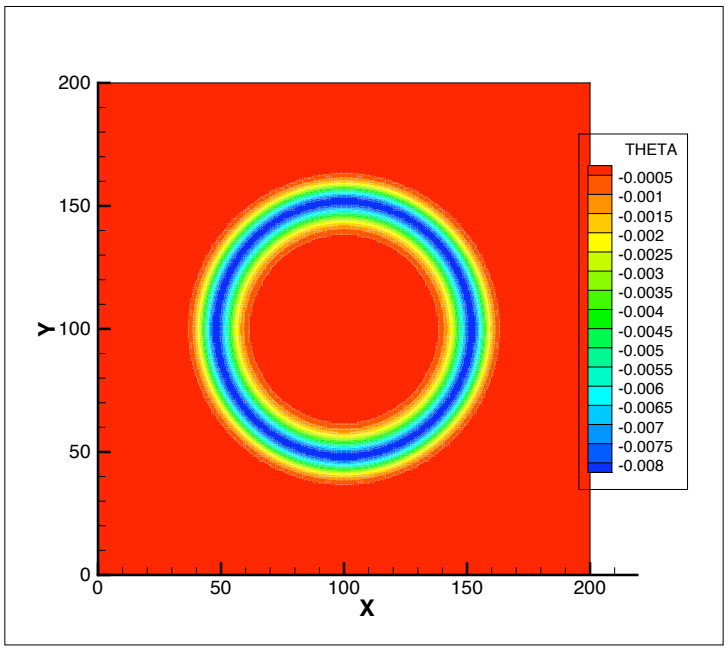

Figure 7.12: BMT field at $t = 100$, associated to $D_t = 0.3$ and $D_b = 0.27$.

With this consistent verification, the histogram of the corresponding BMO/AMO can be studied. They are represented respectively in figures 7.14(a) and 7.14(b). Both diagrams are close to a Gaussian distribution. The BMO were expected to be all negative as the BMT, but this is not systematically satisfied as it depends on the size of the interval $[D_b; D_t]$ as well as on the magnitude of the noise inserted. This is highlighted by figures 7.15 and 7.16. They show the x-profile of the BMO and BMT for $y = 104$ at the end of the assimilation window ($t = 100$) with $a = 0.15$ fixed. The BMO are represented for different observation errors, determining the standard deviation of the noise Gaussian distribution inserted in the observations. The higher α_o, the higher the perturbation.

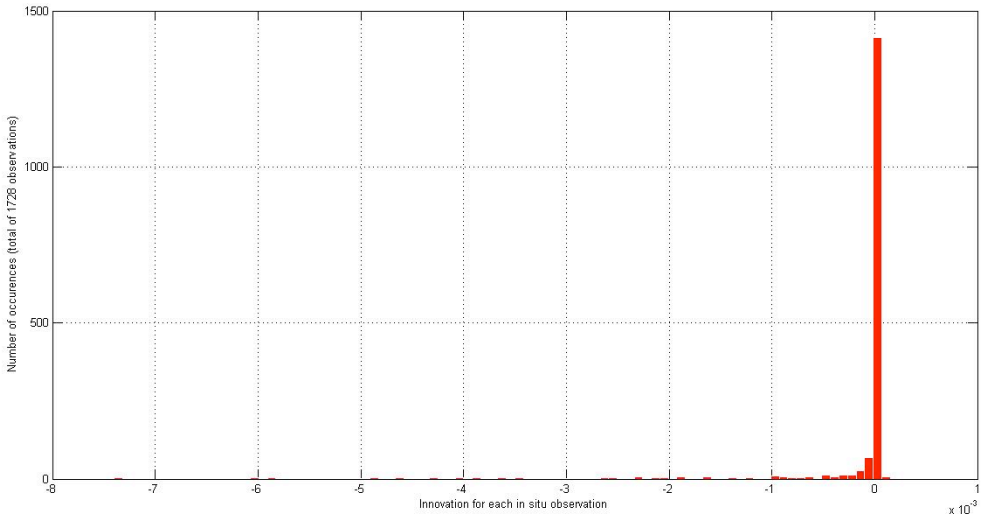

Figure 7.13: Histogram of the BMT vector at $t = 100$.

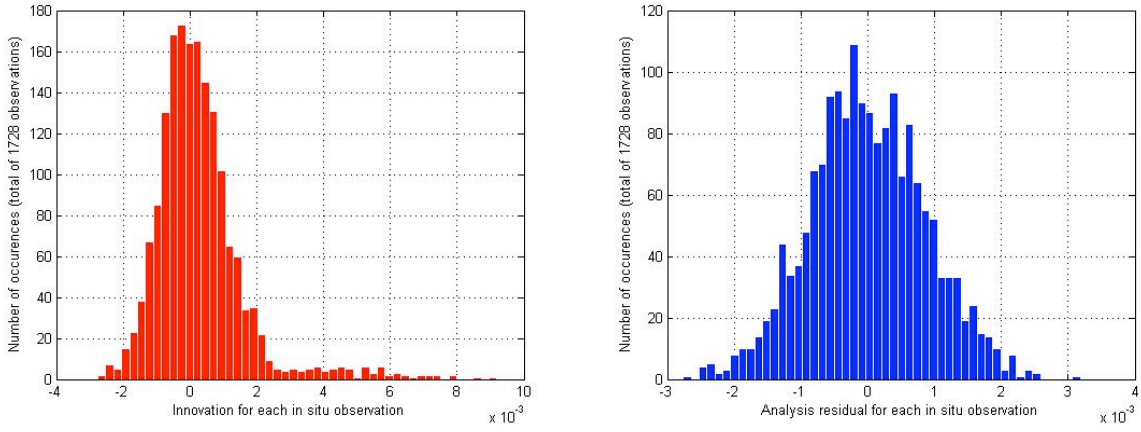

(a) BMO vector

(b) AMO vector

Figure 7.14: Histogram of the BMO/AMO vectors at $t = 100$.

In figure 7.15, the background is highly perturbed with $D_b = 0.15$, while $D_t = 0.30$. When the noise is low, the values of the BMO are very close to those of the BMT at the observation points. When it becomes larger, the discrepancies between the BMT and BMO increase. For instance, for $\alpha_o > 10^{-1}$, where BMT $= 0$, the BMO are not zero and are even of random sign. This is directly the noise which is represented.

In figure 7.16, the interval $[D_b; D_t]$ is much thinner as $D_b = 0.297$, while D_t is still 0.3. Two different observation errors are represented, $\alpha_o = 10^{-2}$ and $\alpha_o = 10^{-6}$. While the BMO are all negative and close to the BMT for the smallest perturbation, this is no longer the case for $\alpha_o = 10^{-2}$. As for $D_b = 0.15$, some positive BMO appear where BMT $= 0$, this is due to the magnitude of the noise.

This series of results on the BMO/AMO vectors indicates that the noise introduced to the observations shall be chosen according to the size of the interval along which the control parameters vary. Otherwise, the observation signal would be drastically modified compared to the true trajectory, and would only represent the random noise.

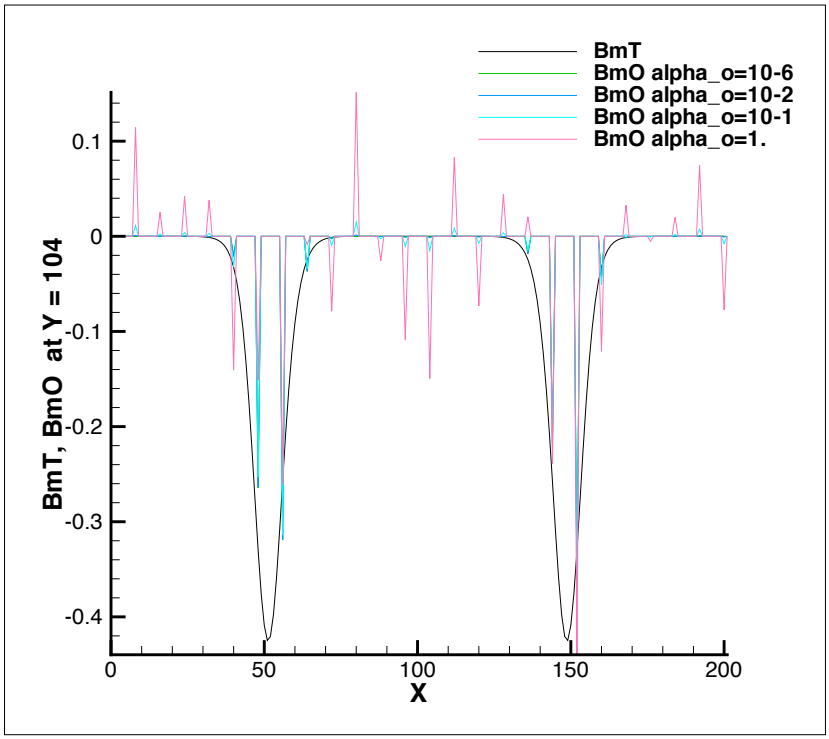

Figure 7.15: 1D-profile of the BMO and BMT for $D_t = 0.3$, $D_b = 0.15$.

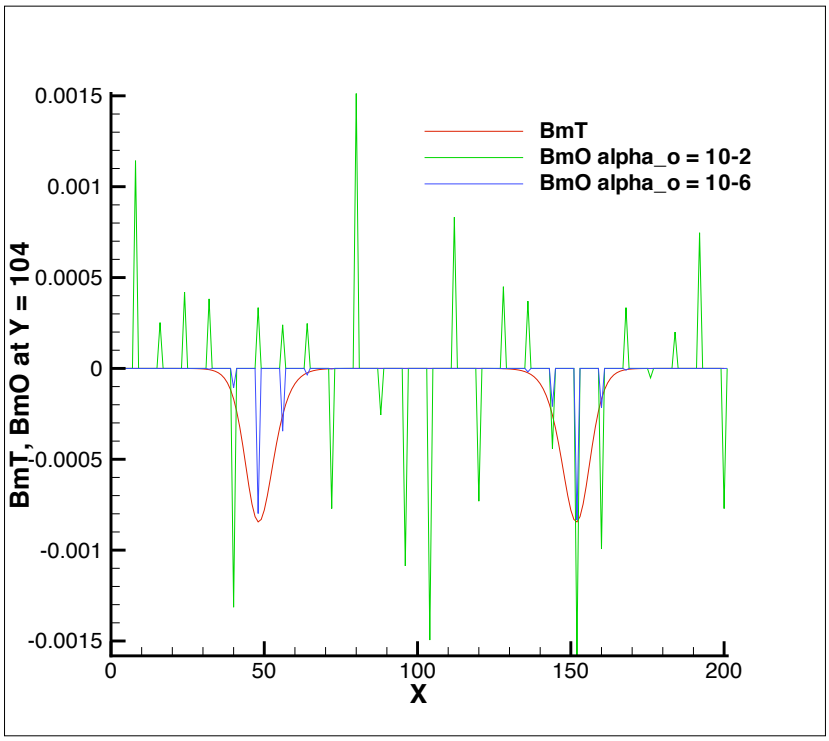

Figure 7.16: 1D-profile of the BMO and BMT for $D_t = 0.3$, $D_b = 0.297$.

7.3.2 A posteriori diagnostics

In [28], four diagnostics have been established in the observation space for the covariances of the observation, background, analysis and innovation vector. Presented in appendix C, they define an a posteriori

validation of the prescribed observation and background variance errors on the one hand, and constitute a validation of the twin experiments on the other hand. They are summarized below:

$$\begin{aligned}
\mathbb{E}[\mathrm{OMB}\cdot\mathrm{OMB}^T] &= \mathbf{R}+\mathbf{H}\,\mathbf{B}\,\mathbf{H}^T \\
\mathbb{E}[\mathrm{AMB}\cdot\mathrm{OMB}^T] &= \mathbf{H}\,\mathbf{B}\,\mathbf{H}^T \\
\mathbb{E}[\mathrm{OMA}\cdot\mathrm{OMB}^T] &= \mathbf{R} \\
\mathbb{E}[\mathrm{AMB}\cdot\mathrm{OMA}^T] &= \mathbf{H}\mathbf{A}\mathbf{H}^T
\end{aligned}$$

with OMB the innovation vector, OMA the residual vector, and AMB the discrepancies between the analysis and the background in the observation space such that $\mathrm{AMB} = \mathbf{H}\,(\mathbf{X}^a - \mathbf{X}^b)$.

These diagnostics are performed in the observation space, the resulting quantities are therefore of dimension $p \times p$, where p is the total number of observations assimilated. In practice, only the trace of these matrices will be considered and both sides of the equalities will be analyzed in terms of the mean value. In this work, two assimilation configurations will be tested. Both consider 1728 in situ observations with the same confidence ($\alpha_o = 0.01$ and $\sigma_o^2 = 7.31 \times 10^{-7}$), a true diffusion coefficient of $D_t = 0.3$ with an active fuel diffusion ($k = 1$) and a fixed reaction term $a = 0.15$. The initial condition is the homogeneous fuel field with $Y = 1$ everywhere, except at the flame central position. The only difference between both configurations is the perturbation introduced in the background: in case A, $D_b = 0.297$ (1% perturbation), while in case B $D_b = 0.27$ (10% perturbation). The results of the assimilation are given in table 7.6, diagnostics in table 7.7.

case	σ_b^2	D_a	σ_a^2	RMS(TMB)	RMS(TMA)
A	9.00×10^{-6}	0.2999	3.05×10^{-9}	1.06×10^{-3}	6.75×10^{-6}
B	9.00×10^{-4}	0.2997	2.98×10^{-9}	1.06×10^{-2}	7.26×10^{-5}

Table 7.6: Assimilation results for both configurations A and B.

case		innovation	background	observation	analysis
A	measure	1.987×10^{-6}	1.230×10^{-6}	7.582×10^{-7}	1.438×10^{-9}
	diagnosis	1.976×10^{-6}	1.244×10^{-6}	7.308×10^{-7}	4.228×10^{-10}
B	measure	1.269×10^{-4}	1.260×10^{-4}	1.565×10^{-6}	8.177×10^{-7}
	diagnosis	1.285×10^{-4}	1.262×10^{-4}	7.308×10^{-7}	4.229×10^{-10}

Table 7.7: Diagnostics results for both configurations A and B.

These results validate the implementation of the twin experiments as the background and observation variances are consistent with the associated diagnostics. In particular, the results for the innovation and background quantities are equal to the diagnostics by less than 2% for both cases A and B.

As to the observation, the diagnosis is not as precise as for the background and innovation, but stays very good for small perturbations as the distance between the measure and the diagnosis is less than 5% in case A. But this distance is much larger in case B with a larger perturbation in the background. This may be due to a misspecification in the observation error. This prototype is build on two major assumptions: $\mathbf{R}$ is diagonal, meaning that there is no spatial correlation between the observation errors, and the variance errors on the observations are independent. In this work, these are not completely satisfied as the variance is the same for all measurements (computed as a percentage of the mean value of the temperature field) and there is no spatial correlation modeled, which is a common assumption in data assimilation.

The assumptions in the characteristics of the observations may be at the origin of the discrepancies in the analysis diagnosis. They may also arise from the non-linearities of the observation operator H. However, despite of these discrepancies, the analysis diffusion coefficient is about the same in both cases, while the background is further away from the true trajectory. It appears that $\mathbf{A}$ has the same magnitude, and that the distance between the true and analysed trajectories is significantly reduced in both cases. So the data assimilation algorithm seems to work properly.

7.4 Sensitivity of the observation operator

The different experiments show that the BLUE algorithm is particularly sensitive to the choice of the diffusion coefficient D and of its incertainty. So this part aims at investigating the sensitivity of the analysis to the linearization of H, and at quantifying the errors introduced in the analysis by the construction of $\mathbf{H}$ with respect to D.

During the assimilation process, the tangent linear of H is computed using a non-centered finite difference scheme, with a control parameter $\mathbf{X}^g$ and its prescribed perturbation $\delta\mathbf{X}^g$, such that:

$$\mathbf{H} = \frac{H(\mathbf{X}^g + \delta\mathbf{X}^g) - H(\mathbf{X}^g)}{\delta\mathbf{X}^g} \tag{7.2}$$

To investigate the quality of this linearization, one may compare two quantities:

- the temperature field T_m resulting from the model integration with a perturbed control parameter $\mathbf{X}^m = \mathbf{X}^g + \epsilon$ (satisfying $\delta\mathbf{X}^g < \epsilon$),
- the temperature field T_h resulting from a Taylor development such that $T_h = T_h + \mathbf{H}\,\epsilon$, with T_h the temperature field associated to $\mathbf{X}^g$.

In an ideal case when H is linear, both temperature fields T_m and T_h are identical. In practice, measuring the relative error r_h between these two quantities for different perturbations ϵ indicates the magnitude of the non-linearities:

$$r_h = \frac{T_h - T_m}{T_h} \tag{7.3}$$

Aberrant relative errors r_h are observed in all the corners of the square domain due to border effects. However, they do have any influence in the assimilation as the front has not reached these zones at the end of the assimilation window (the temperature is close to 0 at these locations). In this sensitivity study, temperatures T_m and T_h are therefore compared at a few grid points located along the path of the flame during the assimilation window. More precisely, 9 grid points are taken into account as defined in table 7.8.

point	x	y
1	50	50
2	100	50
3	150	50
4	50	100
5	100	100
6	150	100
7	50	150
8	100	150
9	150	150

Table 7.8: Coordinates of the 9 points of the **H**-sensitivity study.

Data assimilation is applied for a background $D = 0.3$, with $a = 0.15$. The relative error r_h is analyzed as a function of time, at the 9 different grid points, for two different perturbations ϵ presented in table 7.9. Results are presented in figures 7.17 and 7.18. As expected from the physics of the problem (non-linear dependence of the solution on D), r_h grows over time. Furthermore, it also increases when an observation point is further away from the centre of the domain: the lowest error at all time steps is always associated with the measurement at the centre point (point 5). The value of r_h at this location is even negligible compared to all the other points.

The results show that the magnitude of r_h is highly dependent on the prescribed perturbation ϵ. The discrepancy between both quantities T_m and T_h is less than 0.5% with a 2%-perturbation, but reaches 20% for points 6 and 8 with a 20%-perturbation. So this study indicates the impact of the non-linearities of H

$\mathbf{X}$	$\mathbf{X} + \delta\mathbf{X}$	ϵ
D	0.303	0.306
	0.360	0.440

Table 7.9: Specification of perturbations for **H**-sensitivity study.

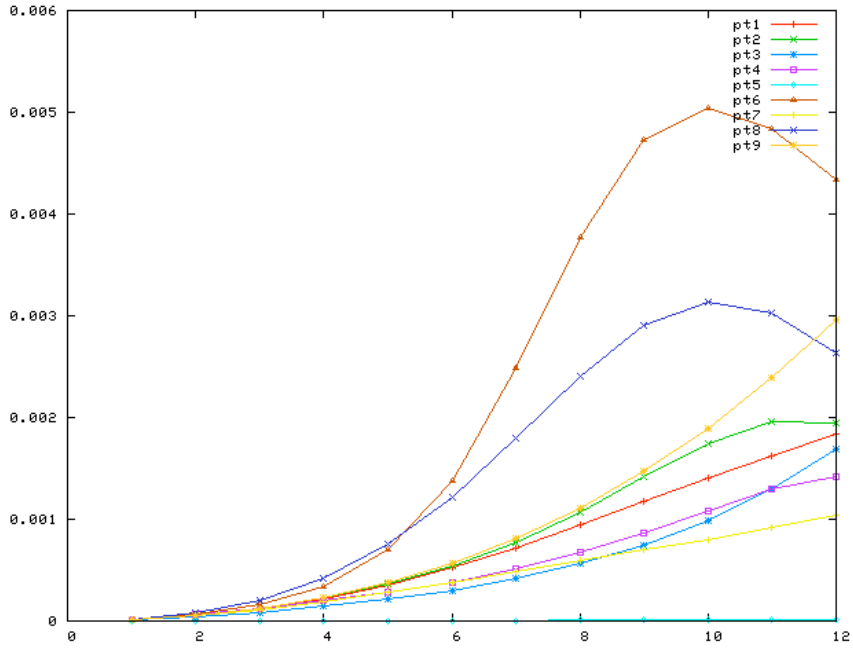

Figure 7.17: Evolution of the relative error r_h over time with a perturbation of 2%. The abscissa axis represents the 12 time steps at which the residual on the temperature is computed, while the ordinate axis gives the magnitude of the relative error r_h.

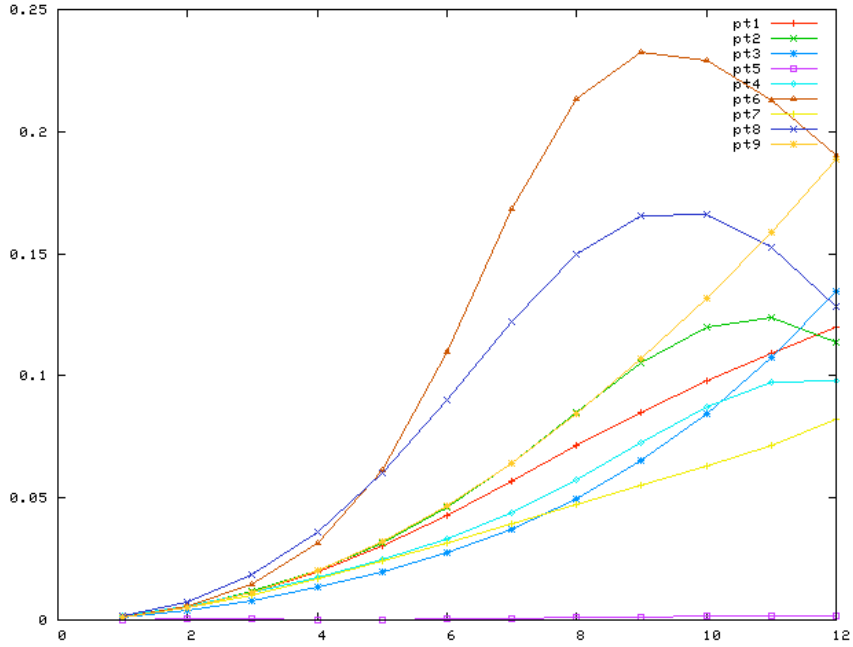

Figure 7.18: Evolution of the relative error r_h over time with a perturbation of 20%. The abscissa axis represents the 12 time steps at which the residual on the temperature is computed, while the ordinate axis gives the magnitude of the relative error r_h.

with respect to D. It shows that the background shall be chosen according to the domain of validity of $\mathbf{H}$. In other words, the BLUE can only provide a reliable analysis if the perturbation in D does not overcome 20%.

Conclusion

This prototype confirms that data assimilation systems allow the use of a wide range of observations, in particular in situ and satellite data. However, it shows that the analysis results from a sensitive balance between the number of observations, their location in the domain and their associated uncertainty with respect to the definition of the background.

Consistency diagnosis such as DFS and AMO/BMO provide information on the quality of the background correction with almost no extra cost, as they result from the combination of quantities that are required during the data assimilation process. These diagnosis measure indeed the optimality of the analysis and may indicate imperfection in the prescribed error statistics. In practice, DFS may be also used to determine which are the best locations of the temperature measurements so as to maximize their contribution to the analysis and so as to optimize the number of sensors in the domain. It could be a useful tool to identify the best strategy in building an observation network.

This first stage of the feasibility study proves that data assimilation algorithms can be adapted for fire applications, even if the information about the system dynamics is confined within the thin combustion zone.

8. Towards the Assimilation of the Fire Rate of Spread

The rate of spread of a wildfire raises from a combination of numerous physical processes. In the models considered in this work, the flame propagation is influenced by two processes: thermal diffusion which spreads out heat over the domain, and chemical reactions which are localized in the vicinity of the front and which enhance the diffusion due to the heat release. While the vegetation distribution defines the direction of the fire spread, the diffusion and reaction coefficients have a significant impact on the magnitude of the flame propagation speed as proved by the KPP analysis.

A large part of the uncertainty in a real fire is linked to the nature of the burning components. As the model parameters D and a are highly dependent on the characteristics of these materials and as s_L can be fully specified by these parameters thanks to the KPP analysis, a first stage towards the assimilation of the wildfire rate of spread is to calibrate both the diffusion and reaction coefficients D and a using the premixed combustion model.

The next stage is to build a data assimilation prototype using the fire spread model presented in chapter 6 and assimilating measurements of the progress variable c at fixed locations over the square domain. In this context of OSE, the prototype calibrates one single control parameter, the constant of proportionality between the velocity field and the vegetal fuel distribution.

8.1 Duo of control parameters

8.1.1 Adaptation of the assimilation algorithm

Definition of the observation operator

D and a define the control space as there are still more observations than background variables. The control space is therefore of the same dimension as the background space with $n = 2$. $\mathbf{B}$ is a square matrix of dimension 2×2. The diagonal terms of this matrix indicate the error variance on each control parameter considered separately, while the off-diagonal terms model the error correlations between D and a. As both model parameters arise from very distinct physical processes before combining together to determine the flame speed, it seems reasonable to assume that their errors are independent. $\mathbf{B}$ is therefore modeled as a diagonal matrix. Each diagonal term is the error variance computed as for the calibration of D only, that is to say as the square of a percentage of the background control variable: $\epsilon^b = (\alpha_b \, \mathbf{X}^b)^2$.

As in the previous assimilations, the observations are built using temperature measurements provided by the three available sets of observations. So the covariance matrix $\mathbf{R}$ is not modified by the number of parameters to calibrate: ϵ^o is equal to the square of a percentage of the mean true temperature field when no noise is introduced.

However, an update of the observation operator is required so as to correct the new control parameter a. As both control parameters are assumed to have uncorrelated errors, the linearization of H is separated into two independent computations, one for the perturbation of D, another for the perturbation of a, while the other control parameter stays fixed. So the new observation operator has two columns, one column per control parameter, with $\mathbf{H} = [\mathbf{H}_D; \mathbf{H}_A]$:

$$\mathbf{H}_D \quad = \quad \frac{H(D + \delta D, a) - H(D, a)}{\delta D}$$

$$\mathbf{H}_A \quad = \quad \frac{H(D, a+\delta a) - H(D,a)}{\delta a}$$

Sensitivity of the observation operator

The sensitivity of H shall also be investigated with respect to a. As for D, the relative error r_h is studied over time at the 9 different grid points for two ϵ-perturbations, specified in table 8.1, presented in figures 8.1 and 8.2. The parameters are set to $a = 0.15$ and $D = 0.3$.

$\mathbf{X}$	$\mathbf{X} + \delta\mathbf{X}$	ϵ
a	0.1515	0.1530
	0.1800	0.2100

Table 8.1: Specification of perturbation for **H**-sensitivity study.

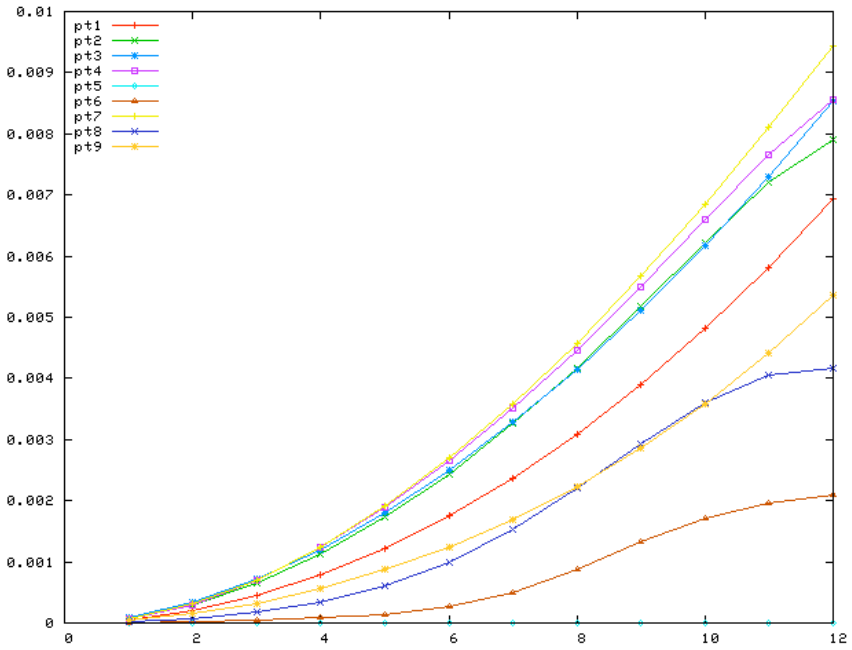

Figure 8.1: Evolution of the relative error r_h over time with a perturbation of 2%. The abscissa axis represents the 12 time steps at which the temperature residual is computed, while the ordinate axis gives the magnitude of the relative error r_h.

The same trends are observed as in the sensitivity study for D. r_h reaches a minimum value at the cent of the domain. However, these results highlight that H is affected by even stronger non-linearities with regards to a for comparable perturbation. Indeed, for a perturbation of 2%, r_h reaches 1% for a and is therefore twice larger than for D. This ratio is about the same for a perturbation of 20%, as for half of the observation points the error reaches 40% at the end of the assimilation window (compared to 20% for D). In general, the perturbation in a shall not overcome 10% during the assimilation window so as to guarantee an optimal analysis.

8.1.2 Data assimilation prototype

The assimilation prototype can be tested for the calibration of two control parameters within the context of OSE. One consistency diagnostic is given by the expectation value of the cost function evaluated at $\mathbf{x}^a$, with $\mathbb{E}[J(\mathbf{X}^a)] = \mathbb{E}[J^o(\mathbf{X}^a)] + \mathbb{E}[J^b(\mathbf{X}^a)] \approx p/2$.

For this validation step, $D_t = 0.3$ and $a_t = 0.15$. The background parameters are defined with an

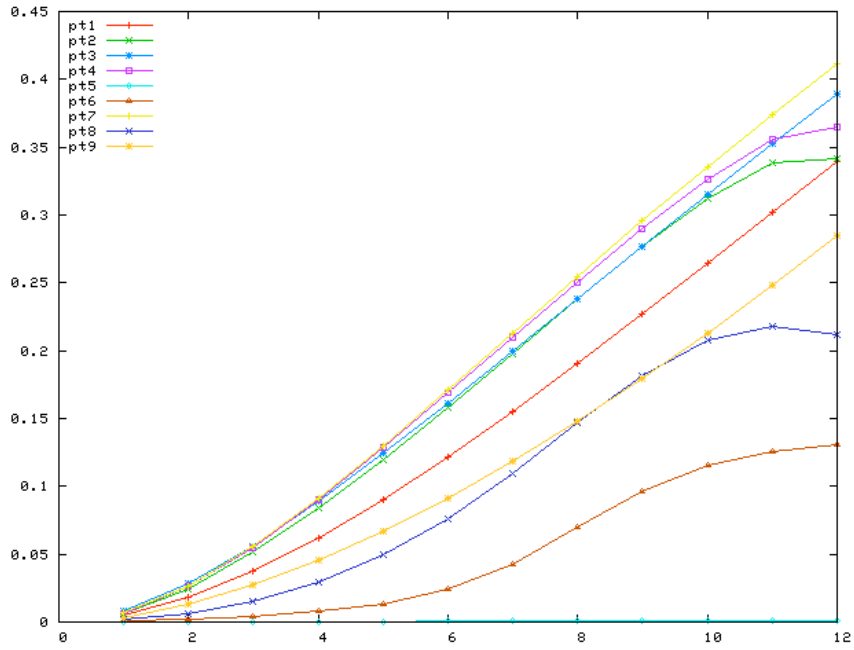

Figure 8.2: Evolution of the relative error r_h over time with a perturbation of 20%. The abscissa axis represents the 12 time steps at which the temperature residual is computed, while the ordinate axis gives the magnitude of the relative error r_h.

uncertainty of 10% for D and 5% for a, leading to $D_b = 0.27$ and $a_b = 0.1575$. Hence,

$$\mathbf{B} = \begin{bmatrix} 9.00 \times 10^{-4} & 0 \\ 0 & 5.62 \times 10^{-5} \end{bmatrix}$$

In situ observations are built with an equal space and time frequency for each experiment. The resulting analysis is studied as a function of the number of observations ($\alpha_o = 0.01$ fixed). Results are presented in table 8.2, where r_{da} represents the relative error between $\mathbb{E}[J(\mathbf{X}^a)]$ and $p/2$ in the data assimilation process.

Obs. frequency	D_a	a_a	$\mathbb{E}[J(\mathbf{X}^a)]$	$p/2$	r_{da}
2	0.2988	0.15005	320,000	500,000	0.36
16	0.2989	0.15006	661	864	0.23
64	0.2982	0.15010	24	13	0.46
100	0.3037	0.1564	0.78	4	0.80

Table 8.2: Analysis diagnostic as a function of the number of observations p.

From these results it appears that the consistency diagnostic is not completely satisfied by the analysis. However, for an observation frequency between 2 and 64, $\mathbb{E}[J(\mathbf{X}^a)]$ is of the same order of magnitude as $p/2$ with a relative error r_{da} less than 50%. Furthermore, the algorithm gives consistent results with a reduction of the distance between the true and analysed trajectories in average and a reduction of the distance between the observations and the analysis in average. For instance, for an observation frequency of 2, RMS(TMA) $= 1.52 \times 10^{-3} <$ RMS(TMB) $= 2.33 \times 10^{-3}$ for the θ-variable, and RMS(AMO) $= 3.59 \times 10^{-4} <$ RMS(BMO) $= 2.38 \times 10^{-3}$.

This consistency diagnostic is not valid for a higher observation frequency. For an observation frequency of 100, there are only 8 observations assimilated, so the value of the cost function is mainly due to the background. J^b is significantly higher than J^o, with $\mathbb{E}[J^b(\mathbf{X}^a)] = 1.2878$, while $\mathbb{E}[J^o(\mathbf{X}^a)] = 0.2801$. The resulting expectation value of the cost function is 0.7839, while it shall be 4 if the assimilation were to work perfectly. D_a is not even in the interval $[D_b; D_t]$. This significant discrepancy may be due to the misspecification in the background covariance matrix. The results show indeed that the off-diagonal terms of

A cannot be neglected, and are even of the same order of magnitude as the diagonal terms (as shown in table 8.3). This may indicate that the error correlations between a and D are not independent ($\mathbf{A} = (\mathbf{I} - \mathbf{K}\,\mathbf{H})\mathbf{B}$).

For an observation frequency between 2 and 64, where the background does not seem to have a significant weight in the assimilation, the relative error r_{da} may be explained by another assumption: the observation errors are supposed to be independent, but in practice such a constraint is relatively difficult to satisfy.

Obs. frequency	**A**	
2	2.15×10^{-11}	-4.37×10^{-12}
	-4.37×10^{-12}	1.07×10^{-12}
16	1.30×10^{-8}	-2.56×10^{-9}
	-2.56×10^{-9}	6.19×10^{-10}
100	1.62×10^{-5}	2.36×10^{-5}
	2.36×10^{-5}	5.56×10^{-5}

Table 8.3: Analysis error covariance matrix **A** as a function of the observation frequency.

8.1.3 Analysis as an iterative process

A solution to overcome the non-linearities would be to define the analysis as an iterative process with external loops as in the 1D-diffusion-calibration sample model. In the context of OSE, $D_t = 0.3$, $a_t = 0.15$, $D_b = 0.27$ and $a_b = 0.1575$. Hence,

$$\mathbf{B} = \begin{bmatrix} 9.00 \times 10^{-4} & 0 \\ 0 & 5.63 \times 10^{-5} \end{bmatrix}$$

A homogeneous condition in fuel is initialized. There is no fuel diffusion. In situ observations are built using a space and time frequency of 16, so that there are 1728 assimilated observations in this experiment, associated to $\alpha_o = 0.01$. Two strategies are tested, one with the update of **H** only, another with the update of **B** in addition.

Update of **H** only

In this first experiment, the tangent linear **H** is more valid in the vicinity of the true control parameters iteration after iteration. After 4 iterations, $D_a = 0.3004$ and $a_a = 0.1501$, providing a more accurate state of the system as RMS(BMO) $= 2.99 \times 10^{-3} >$ RMS(AMO) $= 3.80 \times 10^{-4}$ on the one hand, RMS(TMB) $= 2.89 \times 10^{-3} >$ RMS(TMA) $= 1.23 \times 10^{-4}$ for the θ-variable on the other hand. The value of the cost function at the analysis is the same as when there is no external loop, with $J(\mathbf{x}^a) = 661$ and $p/2 = 864$. More details about the data assimilation results are provided in table 8.4.

iteration	$\mathbf{x}^b$	$\mathbf{x}^a$	**A**		correlation matrix	
1	0.2700	0.2999	1.52×10^{-8}	-2.72×10^{-9}	1.00	-0.926
	0.1575	0.1499	-2.72×10^{-9}	5.68×10^{-10}	-0.926	1.00
2	0.2700	0.3003	1.63×10^{-8}	-2.76×10^{-9}	1.00	-0.922
	0.1575	0.1501	-2.76×10^{-9}	5.51×10^{-10}	-0.922	1.00
3	0.2700	0.3004	1.63×10^{-8}	-2.76×10^{-9}	1.00	-0.922
	0.1575	0.1501	-2.76×10^{-9}	5.51×10^{-10}	-0.922	1.00
4	0.2700	0.3004	1.63×10^{-8}	-2.76×10^{-9}	1.00	-0.922
	0.1575	0.1501	-2.76×10^{-9}	5.51×10^{-10}	-0.922	1.00

Table 8.4: Results of the external loops with the update of **H** only.

From this series of results, it appears that the structure of the matrix **A** does not change significantly iteration after iteration, neither do the analysis control parameters. The associated correlation matrix is also computed: by definition the diagonal terms are exactly 1, while the off-diagonal term is obtained by

dividing the covariance of the two control parameters by the product of their standard deviations. It gives the correlation coefficient $\rho_{D,a}$ such that:

$$\rho_{D,a} = \frac{cov(\epsilon_D^a, \epsilon_a^a)}{\sigma_{a,D}\,\sigma_{a,a}} \tag{8.1}$$

with $\sigma_{a,D}$ and $\sigma_{a,a}$ the analysis standard deviation associated to D and a respectively, ϵ_D^a and ϵ_a^a the variance associated to D and a respectively. Here $\rho_{D,a} = -0.922$.

Update of **H** and **B**

The same assimilation configuration is considered to test the external loops with the update of the background error covariance matrix **B**. It gives therefore more weight to the background at each iteration: as the analysis is closer to the true state than to the background, and as **B** is updated with **A**, the background is granted a higher confidence at the next iteration. Resuts are presented in table 8.5.

iteration	$\mathbf{x}^b$	$\mathbf{x}^a$	**A**		correlation matrix	
1	0.2700	0.2999	1.52×10^{-8}	-2.72×10^{-9}	1.00	-0.926
	0.1575	0.1499	-2.72×10^{-9}	5.68×10^{-10}	-0.926	1.00
2	0.2700	0.2856	7.82×10^{-9}	-1.36×10^{-9}	1.00	-0.924
	0.1575	0.1537	-1.36×10^{-9}	2.79×10^{-10}	-0.924	1.00
3	0.2700	0.2800	5.23×10^{-9}	-9.12×10^{-10}	1.00	-0.924
	0.1575	0.1550	-9.12×10^{-10}	1.86×10^{-10}	-0.924	1.00
4	0.2700	0.2774	3.91×10^{-9}	-6.84×10^{-10}	1.00	-0.924
	0.1575	0.1556	-6.84×10^{-10}	1.40×10^{-10}	-0.924	1.00

Table 8.5: Results of the external loops with the update of **H** and **B**.

At the end of the external loops, the assimilation diagnostics are consistent as RMS(AMO) $= 2.27 \times 10^{-3} <$ RMS(BMO) $= 2.99 \times 10^{-3}$, and RMS(TMA) $= 2.18 \times 10^{-3} <$ RMS(TMB) $= 2.89 \times 10^{-3}$. As expected, these measures of the RMS of the distance between the analysed and background trajectory show that step by step the analysis is closer to the background, and that the confidence in the background increases iteration by iteration. Furthermore, the structure of the matrix **A** does not change as in the case of the update of **H** only. The correlation matrix is constant during the external loops.

In this configuration as for the update of **H** only, if there exists non-linearities of **H**, they shall no longer interfere with the analysis at the end of the external loops. So this may indicate that both parameters D and a have correlated errors in addition of being antiparallel. However, this needs to be confirmed by further investigations as these coefficients have a different physical meaning.

This dual calibration shows that it is feasible to calibrate multiple control parameters for fire applications in the context of OSE, especially if the observations have a significant weight in the determination of the optimal solution. A special attention shall be given, however, to the modeling of the background error covariance matrix **B** and of the error correlations.

However, as a review of the literature has highlighted, the propagation of a fire at a macroscopic scale can be identified as a wave front, whose main feature is its rate of spread. The idea is therefore to build an assimilation prototype with the speed as control parameter. The calibration of D and a was only a first step to reach this objective. A similar data assimilation study could be performed with s_L as model parameter using the fire spread model presented in chapter 6.

8.2 Assimilation of the speed parameter of the model

In this section, a data assimilation prototype is built using the fire spread model with the PDE of the progress variable c and thus, assimilating measurements of c at fixed spatial locations over the computational domain. In this context of OSE, it calibrates one single control parameter, the constant of proportionality

$s_{L,KPP}$ between the velocity field and the vegetation distribution satisfying $s_L(x,y) = s_{L,KPP} \times Y(x,y)$. Different vegetation configurations will be tested for this assimilation process: a Gaussian distribution on the one hand, a random distribution on the other hand. In any case, the vegetation field does not change during the model integration, the fuel consumption is not taken into account, meaning that Y is an input data representing a fuel mapping.

8.2.1 Steps in the data assimilation process

In this study, the data assimilation algorithm is the same as for the calibration of D in chapter 7.

The true control parameter is fixed to $\mathbf{x}^t = s^t_{L,KPP} = 0.1$. The true trajectory results from the integration of the fire model using this constant coefficient to establish the velocity field $s_L(x,y)$. From this true trajectory are directly extracted the artificial observations with a prescribed frequency f in space and time. Noise is introduced, following a Gaussian distriburion, whose standard deviation is calculated as a percentage of the mean value of the true field $H(\mathbf{x}^t)$. As previously, it is assumed that observation errors are not correlated, and so $\mathbf{R}$ is reduced to a diagonal matrix.

The background control parameter $\mathbf{x}^b = s^b_{L,KPP}$ is specified as a perturbation of the true control parameter The standard deviation is indeed prescribed as a percentage of $s^t_{L,KPP}$, and is used to build the error covariance matrix $\mathbf{B}$ (which is a scalar as there is a single control parameter). In this study, $s^b_{L,KPP} = 0.11$, meaning that the front is assumed to propagate too rapidly. The integration of the fire model $M(s^b_{L,KPP})$ provides the background trajectory and then, applying the selection operator S leads to the formulation of the term $H(\mathbf{x}^b)$.

The quality of the tangent linear of the observation operator H, denoted by $\mathbf{H}$, is highly sensitive to the perturbation $\delta\mathbf{x}^b$ of the background due to the non-linearity of H. However, the validity of $\mathbf{H}$ was verified along the speed interval $[0.10; 0.11]$.

Using the background $\mathbf{x}^b$, the observation vector $\mathbf{y}^o$, the equivalent of the background in the observation space $H(\mathbf{x}^b)$, the linear tangent $\mathbf{H}$, and the error covariance matrices $\mathbf{B}$ and $\mathbf{R}$, the BLUE algorithm is able to produce the analysis $\mathbf{x}^a$. A classical diagnostic consists in verifying that $\mathbf{x}^a$ is closer to $\mathbf{x}^t$ than $\mathbf{x}^b$, and also that the RMS of the distance between the observations and the analysed trajectory is reduced compared to the distance between the observations and the background trajectory. As this study is performed in an OSE context, $\mathbf{x}^t$ is assumed to be known, and therefore the analysis shall also ensure that the RMS of the distance between the true and analysed trajectories is reduced compared to the distance between the true and background trajectories.

8.2.2 Gaussian fuel distribution

The 2D fire spread model has been validated for a plane as well as for a Gaussian vegetation distribution in section 6.2.3. For these different distributions, the diagnostics of the flame properties, speed and thickness, proved the consistency of the model with the macroscopic scale at which the fire propagation is studied. So the behavior of the data assimilation prototype is, in a preliminary investigation, analyzed for an elliptical Gaussian vegetation distribution, illustrated in figure 8.3 and defined as:

$$Y(x,y) = \exp\Big(\frac{(x-100)^2}{2\sigma_x^2} + \frac{(y-100)^2}{2\sigma_y^2}\Big)$$

with $\sigma_x = 40$ and $\sigma_y = 20$.

Analysis as a function of the observation uncertainty

In this study, the level of confidence in the background is assumed to be constant, $\mathbf{x}^b = 0.11$ is fixed and thus, $\mathbf{B} = 10^{-4}$ is constant. Different assimilations are performed, each assimilation is associated to a different observation uncertainty even though the observation frequency is fixed to $f = 96$ in space and time (leading to 64 observations over the time window $[0; 800]$, equivalently 4 observations at each of the 16

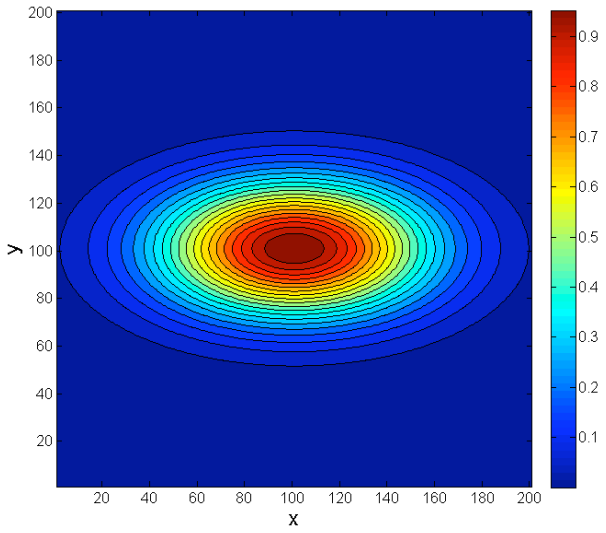

Figure 8.3: Gaussian vegetal fuel distribution over the computational domain.

observational times). This means that the parameter of this study is the error percentage α_o . Results are presented in table 8.6.

Error percentage α_o	0.01	0.1	0.2	0.5	1	5	10
Observation variance σ^o	6×10^{-6}	6×10^{-4}	2×10^{-3}	1×10^{-2}	6×10^{-2}	1.4	5.8
Analysis $\mathbf{x}^a$	0.0994	0.0985	0.1004	0.1054	0.1078	0.1096	0.1098
Analysis variance $\mathbf{A}$	2×10^{-7}	2×10^{-5}	4×10^{-5}	9×10^{-5}	1×10^{-4}	1×10^{-4}	1×10^{-4}
RMS$(H(\mathbf{x}^t) - H(\mathbf{x}^b))$	4×10^{-2}	4×10^{-2}	4×10^{-2}	4×10^{-2}	4×10^{-2}	4×10^{-2}	4×10^{-2}
RMS$(H(\mathbf{x}^t) - H(\mathbf{x}^a))$	2.5×10^{-3}	6×10^{-3}	2×10^{-3}	2×10^{-2}	3×10^{-2}	4×10^{-2}	4×10^{-2}
DFS	0.99	0.84	0.57	0.17	0.05	0.002	0.0005

Table 8.6: Analysis results for an elliptical Gaussian vegetation distribution for $f = 96$ fixed.

Three scenarii can be identified in these results: 1. when a high confidence is prescribed on the background; 2. when a high confidence is prescribed on the observations; and 3. when an equivalent confidence is prescribed on the background and on the observations.

For scenario 1, the information on the background is predominant and the information from the observation has a negligible impact on the analysis, that remains close to the background. For instance, for $\sigma_o = 6 \times 10^{-2}$, $\mathbf{x}^a = 0.1096$. The analysed and background front positions are therefore superposed at any time, notably for $t = 800$ in figure 8.4(a). The associated state variables c are very similar as figure 8.4(b) shows. In the opposite, in scenario 2, the confidence in the observations is predominant, so the analysis is close to the true value. For instance, for $\sigma_o = 6 \times 10^{-6}$, $\mathbf{x}^a = 0.0994$, the analysed trajectory is superposed to the true trajectory as shown in figures 8.5(a) and 8.5(b). Note that the analysis is outside the interval $[\mathbf{x}^t; \mathbf{x}^b]$ because of the impact of the non-linearities of H (the linear tangent is computed in the vicinity of the background), but the algorithm still exhibits a consistent behavior. Finally, in scenario 3, when the confidence in the background and in the observations are equivalent, the analysis is between $\mathbf{x}^t$ and $\mathbf{x}^b$, so the simulated state is an intermediate state. For instance, for $\sigma_o = 1 \times 10^{-2}$, $\mathbf{x}^a = 0.1054$ and the analysed front position is located half way from the background and true front positions in figure 8.6(a), similarly as the analysed progress variable c in figure 8.6(b).

In general, these result show that when the error variance σ_o on the observation decreases, the analysis varies from the background $\mathbf{x}^b = 0.11$ towards the true control parameter $\mathbf{x}^t = 0.10$. Consistently, the DFS for the ensemble of the observations on the assimilation window increases from 0 to 1, meaning that the contribution of the observations also increases. For instance, for scenario 1 the DFS is very low (DFS = 0.002 for $\mathbf{x}^a = 0.1096$) as the background contribution is predominant in this case, while for scenario 2 the DFS

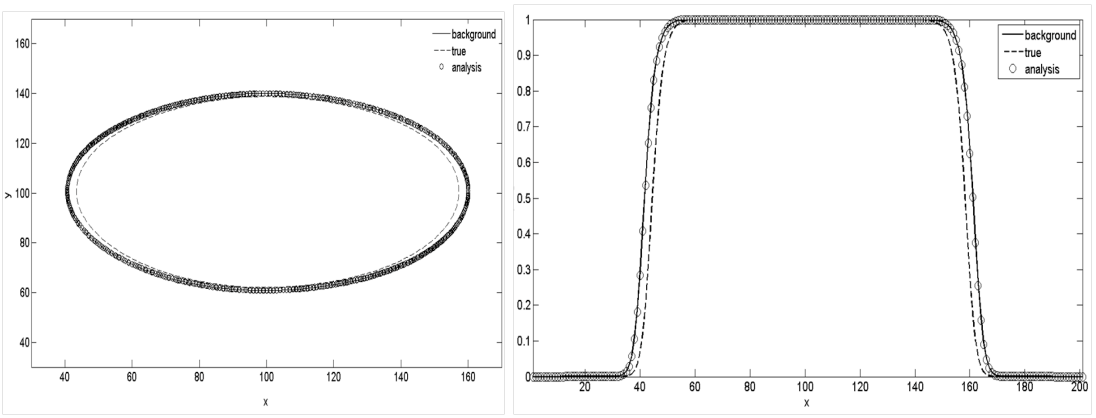

(a) Position of the front (b) Progress variable c along the x-axis for $y = 100$

Figure 8.4: Scenario 1 - Instantaneous position of the front (a) and profile of the progress variable c (b) at $t = 800$, with the true trajectory in dashed line, the background trajectory in solid line and the analyzed trajectory in circle line.

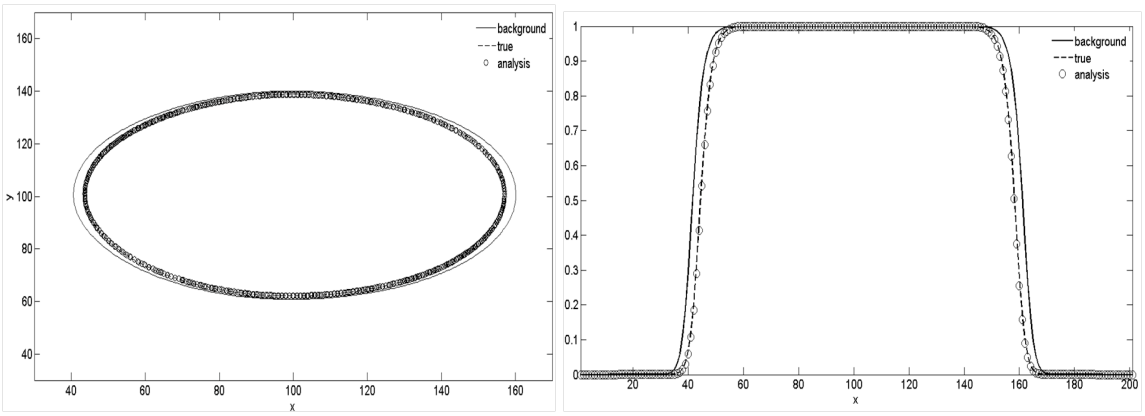

(a) Position of the front (b) Progress variable c along the x-axis for $y = 100$

Figure 8.5: Scenario 2 - Instantaneous position of the front (a) and profile of the progress variable c (b) at $t = 800$, with the true trajectory in dashed line, the background trajectory in solid line and the analyzed trajectory in circle line.

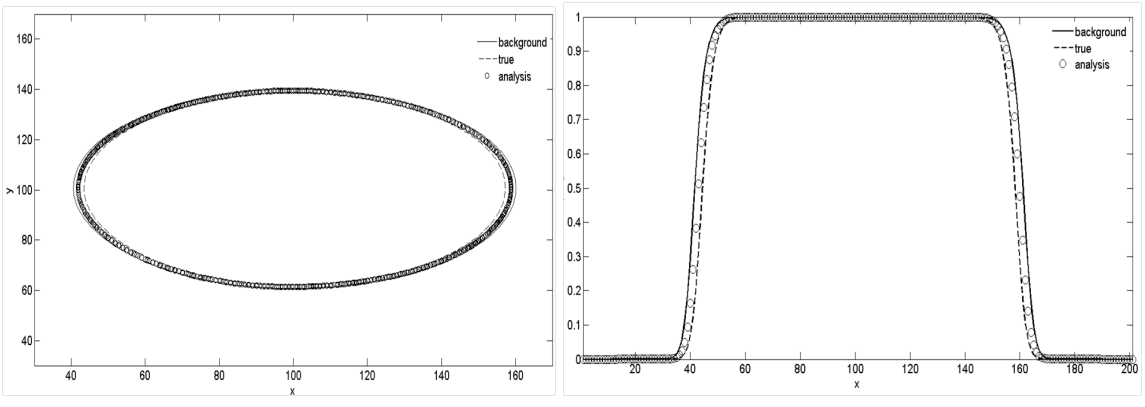

(a) Position of the front (b) Progress variable c along the x-axis for $y = 100$

Figure 8.6: Scenario 3 - Instantaneous position of the front (a) and profile of the progress variable c (b) at $t = 800$, with the true trajectory in dashed line, the background trajectory in solid line and the analyzed trajectory in circle line.

is almost 1 (DFS = 0.99) meaning that the background has no significant influence on the analysis, the observation contribution is predominant. Furthermore, there is a systematic reduction of the analysis error compared to the background error as $\mathbf{A} < \mathbf{B}$: this implies an analysis parameter closer to the true parameter in the control space, and an analysed trajectory closer to the true trajectory than the background trajectory in the observation space (with $\mathrm{RMS}(H(\mathbf{x}^t) - H(\mathbf{x}^a)) < \mathrm{RMS}(H(\mathbf{x}^t) - H(\mathbf{x}^b))$ for all assimilation configurations).

Analysis as a function of the observation frequency

The previous series of assimilation (presented in table 8.6) was carried out for a fixed observation frequency of 96 in space and time. The objective in a second step is to check how the analysis behaves if this frequency is changed. The following study is performed with $f = 32$ (meaning that $p = 1800$ observations are assimilated along the assimilation window $[0; 800]$). As previously, the background uncertainty is fixed with $\mathbf{x}^t = 0.10$, $\mathbf{x}^b = 0.11$ and thus, $\mathbf{B} = 10^{-4}$.

The analysed trajectory in the control space when the observation variance σ_o varies is compared between $f = 32$ and $f = 96$ in figure 8.7. The analysis follows the same trend for both frequencies when the level of confidence in the observations increases: the analysis moves from the background control parameter $\mathbf{x}^b = 0.11$ when the background is predominant towards the true control parameter $\mathbf{x}^t = 0.10$ when the observation variance decreases. However, the curves for $f = 32$ and $f = 36$ are slightly different. Firstly, it is clear that the analysis moves faster towards the true parameter for $f = 32$ than for $f = 96$: in other words, for a given observation variance, the analysis is much closer to the true parameter for $f = 32$ than for $f = 96$. For instance, for $\sigma_o = 10^{-1}$, while $\mathbf{x}^a \approx 0.1025$ for $f = 32$, $\mathbf{x}^a \approx 0.108$ for $f = 96$. This discrepancy between both frequencies is significant along the interval $\sigma_o \in [10^{-3}; 1]$. Indeed, the difference in the analysis is almost negligible for an observation variance below 10^{-3}.
Secondly, while the non-linearities interfere in the assimilation for $f = 96$ as the analysis is outside the interval $[\mathbf{x}^t; \mathbf{x}^b]$ for $\sigma_o < 10^{-3}$, it is not the case for $f = 32$. Indeed, the analysis stays in the interval and converges consistently towards the true control parameter when the level of confidence in the observations is higher and higher.
This difference in the behavior of the data assimilation algorithm is due to the number of observations taken into account by the BLUE, while there is a single control parameter to calibrate. Indeed, when there are numerous observations with a relatively high uncertainty, they can have a significant influence on the analysis as each observation carries some information which can be critical for the assimilation once agregating all together. As a consequence, the 1800 observations subject to a high uncertainty can, in some configurations, have a larger contribution to the analysis than the 64 observations with a lower uncertainty. The result shows that there is, however, a threshold to this phenomenon.

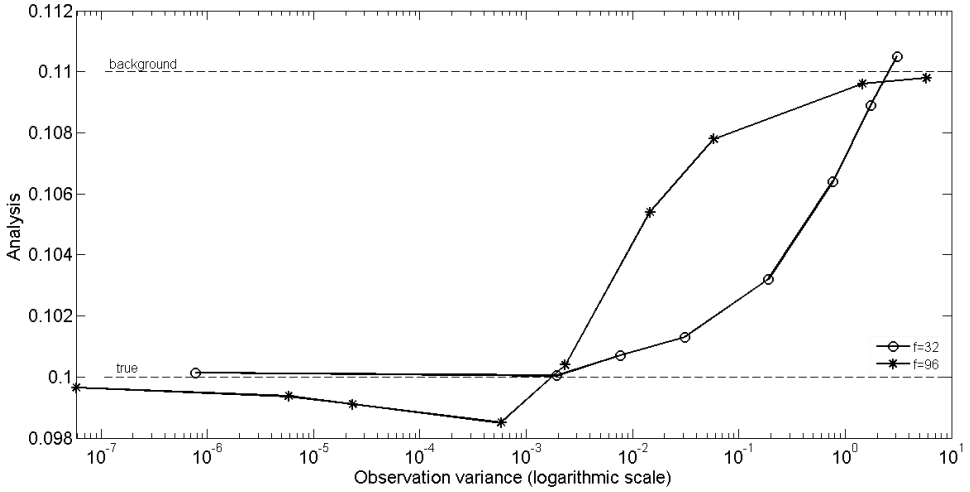

Figure 8.7: Analysis in the control space as a function of the observation variance σ_o (logarithmic scale) - Comparison for two different observation frequencies $f = 96$ ($p = 64$) and $f = 32$ ($p = 1800$).

So as to confirm this statement, another assimilation configuration is tested. As previously, the background uncertainty is fixed to $\mathbf{B} = 10^{-4}$ with $\mathbf{x}^t = 0.10$ and $\mathbf{x}^b = 0.11$. However, the observation variance is also fixed to $\mathbf{R} = 10^{-4}$. The only parameter of the study is therefore the number of observations p taken into account in the assimilation via the choice of the observation frequency f. Results are presented in table 8.7.

Obs. frequency f	Number of observations p	Analysis $\mathbf{x}^a$	Uncertainty $\mathbf{A}$
32	1800	0.10014	3.1×10^{-9}
64	225	0.09996	1.7×10^{-8}
96	64	0.0996	3.2×10^{-6}
101	15	0.1097	9.9×10^{-5}

Table 8.7: Analysis results for an elliptical Gaussian vegetation distribution for different observation frequencies f.

They show that the more observations, the higher the level of confidence in the analysis. This is consistent with data assimilation: when there are more assimilated observations, the algorithm is able to capture more information on the system and thus, to correct with a better accuracy the control parameter. As previously, it appears that the non-linearities interfere more likely with the assimilation when the number of assimilated observations p decreases, or equivalently when the observation frequency f increases. Indeed, for $f = 64$ and $f = 96$, the analysis is not closer to $\mathbf{x}^b$ than for $f = 32$, but it is located outside the interval $[\mathbf{x}^t; \mathbf{x}^b]$. This can be explained simply. The importance of the non-linearities is highly correlated to the position of the assimilated observations over the computational domain. When the observation frequency increases, the assimilated observations are more sparse over the domain. So an important proportion of these observations can be ahead of the fire front in the zone where the progress variable c is low, and therefore where the non-linearities start to become significant. In the opposite, when the observation network is denser, there are more observations (in proportion) located in the vicinity of the front or inside the front, and so these observations can provide important information to the assimilation, avoiding the non-linearities as they have a higher contribution to the analysis as highlighted by the DFS study. Finally, the table 8.7 confirms that for a fixed observation and background variance, the frequency f has a direct impact on the analysis as for $f = 101$ the analysis is close to $\mathbf{x}^t$, while for all the others the analysis remains close to $\mathbf{x}^t$.

8.2.3 Random fuel distribution

The behavior of the data assimilation prototype is also studied for a random vegetation distribution. In this case, the vegetation is assumed to be randomly spread: Y is the superposition of 1,000 randomly spread fuel pockets with a random intensity (between 0 and 1) over the computational domain as presented in figure 8.9.

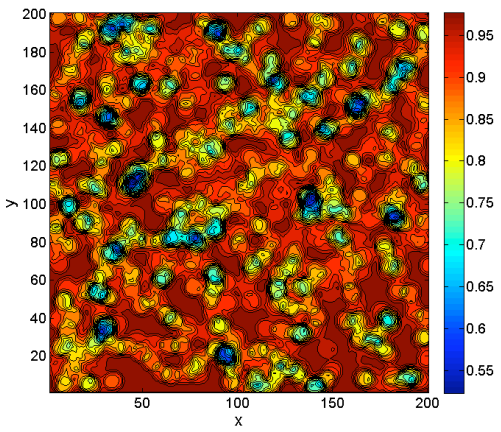

Figure 8.8: Random vegetal fuel distribution over the computational domain.

Different analyses are performed for different confidences in the observations. The observation frequency is $f = 96$ in space and time, leading to 64 observations over the time window $[0; 800]$ (or equivalently, 4 observations at each of the 16 observational times). It is assumed that the confidence in the background is constant, so $\mathbf{B}$ is constant ($\mathbf{B} = 10^{-4}$) and $\mathbf{x}^b = 0.11$ does not change. Results are presented in table 8.8.

Observation variance σ^o	6×10^{-6}	6×10^{-4}	1×10^{-2}	6×10^{-2}	2×10^{-1}	1
Analysis $\mathbf{x}^a$	0.0995	0.0988	0.1054	0.1079	0.1090	0.1096
Analysis variance $\mathbf{A}$	2×10^{-7}	1×10^{-5}	8×10^{-5}	9×10^{-5}	9×10^{-5}	1×10^{-6}
RMS$(H(\mathbf{x}^t) - H(\mathbf{x}^b))$	1×10^{-1}	1×10^{-1}	1×10^{-1}	1×10^{-1}	1×10^{-1}	1×10^{-1}
RMS$(H(\mathbf{x}^t) - H(\mathbf{x}^a))$	7×10^{-3}	1×10^{-2}	6×10^{-2}	9×10^{-2}	1×10^{-4}	1×10^{-1}
DFS	0.99	0.85	0.188	0.05	0.01	0.002

Table 8.8: Analysis results for a random vegetation distribution.

As for the Gaussian vegetation distribution, the data assimilation algorithm exhibits a consistent behavior as the analysis satisfies the diagnostics in terms of uncertainty, average distance with the true state and DFS. The three scenarii can be identified (presented in figure 8.9). Scenario 1 is typically obtained for $\sigma^o = 2 \times 10^{-1}$ with $\mathbf{x}^a = 0.1098$, a parameter which remains close to $\mathbf{x}^b = 0.11$. In the opposite, in scenario 2, the analysis is close to the true value as for $\sigma^o = 6 \times 10^{-6}$, $\mathbf{x}^a = 0.0995$. Finally, in scenario 3, when the confidence is similar in the background and observations, the analysis is between $\mathbf{x}^t$ and $\mathbf{x}^b$, so the simulated state is an intermediate state (for $\sigma^o = 1 \times 10^{-2}$, $\mathbf{x}^a = 0.1054$).

Conclusion

For all the experiments presented in this section, the data assimilation algorithm exhibits a consistent behavior. When the level of confidence in the observations increases, the analysis varies from the background $\mathbf{x}^b = 0.11$ towards the true control parameter $\mathbf{x}^t = 0.10$. Consistently, the DFS for the ensemble of the observations on the data assimilation window increases from 0 to 1, meaning that the contribution of the observations also increases.

For all these experiments, with a Gaussian as well as with a random vegetal fuel distribution, the behavior of the data assimilation algorithm is validated, both in the control and observation space. First of all, there is a systematic reduction of the analysis error compared to the background error. Secondly, the RMS of the distance between the true and analysed trajectories is in every case lower than the RMS of the distance between the true and background trajectories. These two diagnostics mean that the uncertainty in the analysed front position is reduced compared to the background and to the observations, providing a better estimation than if either source of information were taken separately.

In this work, the uncertainty of the model formulation is investigated as the background error is assumed to be totally included in the uncertainty of the constant parameter $s_{L,KPP}$. However, the input data such as the vegetation distribution could also be subject to some uncertainties and furthermore, the relation between the rate of spread and the vegetation distribution may not be linear. In future investigations, the formulation of the rate of spread could therefore be complicated such that:

$$s_L(x, y) = s_{L,KPP}\, Y(x, y)^n$$

with the introduction of a new parameter n and of an unknown in the vegetation distribution Y such that $Y = Y_0 + Y^{'}$ (with Y_0 known and $Y^{'}$ unknown). In this new configuration, the algorithm could assimilate both parameters n and $s_{L,KPP}$ as well as the unknown field $Y^{'}$.

In general, this study demonstrates that some of the limitations of wildland fire modeling can be overcome by coupling information from observations and models, and that a data-driven fire model can lead to more accurate predictions of fire spread. This preliminary work is limited to a stand-alone numerical feasibility study, however these results show that this strategy could provide a valuable solution to the problem of integrating fire sensor observations into fire models. This data assimilation prototype considered observations at fixed locations over the area subject to a fire, but in reality this zone may be covered by satellite or airplanes

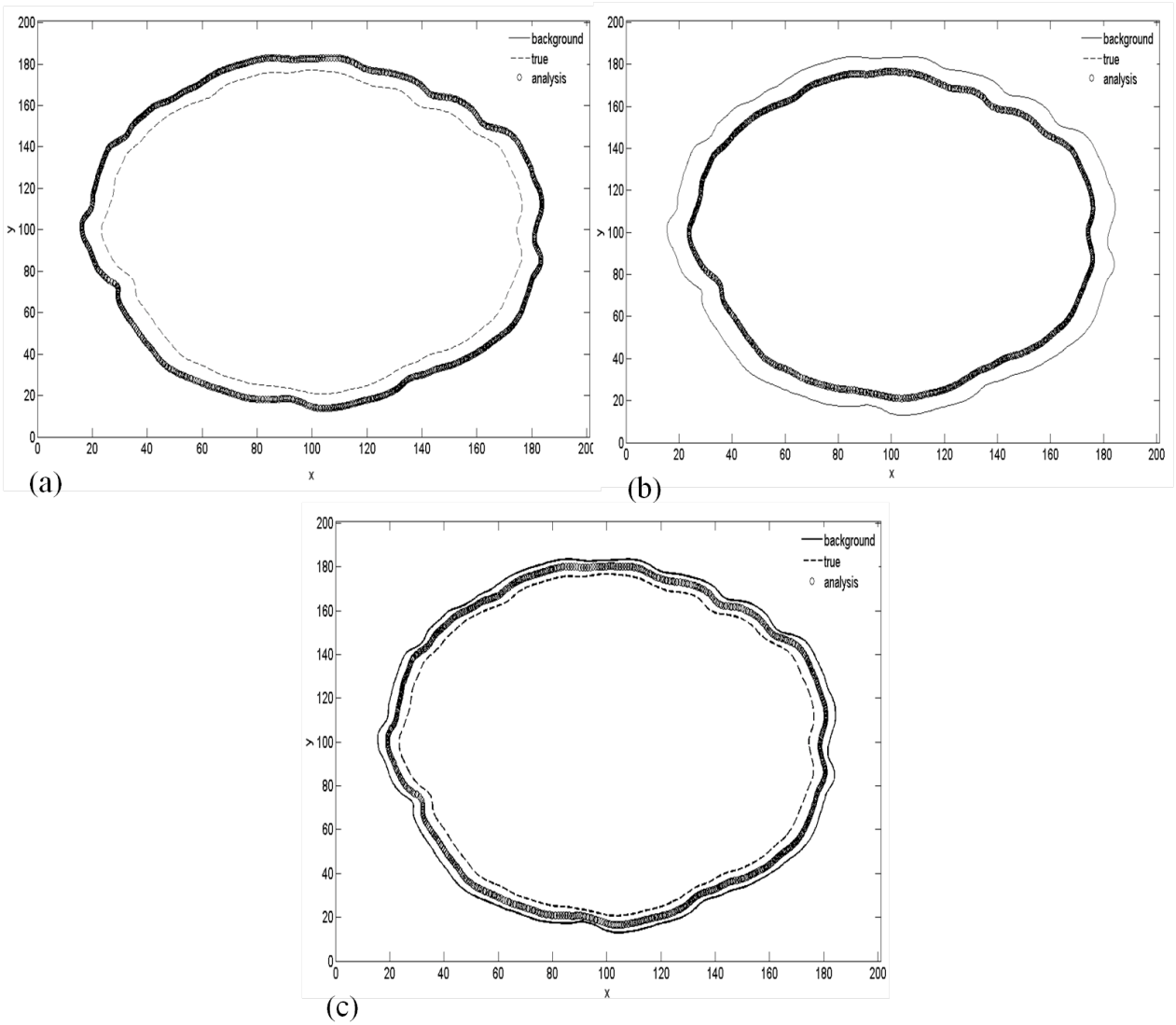

Figure 8.9: Position of the simulated front at $t = 800$ with the true parameter in dashed line, the background parameter in solid line and the analysed parameter in circle line (a) Scenario 1: when a high level of confidence is prescribed on the background (b) Scenario 2: when a high level of confidence is prescribed on the observations (c) Scenario 3: when an equivalent confidence is prescribed on the background and on the observations.

so that it could also integrate dynamical data like time-evolving locations of the fire front. The next chapter will therefore investigate how to adapt the data assimilation methodology to be able to consider multiple sources of observations.

9. Exploration of the Lagrangian Technique

As fire observations are made at time-evolving locations along the flame front in practice, the Lagrangian assimilation may appear as a powerful alternative to calibrate the speed parameter of the propagation model presented in chapter 6. With this technique, the trajectory of the background front is computed using the motion of a set of particles over time, instead of solving the reaction-diffusion PDE model [29][30]. However, this PDE model is used to produce the observations of the fire front, necessary in the OSE context. As a demonstration-of-concept, this methodology has been tested for a 1D configuration, where a single particle represents the front position.

9.1 Motivations

The exploration of this Lagrangian technique has been motivated by different factors:

- The evolution of the fire front is highly dependent upon the local amount of fuel, so its shape may vary drastically over the computational domain if the vegetation distribution is not homogeneous. A Lagrangian technique could therefore appear as a powerful tool to detect and track the local features of the multiple heads of the fire. The idea is to introduce more particles in these critical zones, where a large part of the information on the system dynamics is confined.
- Observations of the fire are provided by firefighters but also by satellite images. In the latter, the sequence of images obtained during the assimilation window gives information on the dynamical evolution of the fire front. These images of the front at different times can be considered as Lagrangian data.
- In the Eulerian approach of data assimilation, the analysis is highly sensitive to the non-linearities of the observation operator with respect to the control parameters. In the opposite, the Lagrangian observation operator which deduces the position of the particles from the velocity field shall be linear. So a Lagrangian technique may appear as a solution to overcome the issue with the non-linearities of H.

9.2 Principles

9.2.1 Observations in the context of OSE

As in the Eulerian approach, the objective of the Lagrangian assimilation is to calibrate the constant speed parameter $s_{L,KPP}$ for an isotropic vegetation distribution. Unlike the Eulerian approach, the data assimilation does not consider temperature measurements but the successive positions of the front as observations.

More precisely, in this proof-of-concept, the successive observed positions of the fire front $\mathbf{Y}^o$ are provided by the fire spread model which is integrated for the true value of the KPP speed, denoted by $s^t_{L,KPP}$. The integration of this Eulerian model gives primarily the field c at each time step, assuming the initial condition of the fire is perfectly known (at time t_0). The initial position of the front is denoted by $x_{c,0}$. As the study is performed in a one-dimensional case, the fire front is represented by a single point whose position over time, denoted by $x_{c,t}$, corresponds to $c(x_{c,t}) = 0.5$.

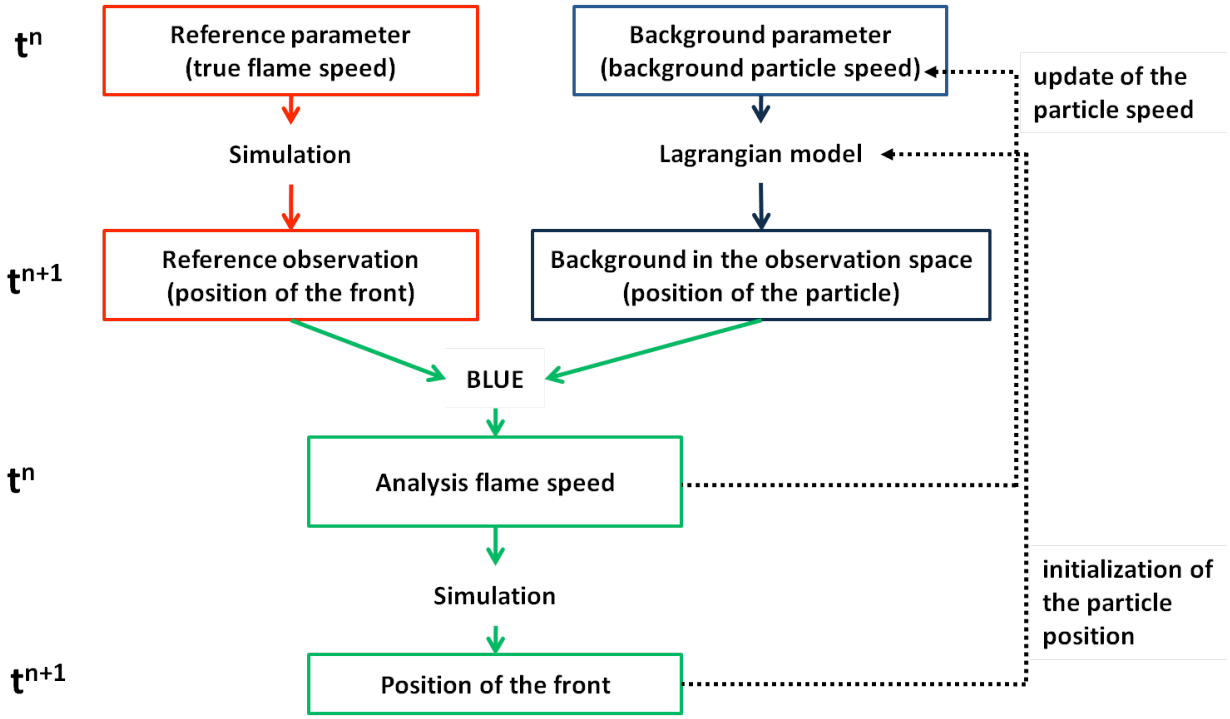

Figure 9.1: Schematic representation of the algorithm of Lagrangian data assimilation.

This configuration of data assimilation does not define a rigorous framework for OSE in the sense that observations are directly extracted from the true trajectory. No noise is introduced. However, $\mathbf{R}$ is not a zero matrix. The observation uncertainty is fixed in terms of the mesh size ($\sigma_o = \alpha_o \times \Delta x$, with α_o a parameter), so as to measure the uncertainty in the position of the observation with respect to the grid.

9.2.2 Background with the Lagrangian model

To apply a data assimilation algorithm, a modeled position of the fire front is required. The speed $s_{L,KPP}$ is the control parameter, so a background value $s^b_{L,KPP}$ is introduced as a perturbation of $s^t_{L,KPP}$, with $\sigma_b = \alpha_b \times s^t_{L,KPP}$ and α_b a parameter such that:

$$s^b_{L,KPP} = s^t_{L,KPP} + \sigma_b \tag{9.1}$$

Starting from the same initial condition $x_{c,o}$ at time t_0 as for the observations, the modeled position $x_{c,b}$ of the front is established at time t using a Lagrangian transport model defined by the set of equations (9.2):

$$\begin{cases} \frac{dx_{c,b}(t)}{dt} = s^b_{L,KPP} \\ x(t_0) = x_0 \end{cases} \tag{9.2}$$

This position of the particle at time t, denoted by $x_{c,b}(t)$, represents the equivalent of the background parameter $s^b_{L,KPP}$ in the observation space. In other words, $x_{c,b} = H(s^b_{L,KPP})$ with H the Lagrangian observation operator.

9.2.3 Lagrangian observation operator

The BLUE algorithm requires the linearization of H in the vicinity of the background parameter. A perturbed position of the particle $x_{c,b}$ is computed by introducing a perturbation to the background control parameter $s^b_{L,KPP}$ (denoted by $\delta s^b_{L,KPP}$) and then by solving the associated Lagrangian transport model. Hence,

$$\mathbf{H} = \frac{\tilde{x}_{c,b} - x_{c,b}}{\delta s^b_{L,KPP}} \tag{9.3}$$

In the context of a constant rate of spread at a given time, it is easy to show that $\mathbf{H}$ is exactly equal to the elapsed time $(t - t_0)$ between two observations. In other words, $\mathbf{H}$ is given by the time step associated to the Lagrangian model. This also means that $\mathbf{H}$ has a time unit as it maps a control variable from the speed space onto the position space.

9.2.4 The BLUE resolution

At the initial time of the assimilation t_0, a modeled position of the fire front $H(\mathbf{x}^b) = x_{c,b}$ is provided as well as an observed position $\mathbf{y}^o = x_{c,t}$. The observation operator is defined, so are the error covariance matrices $\mathbf{R}$ and $\mathbf{B}$. Both error covariance matrices do not have the same unit: $\mathbf{R}$ is defined in terms of distance, $\mathbf{B}$ in terms of speed. So as to compare both quantities, $\mathbf{R}$ needs to be divided by the square of the tangent linear of the observation operator $\mathbf{H}$.

The BLUE determines the optimal solution $\mathbf{x}^a = s^a_{L,KPP}$ of the speed parameter at time t_0, by using the discrepancy between the two positions of the fire front $\text{OMB} = \mathbf{y}^o - H(\mathbf{x}^b)$. As in the Eulerian approach, the analysis can be considered as a correction of the background. In this framework, $\mathbf{x}^a$ represents a speed correction of the front at time t_0.

With this technique, the parameter calibration is performed at an instantaneous time with one single observation and one background control parameter. The resulting analysis is then used to update the model parameters for the next data assimilation time:

- The speed parameter of the Lagrangian transport model is updated with $s^a_{L,KPP}$.
- The initial position of the front $x_{c,0}$ is updated with the position of the analysed front at time t (this position results from the integration of the fire spread model from t_0 to t with $s^a_{L,KPP}$ as parameter of the model and from the identification of the location at which $c = 0.5$ is satisfied).

This update of the background parameters are schematized in figure 9.2. In this prototype, there is no update of the background error covariance matrix $\mathbf{B}$: it appears as a reasonable choice as the initial position of the front $x_{c,0}$ at each integration of the Lagrangian model is computed using the model and is therefore subject to similar uncertainties as in the previous assimilation iterations.

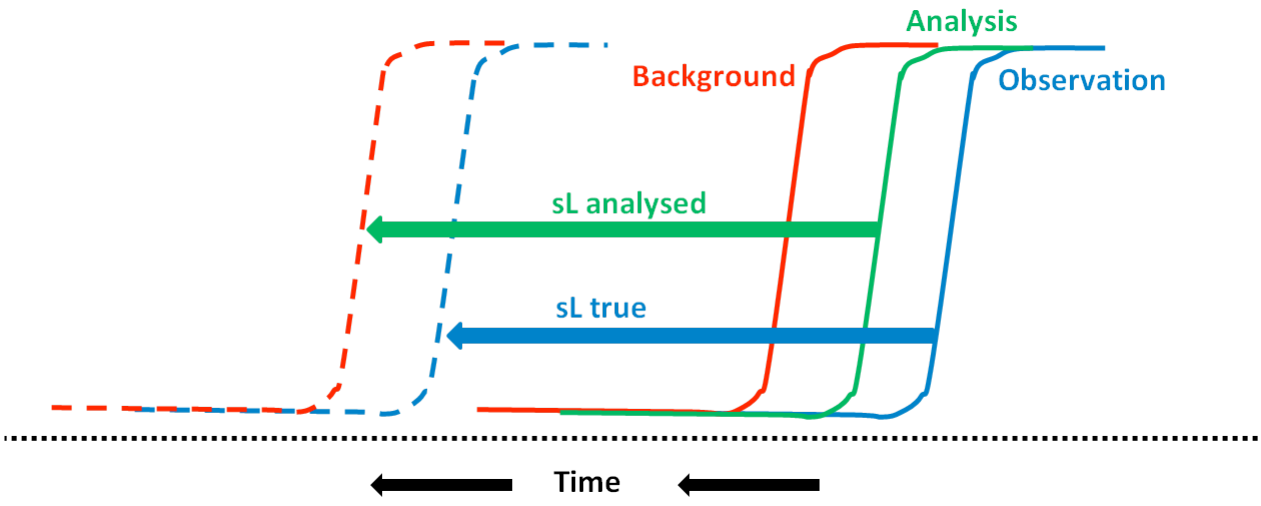

Figure 9.2: Schematic representation of the update of the background parameters with the analysis from the previous assimilation iteration.

This sequential assimilation is schematized in figure 9.1. This approach is consistent as in future investigations the speed parameter of the Lagrangian transport model will not be the KPP constant, but instead it will change over time depending on the vegetal fuel distribution over the computational domain.

9.3 Feasibility of the Lagrangian approach

The feasibility of the Lagrangian data assimilation is shown for the fire spread model in 1D with an isotropic fuel distribution. In the course of its integration, it has been underlined that the system reaches the KPP speed after a transient state, whose length depends on the thickness numerical parameter β. This parameter is set to $\beta = 1.2$ so as to have an accurate speed of the observed front and thus an accurate position of the observed front. The Lagrangian assimilation shall start once this permanent regime is reached so as to get consistent front positions. The assimilation starts at $t_0 = 600$ and lasts until $t = 800$. $s^t_{L,KPP} = 0.1$.

9.3.1 Assimilation at each model time step

Observations $\mathbf{y}^o$ are produced by integrating the Eulerian model with the progress variable c as state variable. There is therefore one observation of the system at each time step (each $\Delta t = 0.5$). The initial configuration of the background at $t_0 = 600$ is defined by the true state associated to $s^t_{L,KPP} = 0.1$, so the particle position corresponds to the position of the observation at $t_0 = 600$, and the background field is equal to the true field until t_0.

An assimilation is carried out at $t_0 = 600$ for different values of the background control parameter $s^b_{L,KPP}$ (and therefore for different background uncertainties) and for different levels of confidence in the observations (via the definition of α_o). In table 9.1, only one assimilation iteration at $t_0 = 600$ is presented so as to give a first insight on the algorithm behavior. From these results, the algorithm appears to be consistent with the data assimilation requirements:

1. in terms of uncertainty: $\mathbf{A} < \mathbf{B}$ and $\mathbf{A} < \mathbf{R}$,
2. in terms of control parameter: $s^t_{L,KPP} < s^t_{L,KPP} < s^b_{L,KPP}$,
3. in terms of diagnostics: RMS(AMO) < RMS(BMO), and the DFS show that the observation contribution decreases when the level of confidence in the background increases.

Case	α_b	α_o	$\mathbf{B}$	$\mathbf{R}$	$s^a_{L,KPP}$	$\mathbf{A}$	RMS(BMO)	RMS(AMO)	DFS(obs)
A	0.10	0.01	10^{-4}	10^{-4}	0.1077	8×10^{-5}	5.7×10^{-3}	3.8×10^{-3}	0.2
B	0.10	0.20	4×10^{-2}	10^{-4}	0.1099	1×10^{-6}	5.7×10^{-3}	4.9×10^{-3}	6×10^{-4}
C	0.10	0.50	0.25	10^{-4}	0.1099	1×10^{-6}	5.7×10^{-3}	4.9×10^{-3}	10^{-6}
D	0.20	0.20	4×10^{-2}	4×10^{-4}	0.1199	4×10^{-4}	1.1×10^{-2}	9.8×10^{-3}	2×10^{-3}

Table 9.1: Lagrangian results for one assimilation iteration at $t_0 = 600$. $s^t_{L,KPP} = 0.1$, while the background parameter depends on the uncertainty: $s^b_{L,KPP} = 0.11$ for cases A, B, C; $s^b_{L,KPP} = 0.12$ for case D.

The evolution of the analysis over time is represented for one particular case, the case D presented in table 9.1 and visualized in figure 9.3. It is clear that the control parameter oscillates along the iterations, but these oscillations tend to be damped over time and to lead the analysis towards the true control parameter.

The presence of oscillations is justified by the process. The background overestimates the true value of the control parameter, so this means that the background front propagates too rapidly compared to the true front. As it is an instantaneous assimilation, the analysis speed needs to be reduced to slow down the front. In other words, if the background front is to superpose to the true front, then the speed of the propagation shall be reduced quite drastically so as to balance the advance pulled ahead of the true front. Then, at the next assimilation iteration, the background front may be too much slowed down, so the analysis speed has to be accelerated. If it is too much accelerated, the analysis shall be reduced again. This applies until the convergence towards the true speed is obtained. That is why, along the assimilation iterations, $s^a_{L,KPP}$ can be out of the interval $[s^t_{L,KPP}, s^b_{L,KPP}]$ with $s^a_{L,KPP} < s^t_{L,KPP}$. It may take several iterations to obtain an analysis converging towards the true control parameter without oscillations. It depends upon the uncertainties prescribed in the observations and in the background: the higher the confidence in the background, the longer it takes to the analysis to converge.

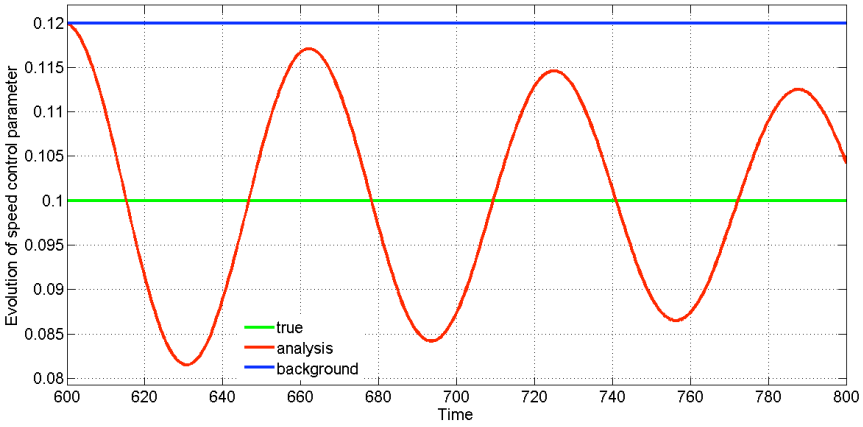

Figure 9.3: Evolution of the control parameter $s^a_{L,KPP}$ along the assimilation iterations, when observations are considered at each time step $\Delta t = 0.5$ from $t_0 = 600$ to $t = 800$ (case D). The blue line represents the initial value of $s^b_{L,KPP} = 0.12$ at t_0, while the red line corresponds to the constant value of $s^t_{L,KPP} = 0.10$ which is the true parameter in the context of OSE. The background value of $s^b_{L,KPP}$ varies along the iterations, it is not represented on the figure as it can be deduced from the analysis by shifting to the left (one time step) the analysed trajectory.

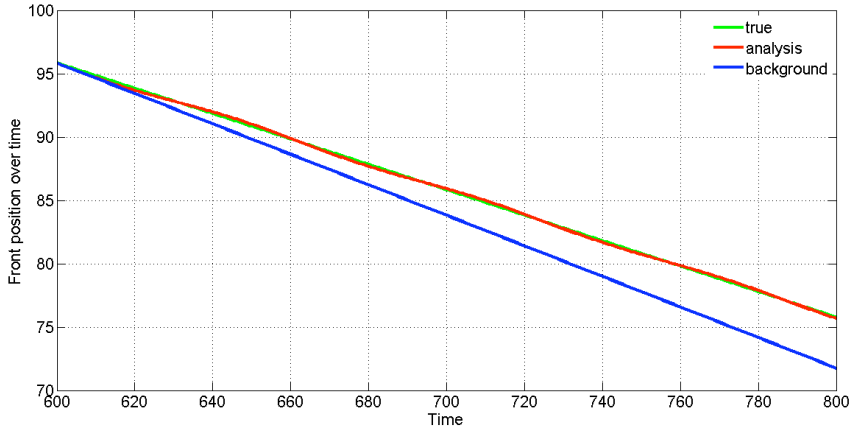

Figure 9.4: Evolution of the positions of the true front (green line), of the background front (blue line) and of the particle analysed position (red line) for case D. The background front corresponds to the integration of the front trajectory with $s^b_{L,KPP} = 0.12$ (the initial value of the background), representing the forecast of the position if there were no combination of information with the observations. The true trajectory is associated to $s^t_{L,KPP} = 0.10$.

9.3.2 Assimilation at the observation times only

A next stage in the investigation consists in carrying out data assimilation only at the observation times (the observation frequency over time is fixed as input parameter). The Lagrangian model is integrated with a time step corresponding to the elapsed time between two observations. In this study, the system is observed each 10 seconds, so the Lagrangian model is integrated with time steps of 10s.

As for the assimilation at each Eulerian time step ($\Delta t = 0.5$), the initial configuration of the background at $t_0 = 600$ is defined by the true state associated to the parameter $s^t_{L,KPP} = 0.1$, so the position of the particle corresponds to the position of the observation at $t_0 = 600$, and the background field is equal to the true field until t_0. An assimilation is carried out at $t_0 = 600$ for different values of $s^b_{L,KPP}$ and for different levels of confidence in the observations. Results are presented in table 9.2.

Case	α_b	α_o	**B**	**R**	$s^a_{L,KPP}$	**A**	RMS(BMO)	RMS(AMO)	DFS(obs)
A	0.10	0.01	10^{-4}	10^{-4}	0.10003	9.9×10^{-7}	0.10	3.1×10^{-4}	0.99
B	0.10	0.20	4×10^{-2}	10^{-4}	0.1080	8×10^{-5}	0.10	7.9×10^{-2}	0.2
C	0.20	0.10	10^{-2}	4×10^{-4}	0.1039	8×10^{-5}	0.20	3.89×10^{-2}	0.8
D	0.20	0.50	0.25	4×10^{-4}	0.1172	3.4×10^{-4}	0.20	0.17	0.14

Table 9.2: Lagrangian results for one assimilation iteration at $t_0 = 600$ for a time step of 10. $s^t_{L,KPP} = 0.1$, while the background parameter depends on the uncertainty: $s^t_{L,KPP} = 0.11$ for cases A, B; $s^b_{L,KPP} = 0.12$ for cases C, D.

As expected from the previous investigation, the assimilation diagnostics are consistent with the uncertainty prescribed in the observation and in the background. Along the iterations, oscillations on both sides of $s^t_{L,KPP}$ are also present in this configuration as figure 9.5 shows. However, they are smoother as the elapsed time between two observations is longer. For instance, for case B, the magnitude of the oscillations decrease faster: the system tends to stabilize faster towards $s^t_{L,KPP}$.

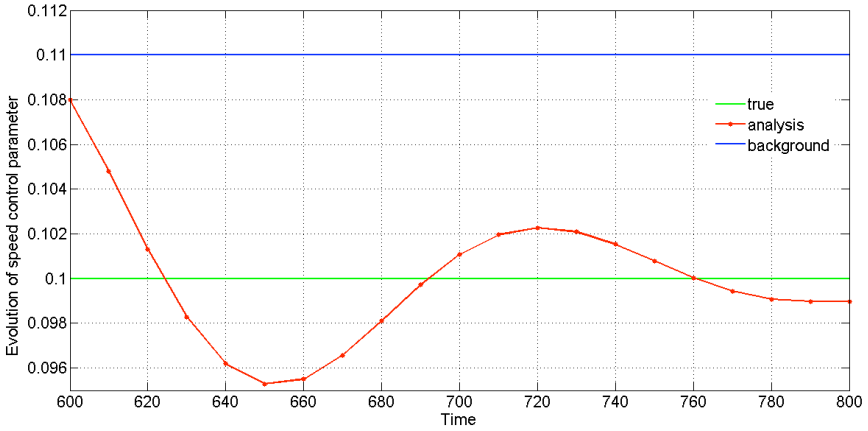

Figure 9.5: Evolution of the control parameter $s^a_{L,KPP}$ along the assimilation iterations, with an assimilation at each observation time step from $t_0 = 600$ to $t = 800$ (case B). The blue line represents the initial value of $s^b_{L,KPP} = 0.11$ at t_0, while the red line corresponds to the true parameter $s^t_{L,KPP} = 0.10$. The background value $s^b_{L,KPP}$ varies along the iterations, it is not represented on the figure as it can be deduced from the analysis by shifting to the left (one time step) the analysed trajectory.

For these configurations of Lagrangian assimilation, the error covariance matrices **R** and **B** stay constant along the assimilation iterations. One perspective would be to update **B** at each iteration so as to give more and more confidence to the background. This is consistent with the fact that at each iteration the analysis shall be closer to the true control parameter than to the background. It will be helpful to reduce the oscillating period of time. However, this update of **B** cannot be performed with the analysis error covariance matrix **A** as the position of the particle in the Lagrangian model is updated using the Eulerian model (with $s^a_{L,KPP}$ as model parameter). This introduces therefore some uncertainty which cannot be negligible and which will need to be analyzed in further investigations.

9.3.3 Generalization to a non-homogeneous fuel field

The Lagrangian prototype can be adapted to an anisotropic vegetation distribution. In this case, the speed in the Lagrangian model is not the KPP constant but the parameter $\bar{s}_L$ resulting from the spatial filtering in 1D. Otherwise, the algorithm stays the same to the homogeneous distribution of the vegetation, with constant matrices **B** and **R** along the iterations and an update of the position of the particle and of its velocity in the Lagrangian model using the result of the previous analysis.

As for the assimilation of the constant speed, the first analysis occurs at $t_0 = 600$, the observations which

represent the true state are produced for $s^t_{L,KPP} = 0.1$ and the initial value of the background depends on the perturbation in the true coefficient $s^t_{L,KPP}$. Results are presented in table 9.3.

Case	α_b	α_o	**B**	**R**	$s^a_{L,KPP}$	**A**	RMS(BMO)	RMS(AMO)	DFS(obs)
A	0.2	0.1	4×10^{-4}	10^{-2}	0.1089	2×10^{-4}	0.11	4.2×10^{-2}	0.48
B	0.1	0.5	1×10^{-4}	0.25	0.1098	1×10^{-6}	6.3×10^{-2}	4.7×10^{-2}	9×10^{-3}
C	0.1	1.0	10^{-4}	1	0.10998	1×10^{-6}	5.9×10^{-2}	2.9×10^{-2}	1×10^{-4}

Table 9.3: Lagrangian results for one assimilation iteration at $t_0 = 600$ for a time step of 10, with a vegetation dependence of the flame speed s_L. $s^t_{L,KPP} = 0.1$, while the background parameter depends on the uncertainty: $s^b_{L,KPP} = 0.12$ for case A; $s^b_{L,KPP} = 0.11$ for cases B, C.

These results show that this technique is feasible even though the flame speed is not constant and depends on the local amount of the vegetation. Indeed, the diagnostics (DFS and RMS(BMO)/RMS(AMO)) are consistent with the prescribed uncertainties in the data (when converted into the same unit). By comparison with the previous Lagrangian assimilation, it appears that when the level of confidence in the background is high, the convergence is much slower than when the observations have granted a high confidence.

Figure 9.6 shows the evolution of the speed over time for the case A, presented in table 9.3. In this configuration, **R** is equivalent to about 10^{-4} in the speed space, so this corresponds to a case where the level of confidence in the background and in the observations is similar. The speed converges towards the true parameter within a reasonable amount of time (about 100s after the first assimilation) as expected.

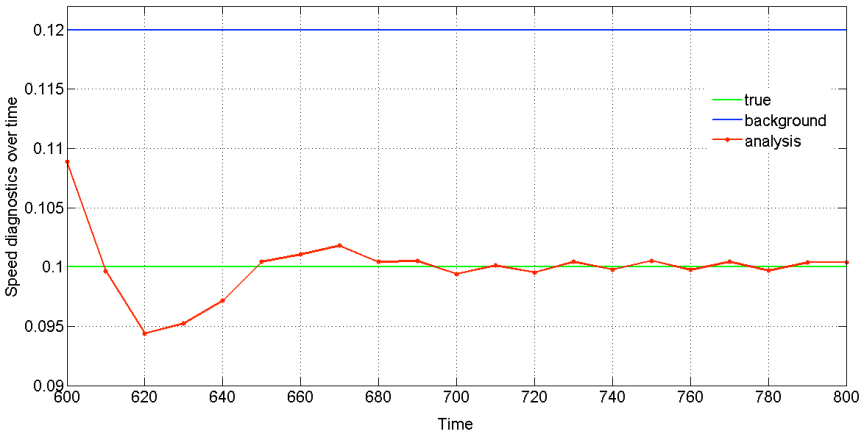

Figure 9.6: Evolution of the control parameter $s^a_{L,KPP}$ along the assimilation iterations, with an assimilation at each observation time step from $t_0 = 600$ to $t = 800$ (case A). The blue line represents the initial value of $s^b_{L,KPP} = 0.12$ at t_0, while the red line corresponds to the true parameter $s^t_{L,KPP} = 0.10$. This Lagrangian assimilation corresponds to the configuration where the speed depends linearly on the vegetation mass fraction Y.

This example highlights the potential of the Lagrangian assimilation for forest fires. Indeed, it is possible with a limited computational cost to calibrate the speed parameter using observations of the fire front positions over time. However, the robustness of the method has to be further investigated so as to know in which cases it gives more valuable results than the Eulerian approach.

Conclusion

This study proves that the Lagrangian technique could be suitable to assimilate the speed of the fire front within a reasonable amount of time, as it reduces considerably the number of integrations of the Eulerian model (only one integration for the production of observations). However, this has been performed in 1D only.

The generalization of this technique to a two-dimensional configuration is naturally the next stage of this investigation so as to be able to compare both Eulerian and Lagrangian techniques in a more realistic context. This generalization may encounter some difficulties. There would be indeed a complete set of particles along the fire front, so a technique would have to be implemented to associate the particles of the background front with the observed positions of the front over time. Furthermore, as the front grows over time and as its shape could change drastically, the Lagrangian technique shall be able to change the number of particles over time so as to keep a constant resolution accuracy.

Image assimilation could be a solution to investigate as it is currently performed in meteorology for the study of structures like clouds. This technique is aimed at assimilating information provided by satellite data, and thus at connecting model variables with image-type data. The idea is to add an extra term in the optimization problem so as to assimilate the transport of the image pixels, which are considered as pseudo-observations of velocity. This implies the determination of a mean distance between two clouds of points, one representing the observations, the other one the background position of the particles, and thus image assimilation is associated with a global assimilation correction.

In any case, the development of a Lagrangian technique may appear as a powerful tool to identify and track the dynamical evolution of the fire front even though the vegetation distribution is scattered. It would also make possible the assimilation of the initial position of the fire, which is known to be subject to significant uncertainties in reality.

Conclusion

Data assimilation is an established mature approach that appears in a wide range of applications, but there are specific challenges in fire and more generally combustion applications. Indeed, the critical information in the system is confined within a very thin region in the vicinity of the fire front. This reaction zone moves over time in different directions depending on the local conditions (e.g., vegetal fuel distribution), which makes it difficult to track over time. However, the present investigation shows that data assimilation is able to capture this information in space and time, and to lead to a more accurate prediction of the position of the flame front.

This feasibility study is organized in two steps. The first step consisted in ensuring that classical data assimilation algorithms (such as the BLUE) can be applied to wildfire applications. The measure of the DFS have highlighted the front-like topology of fires, while the a posteriori diagnostics have validated the implementation of the error statistics. The second step was aimed at defining a more physical configuration by developing a new fire propagation model and by introducing a speed control parameter for data assimilation. This led to the exploration of the potential of Eulerian and Lagrangian techniques.

Certainly, this investigation was limited to a stand-alone numerical feasibility study and does not represent a realistic fire configuration. Ongoing research is aimed at assimilating time-evolving locations of the flame front in 2D. It is also aimed at building a more physical flame spread model taking into account the vegetation, the wind and the topography characteristics. Finally, it is aimed at better accounting for uncertainties; for instance, while the present study considers the uncertainties associated with the flame spread model, it does not consider the uncertainties associated with the input data to the model, such as the vegetation distribution. The future prototype of data assimilation will take into account uncertainties in the vegetation, wind and topography data. This means that more parameters will be controlled; the size of the assimilation problem will therefore increase, implying an extra computational cost. Attention will have to be paid to the modeling of the covariance matrix for background errors (notably, the error correlations between the control parameters), and the validity of the linear tangent operator will have to be studied carefully so as to determine a valid range of values for each control parameter.

While much remains to be done, data assimilation has already shown potential in overcoming some of the limitations of wildfire modeling, and may appear as a new paradigm for fire and combustion problems.

Perspectives

"Mystery creates wonder, and wonder is the basis of man's desire to understand."
Neil Armstrong.

This internship was the starting point of a projet of widener perspectives, whose objective is to use data assimilation as a tool to improve the modeling of a fire propagation. Observations are an additional source of information from which knowledge on the dynamics of the system can be extracted and used to balance some of the fire model approximations. This data-driven simulation could lead on the long-range to a better understanding of the multi-physics interaction in a wildfire process.

To match these perspectives, I will start from October 2010 a PhD dissertation within the framework of the project ANR-COSINUS-IDEA, entitled *Fire propagation and Data assimilation*, under the supervision of the EM2C department of Ecole Centrale Paris, CERFACS and the Dept. of Fire Protection Engineering of UMD. While this master thesis was a necessary step to ensure the feasibility of data assimilation for wildfire applications, the PhD dissertation is aimed at developing a more realistic model for wildfire propagation using data assimilation as a tool. An extensive study of the fire dynamics will be carried out at the flame scale so as to understand which processes are predominant, which factors enhance or reduce the fire spread, or which gas components are producted by the reaction using a tabulation method. This focus on the physics of a wildfire and its modeling with the LES technique will be helpful to introduce data assimilation and to improve the forecast of fire propagation at a macroscopic scale.

This master thesis carried out in collaboration between CERFACS and UMD has proved to myself that it could encompass most of my research interests and fulfill my personal ambitions for my future professional career. It will indeed be captivating to work on a multidisciplinary project, at the interface between different research teams, in which I will be able to acquire a stronger knowledge on the physics of wildland fires, on the turbulence modeling and on the methodologies of data assimilation. As a future engineer in applied mathematics, it will be very interesting to combine numerical and statistical tools, so as to broaden my skills and to strengthen my knowledge in advanced modeling. Furthermore, the international collaboration with the University of Maryland will extend the scope of this project and the potential of further collaborations. While Dr. Arnaud Trouvé could provide his experience in fire modeling, Dr. Kayo Ide from the Department of Atmospheric and Oceanic Science could help in the development of the Lagrangian assimilation, while the PhD student Tatiana Sofronova from the Department of Geography could be a useful partner to investigate the vegetation influence on the fire propagation. With such an international framework and this *triangular collaboration* between EM2C, CERFACS and UMD, communication will be a key to complete this project successfully and to introduce this new paradigm in fire modeling.

Bibliography

[1] R. Rothermel. A mathematical model for predicting fire spread in wildland fires. *USDA Forest Service*, 1972.

[2] F.A. Albini. A model for fire spread in wildland fuels by radiation - a model including fuel cooling by convection. *Combustion Science and Technology*, 45:101–113, 1985.

[3] D.X. Viegas. Forest fire propagation. *Philosophical transactions of the Royal Society*, pages 2907–2928, 1998.

[4] Albert Tarantola. *Inverse Problem: Theory Methods for Data Fitting and Parameter Estimation*. Elsevier, 1987.

[5] Kayo Ide, Philippe Courtier, Michael Ghil, and Andrew C. Lorenc. Unified notation for data assimilation: operational, sequential and variational. *Journal of the Meteorological Society of Japan*, 75(1B):181–189, 1997.

[6] François Bouttier and Philippe Courtier. Data assimilation concepts and methods. Meteorological training course lecture series, ECMWF, March 1999.

[7] Eugenia Kalnay. *Atmospheric Modeling, Data Assimilation and Predictability*. 2003.

[8] David F. Parrish and John C. Derber. The national meteorological center's spectral statistical interpolation analysis system. *Monthly Weather Review*, 120:1747–1763, 1992.

[9] F. Rabier, H. Jarvinen, E. Kilnder, J-F. Mahfouf, and A. Simmons. The ecmwf operational implementation of four-dimensional variational assimilation. part i: Experimental results with simplified physics. *Quarterly Journal of the Royal Meteorological Society*, 126:1143–1170, 2000.

[10] P. Brasseur and J. Verron. *The SEEK filter method for data assimilation in oceanography: a synthesis*. 2006.

[11] A. Cowlard, W. Jahn, C. Abecassis-Empis, G. Rein, and J.L. Torero. Sensor assisted fire fighting. *Fire Technology*, 46:719–741, 2010.

[12] W. Jahn, G. Rein, and J.L. Torero. Forecasting fire growth using an inverse zone modeling approach. *Fire Safety Journal*, submitted for publication.

[13] J.Mandel, L.S.Bennethum, J.D.Beezley, J.L.Coen, C.D.Douglas, M.Kim, and A.Vodacek. A wildland fire model with data assimilation. *Mathematics and Computers in Simulation*, pages 584–606, 2008.

[14] A. Gelb. *Applied optimal estimation*. 1974.

[15] Olivier Talagrand. Assimilation of observations, an introduction. *Journal of the Meteorological Society of Japan*, 75(1B):191–209, 1997.

[16] Alexander Aitken. On least squares and linear combinations of observations. *Proceedings of the Royal Society of Edinburgh*, 55:42–48, 1935.

[17] Robin Plackett. Some theorems in least squares. *Biometrika*, 37(1/2):149–157, 1950.

[18] Sophie Ricci. Assimilation variationnelle ocÃ©anique: modÃ©lisation multivariÃ©e de la matrice de covariance d'erreur d'Ã©bauche. ThÃ¨se de doctorat, UniversitÃ© Paul Sabatier - Toulouse III - OcÃ©anographie Physique, 2004.

[19] A.L. Sullivanl. A review of wildland fire spread modelling, 1990-present 1: physical and quasi-physical models. *International Journal of Wildland Fire*, 18, 2009.

[20] A.L. Sullivanl. A review of wildland fire spread modelling, 1990-present 2: empirical and quasi-empirical models. *International Journal of Wildland Fire*, 18, 2009.

[21] A.L. Sullivanl. A review of wildland fire spread modelling, 1990-present 3: mathematical analogues and simulation models. *International Journal of Wildland Fire*, 18, 2009.

[22] J.H. Balbi, F. Morandini, X. Silvani, J.B. Filippi, and F. Rinieri. A physical model for wildland fires. *Combustion and Flame*, pages 2217–2230, 2009.

[23] Geir Evensen. Sequential data assimilation with a nonlinear quasi-geostrophic model using monte carlo methods to forecast error statistics. *Journal of Geophysical Research*, 99:10,143–10,162, 1994.

[24] T. Poinsot and D. Veynante. *Theoretical and Numerical Combustion, 2nd edition*. R. T. Edwards, 2005.

[25] J. M. Duclos, D. Veynante, and T. Poinsot. A comparison of flamelet models for premixed turbulent combustion. *Combustion and Flame 95*, pages 101–117, 1993.

[26] S.K. Lele. Compact finite difference schemes with spectral-like resolution. *Journal of Computational Physics*, 103:16–42, 1992.

[27] Olivier Talagrand. Objective validation and evaluation of data assimilation. In *Proceedings of Workshop on Diagnosis of Data Assimilation Systems*, pages 287–299. ECMWF, Shinfield Park, Reading, 2004.

[28] Gérald Desroziers, Loic Berre, Bernard Chapnik, and Paul Poli. Diagnosis of observation, background and analysis-error statistics in observation space. *Quarterly Journal of the Royal Meteorological Society*, 131(613):3385–3396, 2005.

[29] L. Kuznetsov, K. Ide, and C.K.R.T. Jones. A method for assimilation of lagrangian data. *Monthly Weather Review*, 131:2247–2260, October 2003.

[30] L.F. Meunier. Lagrangian assimilation of vorcore antarctic balloons in the geos-5 4dvar assimilation system. Final study report, ENM-NASA-University of Maryland, 2009.

[31] F. Rabier. Overview of global data assimilation developments in numerical weather-prediction centres. *Quarterly Journal of the Royal Meteorological Society*, 131:3215–3233, 2005.

[32] C.D. Rodgers. Information content and optimization of high spectral resolution measurements. (2830):136–147, 1996.

[33] Mike Fisher. Background error covariance modelling. In *Seminar Series on Recent developments in atmospheric and ocean data assimilation, 8-12 September 2003*, pages 45–63. ECMWF, Shinfield Park, Reading, 2003.

[34] Gérald Desroziers, Pierre Brousseau, and Bernard Chapnik. Use of randomization to diagnose the impact of observations on analyses and forecasts. *Quarterly Journal of the Royal Meteorological Society*, 131(611):2831–2837, 2005.

[35] Bernard Chapnik, Gérald Desroziers, Florence Rabier, and Olivier Talagrand. Properties and first application of an error-statistics tuning method in variational assimilation. *Quarterly Journal of the Royal Meteorological Society*, 130(601):2253–2275, 2004.

[36] Bernard Chapnik, Gérald Desroziers, Florence Rabier, and Olivier Talagrand. Diagnosis and tuning of observational error in quasi-operational data assimilation setting. *Quarterly Journal of the Royal Meteorological Society*, 132(615):543–565, 2006.

[37] Gérald Desroziers and Serguei Ivanov. Diagnosis and adaptative tuning of information error parameters in variational assimilation. *Quarterly Journal of the Royal Meteorological Society*, 127(574):1433–1452, 2001.

[38] Olivier Talagrand. A posteriori verification for analysis and assimilation algorithms. In *Proceedings of Workshop on Diagnosis of Data Assimilation Systems*, pages 17–28. ECMWF, Shinfield Park, Reading, 1998.

Appendix

A. KPP Analytical Solution

An equation of the form (A.1) can be solved analytically. The flame speed s_L can be extracted from the solution using a KPP analysis [24]: the idea is that the flame speed is controlled by the cold side of the flame (i.e. the zone where θ is close to 0) under the assumption of *frozen turbulent*, meaning that the turbulent flow field is not affected by combustion.

$$\frac{\partial \theta}{\partial t} = D \frac{\partial^2 \theta}{\partial x^2} + a\,(1-\theta)\,\theta \tag{A.1}$$

In this cold side of the flame, an expansion in exponential form ($\theta = exp[\lambda(x + s_L\,t)]$) can be sought. This term comes from the fact that the solution is steady in a moving frame of reference at speed $-s_L$. This is equivalent to a change of frame of reference such that:

$$\frac{\partial \theta}{\partial t} = s_L \frac{\partial \theta}{\partial x}$$

Hence, equation (A.1) becomes:

$$s_L \frac{\partial \theta}{\partial x} = D \frac{\partial^2 \theta}{\partial x^2} + a\,(1-\theta)\,\theta \tag{A.2}$$

In this expansion, the reaction rate is assumed to be $a\,\theta$ since $(1-\theta)$ is of order unity. In this new frame of reference attached to the flow, substituting $\theta = exp[\lambda\,x]$ in equation (**??**) leads therefore to the following equation for λ ($\lambda > 0$):

$$\lambda^2 - \frac{s_L}{D}\,\lambda + \frac{a}{D} = 0 \tag{A.3}$$

whose discriminant is $\Delta = \left(\frac{s_L}{D}\right)^2 - 4\,\frac{a}{D}$:

- if $\Delta < 0$, there is no solution,
- if $\Delta > 0$, this gives two positive roots $P = a/D$ and $S = s_L/D$, which is not acceptable in the KPP analysis,
- if $\Delta = 0$, there exists one single solution $s_L = 2\,\sqrt{aD}$.

The equation (A.1) has no solution for λ if the flame speed s_L is less than $2\sqrt{aD}$. However, the KPP analysis proves that this minimum speed is the actual speed of the flame, consequently $s_{KPP} = 2\sqrt{aD}$. It also provides the value of the parameter λ as a function of the flame speed s_L such that:

$$\lambda = \frac{s_L}{D} \tag{A.4}$$

Since λ is the inverse of a flame thickness δ_L, the flame thickness is given by:

$$\delta_L = \frac{D}{s_L} = \frac{1}{2}\sqrt{\frac{D}{a}} \tag{A.5}$$

So as to conclude, the KPP analysis provides a characterization of the flame, in terms of speed s_L and thickness δ_L, which depend on the two model parameters D and a of the reaction-diffusion equation.

B. DFS, or Degree of Freedom for Signals

Each observation, and at a larger scale each set of observations, contributes to the assimilation at a different level, depending on its position with respect to the wildfire propagation. The DFS, which stands for "Degree of Freedom for Signals", is then a useful tool to quantify the impact of the observations in the optimization problem. [31] introduces it so as to evaluate properly the impact of the data on the assimilation and to optimize the quantity and the location of data to be assimilated.

B.1 Notations

$\mathbf{y}^o = (\mathbf{y}_1^{oT}, ..., \mathbf{y}_q^{oT})^T$ represents the complete observation vector of the system by including the q set of observations available. Each set of observations $\mathbf{y}_k^{oT}$ $(k = 1, .., q)$ is defined as a vector of length p_k.

All the available information for data assimilation are supposed to form a vector $\mathbf{z}$, including both observations and background , so that $\mathbf{z} = (\mathbf{x}^b, \mathbf{y}^o)^T$. $\mathbf{z}$ is called the *generalized observation vector*. It is linked to the true state $\mathbf{x}^t$ by the relation $\mathbf{z} = \mathbf{\Gamma}\mathbf{x}^t + \epsilon$, with:

- $\mathbf{\Gamma} = (\mathbf{I}_n, \mathbf{H})^T$
  n represents the size of the state vector $\mathbf{x}$, while p gives the total number of observations. $\mathbf{H}$ is the observation operator of dimension $p \times n$, so $\mathbf{\Gamma}$ is a known matrix of dimension $(n + p) \times n$, whose rank is equal to n as data contain information on any component of the state $\mathbf{x}$. Note that this expression of $\mathbf{\Gamma}$ is valid as the *determinacy condition* is satisfied (independently of any gaussian hypothesis on the errors).

- $\epsilon = (\epsilon^{bT}, \epsilon^{oT})^T$
  ϵ is the vector representing the uncertainty in the data. $\epsilon^o = (\epsilon_1^{oT}, ..., \epsilon_q^{oT})^T$ is associated with the observations, with ϵ_k^o the error associated to the observation set k.

- $\mathbf{S} = \mathbb{E}[\epsilon \cdot \epsilon^T]$
  $\mathbf{S}$ is the covariance matrix of the error vector ϵ such that:

$$\mathbf{S} = \begin{pmatrix} \mathbf{B} & 0 \\ 0 & \mathbf{R} \end{pmatrix} \tag{B.1}$$

In the following, the subset of information i is obtained such that $\mathbf{z}_i = \mathbf{\Pi_i}\mathbf{z}$, with i the index of the set extracted from $\mathbf{z}$ by the selection operator $\mathbf{\Pi_i}$. Formally,

- $\mathbf{\Gamma}_i = \mathbf{\Pi_i}\mathbf{\Gamma}$,

- $\mathbf{S}_i = \mathbf{\Pi_i}\mathbf{S}{\mathbf{\Pi_i}}^T$

B.2 Contribution of a set of observations to the analysis

B.2.1 General context

In the context of a minimization problem, the cost function is expressed as a sum of N cost functions corresponding to each source of information assimilated (each source containing p_i observations). Hence,

$$J(\mathbf{x}) = \sum_{i=1,N} J_i(\mathbf{x}) = \frac{1}{2}\,(\mathbf{z}-\mathbf{\Gamma x})^T \mathbf{S}^{-1}(\mathbf{z}-\mathbf{\Gamma x}) \tag{B.2}$$

with i the index of a subset of information and J_i the cost function defined as:

$$J_i = \frac{1}{2}\,(\mathbf{z}_i-\mathbf{\Gamma}_i\mathbf{x})^T {\mathbf{S}_i}^{-1}(\mathbf{z}_i-\mathbf{\Gamma}_i\mathbf{x}) \tag{B.3}$$

It is known that the analysis error covariance matrix $\mathbf{A}$ is equal to the inverse of the Hessian matrix associated with the cost function J, consequently:

$$\mathbf{A}^{-1} = \sum_{i=1,N} \mathbf{\Gamma}_i^T \mathbf{S}_i^{-1} \mathbf{\Gamma}_i \tag{B.4}$$

Hence,

$$\mathbb{E}[J_i(\mathbf{x}^a)] = \frac{1}{2}\left(p_i - Tr(\mathbf{\Gamma}_i\,\mathbf{A}\mathbf{\Gamma}_i^T\,\mathbf{S}_i^{-1})\right) \tag{B.5}$$

supposing $\mathbf{S}$ optimal.

According to reference [27], the contribution c_i of a data subset i to the analysis is defined as:

$$c_i = Tr(\mathbf{S}_i^{-1/2}\,\mathbf{\Gamma}_i \mathbf{A} \mathbf{\Gamma}_i^T\,\mathbf{S}_i^{-1/2}) \tag{B.6}$$

and satisfies $\sum_{i=1}^{N} c_i = n$, n representing the size of the control vector $\mathbf{x}$.

B.2.2 Focus on the observations

So far in the analysis, no distinction has been made between the background and the temperature measurements, each quantity has been considered as a source of information. At this point, the objective is to study the contribution of the temperature measurements to the analysis so as to analyze the impact of their positions and of their number on the correction.

Considering a set of observations $\mathbf{y}_k^o$ extracted from $\mathbf{y}^o$ by $\mathbf{\Pi_k}$, its associated error covariance matrix and observation operator are respectively denoted $\mathbf{R}_k$ and $\mathbf{H}_k$. The contribution of this subset k is therefore given by:

$$\begin{aligned} c_k &= Tr(\mathbf{R}_k^{-1/2}\mathbf{H}_k\mathbf{A}\mathbf{H}_k^T\mathbf{R}_k^{-1/2}) \\ \Rightarrow c_k &= Tr(\mathbf{A}\mathbf{H}_k^T\mathbf{R}_k^{-1}\mathbf{H}_k) \end{aligned} \tag{B.7}$$

If p_k is the size of the vector $\mathbf{y}_k^o$, this contribution is equivalently defined as:

$$c_k = p_k - 2\mathbb{E}[J_k^o(\mathbf{x}^a)] \tag{B.8}$$

with:

$$\mathbb{E}[J_k^o(\mathbf{x}^a)] = \frac{1}{2}\,Tr(\mathbf{I}_k - \mathbf{A}\mathbf{H}_k^T\,\mathbf{R}_k^{-1}\mathbf{H}_k) \tag{B.9}$$

Recall that $J_k^o(x^a)$ is the part of the observation cost function associated with the set k of observations, and evaluated at the optimum $\mathbf{x}^a$.

B.3 Link with the number of Degrees of Freedom for Signal

The weight of the subset of information $\mathbf{y}_k^o$ in the assimilation system can be evaluated by measuring the trace of the analysis Jacobian with respect to this set of information. This weight is called DFS. Hence,

$$\mathrm{DFS} = Tr\Big(\frac{\partial(\mathbf{H}\mathbf{x}^a)}{\partial \mathbf{y}_k^o}\Big) = \sum_k Tr\Big(\frac{\partial(\mathbf{H}_k\mathbf{x}^a)}{\partial \mathbf{y}_k^o}\Big) \tag{B.10}$$

In the case of a linear problem, (B.10) is equivalent to:

$$\begin{aligned} \mathrm{DFS} &= Tr(\mathbf{HK}) \\ \Rightarrow \mathrm{DFS}_k &= Tr(\mathbf{\Pi}_k\mathbf{HK}{\mathbf{\Pi}_k}^T) \end{aligned} \tag{B.11}$$

with DFS_k the DFS associated to the subset k. This represents a special case of the contribution c_k defined in (B.7), when the errors of the observations k are not correlated with the errors of the other subsets of observations.

More information about DFS and their implication in data assimilation are available in [32] and [33].

B.4 Reduction of the uncertainty linked to the set of observations

As $\mathbf{A} = \mathbf{B}\left(\mathbf{I} - \mathbf{KH}\right) = \mathbf{B} - \mathbf{A}\mathbf{H}^T\,\mathbf{R}^{-1}\,\mathbf{HB}$, the total variance reduction r_v of $\mathbf{z}^o$ due to the assimilation algorithm is defined by [34] as:

$$\begin{aligned} r_v &= Tr(\mathbf{B}) - Tr(\mathbf{A}) \\ \Rightarrow r_v &= Tr(\mathbf{A}\mathbf{H}^T\mathbf{R}^{-1}\mathbf{HB}) \end{aligned} \tag{B.12}$$

If the observation errors are independent, the variance reduction r_v can be computed for any subset of observations k. The associated variance reduction, denoted $r_{v,k}$, is then defined as:

$$r_{v,k} = Tr(\mathbf{A}{\mathbf{H_k}}^T{\mathbf{R_k}}^{-1}\mathbf{H_k}\mathbf{B}) \tag{B.13}$$

implying:

$$\mathbf{A} = \mathbf{B} - \sum_k \mathbf{A}\mathbf{H}_k^T\,\mathbf{R}_k^{-1}\,oH_k\mathbf{B} \tag{B.14}$$

with $(\mathbf{R}_k, \mathbf{H}_k)$ the operators associated with the subset k.

This quantity $r_{v,k}$ is compared to the total variance reduction r_v, so as to measure the specific contribution of the subset k in the assimilation. Equivalently,

$$\mathbf{A}\mathbf{H}_k^T\mathbf{R}_k^{-1}\mathbf{H}_k\mathbf{B} = \mathbf{A}\mathbf{H}^T\mathbf{R}^{-1}\mathbf{S}_k\mathbf{S}_k\mathbf{HB} = \mathbf{A}\mathbf{H}^T\mathbf{R}^{-1}\mathbf{S}_k\mathbf{HB} = \mathbf{K}\mathbf{S}_k\mathbf{HB}$$

where $\mathbf{S_k}$ is an operator which sets to 0 all components which do not correspond to subset k and keeps all the others the same. What is more, it satisfies $\mathbf{S}_k\mathbf{S}_k = \mathbf{S}_k$ and since observation errors are independent, $\mathbf{S}_k$ commutes with $\mathbf{R}^{-1}$.
Hence,

$$r_{v,k} = Tr(\mathbf{K}\mathbf{S}_k\mathbf{HB}) \tag{B.15}$$

meaning that $\mathbf{S}_k$ is applied to $\mathbf{HB}$ in order to select the observations associated with subset k.

Equation (B.13) can be projected onto another space by applying the transformation $\mathbf{B}^{-1/2}$. Then the variance reduction $\tilde{r}_{v,k}$ associated with subset k is equal to DFS_k, defined in (B.11), such that:

$$\tilde{r}_{v,k} = Tr(\mathbf{A}\mathbf{H}_k^T\mathbf{R}_k^{-1}\mathbf{H}_k) = Tr(\mathbf{\Pi}_k\mathbf{HK}{\mathbf{\Pi}_k}^T) \tag{B.16}$$

This result is generalized to the whole information system as $\tilde{r}_v = Tr(\mathbf{HK})$. This means that the DFS can be assimilated as

- the total error variance reduction due to the assimilation algorithm,
- the expectation value of the cost function evaluated at the analysis (if prior matrices $\mathbf{B}$ and $\mathbf{R}$ are correctly specified).

Hence,

$$\tilde{r}_{v,k} = Tr(\mathbf{K}\mathbf{S}_k\mathbf{H}) = \mathbb{E}[J_k^o(\mathbf{x}^a)] \tag{B.17}$$

C. Data Assimilation Diagnostics

In [28], Desroziers develops consistency diagnostics that should be fulfilled to guarantee an optimal analysis and that may potentially give information on imperfectly prescribed observation and background error statistics. These consistency diagnostics are almost cost-free since they result from the combination of quantities that are already required during the assimilation algorithm. More details are given in references [35][36][37][34] and [27].

C.1 A general assimilation diagnosis

According to reference [38], the cost function J evaluated at the control variable $\mathbf{x}$ consists in a background and an observation contributions such that $J(\mathbf{x}) = J^b(\mathbf{x}) + J^o(\mathbf{x})$. Consequently, *a posteriori* validation of the assimilation system can be derived from equation (B.5). Hence,

$$\begin{aligned}
\mathbb{E}[J^o(\mathbf{x}^a)] &= \frac{1}{2}\Big(p - Tr(\mathbf{H}^T\mathbf{R}^{-1}\mathbf{HA}\Big) \\
&= \frac{1}{2}\Big(p - Tr(\mathbf{H}^T\mathbf{K}^T\Big) \\
\Rightarrow \mathbb{E}[J^o(\mathbf{x}^a)] &= \frac{1}{2}Tr(\mathbf{I}_p - \mathbf{HK}) \qquad \text{(C.1)} \\
\mathbb{E}[J^b(\mathbf{x}^a)] &= \frac{1}{2}\Big(n - Tr(\mathbf{B}^{-1}(\mathbf{B} - \mathbf{KHB}))\Big) \\
&= \frac{1}{2}\Big(n - Tr(\mathbf{I}_n - \mathbf{B}^{-1}\mathbf{KHB}\Big) \\
\Rightarrow \mathbb{E}[J^b(\mathbf{x}^a)] &= \frac{1}{2}Tr(\mathbf{HK}) \qquad \text{(C.2)} \\
& \qquad \text{(C.3)}
\end{aligned}$$

using $\mathbf{K} = \mathbf{AH}^T\mathbf{R}^{-1}$ in (C.1) and $\mathbf{A} = \mathbf{B} - \mathbf{KHB}$ in (C.2).

Since $Tr(\mathbf{KH}) = Tr(\mathbf{HK})$, the diagnosis is given by:

$$\mathbb{E}[J(\mathbf{x}^a)] = \mathbb{E}[J^o(\mathbf{x}^a)] + \mathbb{E}[J^b(\mathbf{x}^a)] = \frac{1}{2}Tr(\mathbf{I}_p) = \frac{p}{2} \qquad \text{(C.4)}$$

So if the observation error covariances are properly specified, then the expectation value of the cost function estimated at the analysis is simply proportional to the number of observations assimilated p, which also corresponds to the number of degrees of freedom in the analysis problem.

If this simple *a posteriori* diagnosis is not satisfied by the analysis $\mathbf{x}^a$, it could indicate a misspecification of the statistics on the observation errors. Note that some hypothesis are commonly assumed in practice so as to avoid extra complications: firstly, the expectation operator is approximated by one realization and secondly, actual observations may have spatially correlated errors but they are commonly analyzed with a diagonal $\mathbf{R}$-matrix. These assumptions may lead to an expectation value of J slightly different from $p/2$. In any case, Desrozier's diagnostics will give a more precise insight on the source of the misspecification in the assimilation.

C.2 Innovation

From the definition of the innovation vector $\mathbf{d}^{ob}$, the following sequence of relations may be derived:

$$\begin{aligned} \mathbf{d}^{ob} &= \mathbf{Y}^o - H(\mathbf{X}^b) \\ &= \mathbf{Y}^o - H(\mathbf{x}^t) + H(\mathbf{x}^t) - H(\mathbf{X}^b) \\ &\approx \epsilon^o - \mathbf{H}\,\epsilon^b \end{aligned}$$

with $H(\mathbf{x}^t) - H(\mathbf{X}^b) \approx \mathbf{H}\,(\mathbf{x}^t - \mathbf{X}^b) = \mathbf{H}\,\epsilon^b$.
If error covariance matrices $\mathbf{B}$ and $\mathbf{R}$ are correctly specified in the assimilation problem, then a consistency diagnostics on the innovation vector $\mathbf{Y}^o$ is given by:

$$\mathbb{E}[\mathbf{d}^{ob} \cdot \mathbf{d}^{obT}] = \mathbb{E}[\epsilon^o \cdot \epsilon^{oT}] + \mathbf{H}\,\mathbb{E}[\epsilon^b \cdot \epsilon^{bT}]\,\mathbf{H}^T \tag{C.5}$$

using the linearity of the statistical expectation operator $\mathbb{E}$ and assuming that observation errors ϵ^o and background errors ϵ^b are uncorrelated. Consequently,

$$\mathbb{E}[\mathbf{d}^{ob} \cdot \mathbf{d}^{obT}] = \mathbf{R} + \mathbf{H}\,\mathbf{B}\,\mathbf{H}^T \tag{C.6}$$

C.3 Background and observation covariances

The Kalman gain $\mathbf{K}$ is defined as $\mathbf{K} = \mathbf{B}\,\mathbf{H}^T\,(\mathbf{H}\,\mathbf{B}\,\mathbf{H}^T + \mathbf{R})^{-1}$ if the covariances for background and observation errors are consistent with the assimilation algorithm. Furthermore,

$$\mathbf{d}^{ab} = H(\mathbf{X}^a) - H(\mathbf{X}^b) \approx \mathbf{H}\,\delta\mathbf{X}^a = \mathbf{H}\,\mathbf{K}\,\mathbf{d}^{ob} \tag{C.7}$$

In practice, $\mathbf{d}^{ab}$ shall be computed such that $\mathbf{d}^{ab} = \mathbf{H}\,\delta\mathbf{X}^a$, so $\delta Xa = \mathbf{X}^a - \mathbf{X}^b$ shall be projected onto the observation space using the tangent linear of H. In others words,$\mathbf{d}^{ab}$ is defined in the assimilation diagnostics as:

$$\mathbf{d}^{ab} = \mathbf{H}\,(\mathbf{X}^a - \mathbf{X}^b) \tag{C.8}$$

This leads to:

$$\mathbf{d}^{ab} \cdot \mathbf{d}^{obT} = \mathbf{H}\,\mathbf{K}\,\mathbf{d}^{ob} \cdot \mathbf{d}^{obT} \tag{C.9}$$

Applying the expectation operator $\mathbb{E}$ leads to:

$$\mathbb{E}[\mathbf{d}^{ab} \cdot \mathbf{d}^{obT}] = \mathbf{H}\,\mathbf{K}\,\mathbb{E}[\mathbf{d}^{ob} \cdot \mathbf{d}^{obT}] \tag{C.10}$$

Using (C.6), this expression becomes:

$$\mathbb{E}[\mathbf{d}^{ab} \cdot \mathbf{d}^{obT}] = \mathbf{H}\,\mathbf{K}\,(\mathbf{R} + \mathbf{H}\,\mathbf{B}\,\mathbf{H}^T) = \mathbf{H}\,\mathbf{B}\,\mathbf{H}^T \tag{C.11}$$

This additional diagnostic provides a separated consistency check on the background error covariances in the observation space.

As to the observation covariance, its diagnostic is linked to the distance between the observations and the analysis projected onto the observation space, denoted $\mathbf{d}^{oa}$. This is defined as follows:

$$\mathbf{d}^{oa} = \mathbf{Y}^o - H(\mathbf{X}^b + \delta\mathbf{X}^a) \approx \mathbf{Y}^o - H(\mathbf{X}^b) - \mathbf{H}\,\mathbf{K}\,\mathbf{d}^{ob} = (\mathbf{I} - \mathbf{H}\,\mathbf{K})\,\mathbf{d}^{ob} \tag{C.12}$$

Hence,

$$\begin{aligned} \mathbf{d}^{oa} &= \mathbf{R}\,(\mathbf{H}\,\mathbf{B}\,\mathbf{H}^T + \mathbf{R})^{-1}\,\mathbf{d}^{ob} \\ \mathbb{E}[\mathbf{d}^{oa} \cdot \mathbf{d}^{obT}] &= \mathbf{R}\,(\mathbf{H}\,\mathbf{B}\,\mathbf{H}^T + \mathbf{R})^{-1}\,\mathbb{E}[\mathbf{d}^{ob} \cdot \mathbf{d}^{obT}] = \mathbf{R} \end{aligned} \tag{C.13}$$

C.4 Analysis covariances

It can be deduced from the previous diagnostics that:

$$\begin{aligned} \mathbf{d}^{ab} \cdot \mathbf{d}^{oaT} &= \mathbf{H}\,\mathbf{K}\,\mathbf{d}^{ob}\,\mathbf{d}^{obT}\,(\mathbf{I}-\mathbf{K}\,\mathbf{H})^T \\ &= \mathbf{H}\,\mathbf{B}\,\mathbf{H}^T\,(\mathbf{H}\,\mathbf{B}\,\mathbf{H}^T+\mathbf{R})^{-1}\,\mathbf{d}^{ob}\mathbf{d}^{obT}\,(\mathbf{H}\,\mathbf{B}\,\mathbf{H}^T+\mathbf{R}^{-1}),\mathbf{R} \end{aligned} \tag{C.14}$$

Hence,

$$\mathbb{E}[\mathbf{d}^{ab} \cdot \mathbf{d}^{oaT}] = \mathbf{HBH}^T\,(\mathbf{HBH}^T+\mathbf{R}^{-1})\,\mathbf{R} = \mathbf{HAH}^T \tag{C.15}$$

So the diagnostic on analysis covariances is defined as $\mathbb{E}[\mathbf{d}^{ab} \cdot \mathbf{d}^{oaT}] = \mathbf{HAH}^T$ if the matrices $\mathbf{HBH}^T$ and $\mathbf{R}$ are correctly specified in the assimilation process.

Conclusion

As a conclusion, the relations (C.6), (C.11), (C.13) and (C.15) provide 4 consistency diagnostics on the assimilation process as well as an insight on the uprightness of the background and observation error covariances. In the context of an operational assimilation, these error covariances are only partially known and are therefore expected to be incorrectly specified. If so, Desroziers defines a method to tune them *a posteriori*.

Consider a subset i of p_i observations. This method consists in finding the background and observation variances, denoted respectively $(\sigma_b)_i$ and $(\sigma_o)_i$, associated with the subset i, satisfying (C.16) and (C.17):

$$\begin{aligned} (\sigma_b^i)^2 &= \frac{(\mathbf{d}^{abT})_i\,(\mathbf{d}^{ob})_i}{p_i} \\ &= \frac{1}{p_i}\sum_{j=1}^{p_i}(\mathbf{Y}_j^a-\mathbf{Y}_j^b)\,(\mathbf{Y}_j^o-\mathbf{Y}_j^b) \end{aligned} \tag{C.16}$$

where $\mathbf{Y}_j^a$ and $\mathbf{Y}_j^b$ represent respectively the component j of the equivalent analysis and background in the observation space, while $\mathbf{Y}_j^o$ corresponds to the component j of the observation vector $\mathbf{Y}^o$.
Similarly,

$$\begin{aligned} (\sigma_o^i)^2 &= \frac{(\mathbf{d}^{oaT})_i\,(\mathbf{d}^{ob})_i}{p_i} \\ &= \frac{1}{p_i}\sum_{j=1}^{p_i}(\mathbf{Y}_j^o-\mathbf{Y}_j^a)\,(\mathbf{Y}_j^o-\mathbf{Y}_j^b) \end{aligned} \tag{C.17}$$